Phase-separated disordered bulk-heterojunction nanostructures for photoelectrochemical hydrogen generation

by

Subash Rajasekar

M.S., Indian Institute of Technology Madras, 2015

B.E., College of Engineering Guindy, Anna University, 2011

Thesis Submitted in Partial Fulfillment of the

Requirements for the Degree of

Doctor of Philosophy

in the

Department of Chemistry

Faculty of Science

© Subash Rajasekar 2022

SIMON FRASER UNIVERSITY

Fall 2022

Copyright in this work rests with the author. Please ensure that any reproduction or re-use is done in accordance with the relevant national copyright legislation.

Declaration of Committee

Name:	**Subash Rajasekar**
Degree:	**Doctor of Philosophy (Chemistry)**
Title:	**Phase-separated disordered bulk-heterojunction nanostructures for photoelectrochemical hydrogen generation**
Committee:	**Chair:** **Robert Britton** Professor, Chemistry
	Steven Holdcroft Supervisor Professor, Chemistry
	Erik Kjeang Committee Member Professor, Mechatronic Systems Engineering
	Neil Branda Committee Member Professor, Chemistry
	Vinay Tiwari Committee Member Senior Research Manager Indian Oil Corporation
	Sami Khan Examiner Assistant Professor, Sustainable Energy Engineering
	Timothy L. Kelly External Examiner Professor, Chemistry University of Saskatchewan

Abstract

Donor:Acceptor bulk-heterojunction (BHJ) electrodes are expected to play significant roles in electrode design aimed to increase the efficiency of photoactive materials with low exciton lifetime and diffusion length. While planar BHJ electrodes are well-studied in literature, poor control over donor and acceptor domain sizes during electrode preparation renders it difficult to achieve consistent device performance. Herein, as an alternate to planar BHJ electrodes, nanoparticle BHJ is proposed where the domain size is externally controlled during the preparation of the nanoparticles, which are subsequently used to make the photoelectrode. This approach preserves the domain size and hence is expected to offer better control over planar BHJ electrode design.

Based on the donor and acceptor phase distribution, a nanoparticle-based electrode can be categorized as (i) core-shell, (ii) blended, (iii) randomly-distributed, and (iv) Janus-type structures. Owing to the lack of continuous charge transport pathways in other categories, both within and across the nanoparticle interface, it is hypothesized that randomly-distributed nanoparticle-based BHJ electrodes perform better than other configurations. Hence, to validate, photoelectrochemical behaviour of randomly-distributed BHJ nanoparticulate electrode is examined using organic semiconductors P3HT and PCBM serving as electron donor and acceptor, respectively for hydrogen generation applications.

Individual P3HT and PCBM nanoparticles were prepared by the miniemulsion technique, which are subsequently used to fabricate distinct donor-acceptor, phase-separated, core-shell structure free bulk-heterojunction photoelectrodes. The optoelectronic, morphological and photoelectrochemical H_2 generation examinations revealed that the prepared nanoparticulate electrode performs better than the other nanoparticle-based BHJ electrodes under similar conditions. Following this, BHJ electrodes comprising CuO and TiO_2 nanoparticles were fabricated to determine if similar results can be extrapolated to inorganic semiconductor photoelectrodes. However, on the contrary, the inorganic nanoparticle-based BHJ electrodes displayed poor photoelectrochemical characteristics. The decreased performance is determined to be due to: (i) high electron-hole recombination at the donor and acceptor interface, (ii) increased electrode resistance upon TiO_2 addition, and (iii) photocorrosion.

Keywords: Photoelectrochemistry; Organic semiconductor; Polymer nanoparticle; P3HT; PCBM; CuO; TiO_2; Bulk-heterojunction; Solar hydrogen generation; Miniemulsion; Photoelectrode; Photocathode; Water splitting

Dedication

To My Family

Acknowledgements

I express my sincere gratitude to Prof. Steven Holdcroft for his guidance and the opportunity to be part of his research group. It would not have been possible to complete this thesis without his continuous support.

I am thankful to the supervisory committee members Prof. Neil Branda, Prof. Erik Kjeang, and Dr. Vinay Tiwari for their insightful comments and suggestions throughout the project.

I am grateful to my external supervisor Dr. Vinay Tiwari for sharing his views on research directions, guidance, and administrative support during my time at Indian Oil Corporation.

I would like to thank all the present and past members of the Holdcroft group for their warm acceptance. I cannot be thankful enough to Dr. Patrick Fortin for sharing his knowledge and technical expertise in organic photoelectrochemical cells. I also thank present and past members of the Solar Hydrogen Laboratory of IOC, particularly Mr. Ziya-Ul-Haq.

Finally, I am grateful to SFU and IOC management team for offering the collaborative Ph.D. program and the opportunity to be a part thereof, particularly to Dr. Umish Srivastva and Mr. Alok Sharma.

Table of Contents

List of Tables

List of Figures

List of Symbols and Abbreviations

A	Area of an electrode
AC	Alternating current
BHJ	Bulk-heterojunction
c	Speed of light
CB	Conduction band
C_{dl}	Double-layer capacitance
CE	Counter electrode
C_H	Helmholtz capacitance
$CHCl_3$	Trichloromethane (chloroform)
CMC	Critical micelle concentration
CP	Conjugated polymers
C_{SC}	Space-charge capacitance
CTAB	Cetyltrimethyl ammonium bromide
Cu_2O	Copper(I) oxide
CuO	Copper(II) oxide
d	Diameter of particles
D	Diffusion coefficient
D-A	Donor-Acceptor
DC	Direct current
DET	Dexter energy transfer
DLS	Dynamic light scattering
e	Electronic charge
E_{bg} or E_g	Energy gap or bandgap
EDX	Energy-dispersive X-ray spectroscopy
E_F	Fermi level
E_{FB}	Flat band potential
EIS	Electrochemical impedance spectroscopy
E_{ph}	Photopotential
E_{redox}	Redox potential
ETL	Electron transport layer
F	Faraday constant
FRET	Förster resonance energy transfer

FTO	Florine-doped tin oxide
GC	Gas chromatography
h	Planck's constant
HER	Hydrogen evolution reaction
HOMO	Highest occupied molecular orbital
HTL	Hole transport layer
I	Intensity of light
i	Complex number
IHP	Inner Helmholtz plane
IPCE	Incident photon-to-current efficiency
ITO	Indium tin oxide
j	Current density
k_B	Boltzmann constant
L_D	Carrier diffusion length
LSV	Linear sweep voltammetry
LUMO	Lowest unoccupied molecular orbital
MoS_3	Molybdenum trisulfide
M-S	Mott-Schottky
N_A	Avogadro constant
N_a	Acceptor carrier density
N_d	Donor carrier density
NP	Nanoparticle
OCP	Open circuit potential
OER	Oxygen evolution reaction
OHP	Outer Helmholtz plane
OPEC	Organic photoelectrochemical cell
OPV	Organic photovoltaics
Ox	Oxidized species
P3HT	Poly(3-hexylthiophene)
PC	Photocatalysis
PCBM	[6,6] phenyl-C61-butyric acid methyl ester
PEC	Photoelectrochemical cell
PEDOT:PSS	Poly(3,4-ethylenedioxythiophene) polystyrene sulfonate
PEPS	Photoelectrochemical photocurrent switching

PV	Photovoltaic cell
R	Reflectance
RE	Reference electrode
Red	Reduced species
RHE	Reversible hydrogen electrode
s	Scattering factor
SCE	Saturated calomel electrode
SDS	Sodium dodecyl sulfate
SEM	Scanning electron microscopy
SHE	Standard hydrogen electrode
STH	Solar-to-hydrogen conversion efficiency
T	Temperature
TEM	Transmission electron spectroscopy
TiO_2	Titanium(IV) oxide
UV	Ultraviolet radiation
VB	Valence band
V_{max}	Maximum photovoltage
WE	Working electrode
XRD	X-ray diffraction
Z	Impedance
α	Absorption coefficient
ε_o	Permittivity of free space
ε	Dielectric constant
η	Viscosity
λ	Wavelength
μ	Chemical potential
ν	Frequency of the incident light
τ	Exciton recombination time

Chapter 1.

Introduction

A vision set in the Paris climate agreement (2015) and reaffirmed in the Glasgow climate pact (2021) is a gradual shift in energy dependence from carbon-based fuels toward alternative energy sources to limit the rising global temperature within 2 °C above pre-industrial levels.[1, 2] To achieve this, it is paramount to switch from using fossil-fuel-based resources such as coal, natural gas, and petroleum products for energy conversion/generation to safe, renewable, and earth-abundant resources. A wide array of alternatives, such as solar, wind, hydro, geothermal, and biomass, are available to replace carbon-based fuels to meet the energy requirements. Of these available resources, solar energy has received considerable attention owing to the copious amount of power (1.08×10^8 GW) that reaches the earth every day. If harvested efficiently, the incident insolation is sufficient to meet the current and projected global energy consumption requirements.[3] Significant progress has been achieved in terms of harnessing irradiant solar energy via photovoltaics in the past decade; the maximum energy conversion efficiency of photovoltaic panels has increased significantly from ~20% at the beginning of the century to more than 40%.[4] In addition to the increased efficiency, the cost of electricity produced from solar panels is continuously decreasing.[5] These factors make solar energy one of the prime candidates for an alternative energy source.

Despite this remarkable progress, intermittency of solar irradiation hinders its widespread adaptation.[6, 7] This necessitates the storage of solar energy when the source is not available to achieve seemingly continuous energy utilization. Though there are several technologies available to store solar energy, most can be classified under four broad categories: (i) electrochemical storage (e.g., batteries, supercapacitors), (ii) chemical storage (e.g., hydrogen, methane), (iii) mechanical storage (e.g., flywheel, pumped hydro), and (iv) thermal storage (e.g., molten salts, phase change materials).[8, 9] Different storage techniques offer unique advantages and disadvantages, and the choice of selection usually depends on the intended final application. For instance, batteries are best suited for electrical energy applications, while thermal storage systems are preferred for space heating and cooking applications.

This thesis focuses on the application of solar energy storage in hydrogen via water splitting.[10] The current chapter briefly introduces photoelectrochemical (PEC) hydrogen generation (which is also referred to as solar water splitting) and its working principle. Additionally, it discusses different tools to characterize and measure the performance of a semiconductor photoelectrode used in a PEC device.

1.1. Solar Hydrogen

Hydrogen is an energy carrier that releases water as a by-product upon reacting with oxygen; hence it is currently regarded as one of the major candidates for the low-carbon energy economy of the future. Hydrogen-based energy conversion devices are expected to play a significant role in the automotive, domestic heating, and solar energy storage industries. To be used as a clean energy carrier, it is essential to understand the carbon footprint of the hydrogen supply chain. Approximately, half of the global hydrogen is produced via *steam methane reforming,* a process that converts hydrocarbon feedstock to hydrogen and carbon monoxide/dioxide (Equations 1.1 and 1.2). About 30% is obtained from the *petroleum refining* process, and 18% is from *coal gasification,* in which coal is partially oxidized with steam and oxygen to produce hydrogen along with CO and CO_2. Together these three technologies contribute to 96% of global hydrogen production.[11-13] However, these processes are not 'clean' as CO or CO_2 is liberated during production. Though it is possible to capture and store the liberated gases via sequestration steps, it is not sustainable in the long term.[14]

$$CH_4 + H_2O \rightleftharpoons CO + 3H_2 \quad (1.1)$$

$$CO + H_2O \rightleftharpoons CO_2 + H_2 \quad (1.2)$$

Electrolysis occupies the fourth place, contributing less than 4% of the global hydrogen production, and is the only industry-level production technique that does not directly depend on carbon-based feedstock.[15] In an electrolyzer, water molecules are split into hydrogen and oxygen ($2H_2O \rightleftharpoons 2H_2+O_2$) by applying an electrical potential of more than 1.23 V (>1.6 V, if including various losses).[16] If the energy used to split water is produced from renewable sources such as solar, wind, or hydro and not from fossil-fuel-based power plants, electrolysis could be a potential source for 'clean' hydrogen. Though

electrolyzers powered by photovoltaic panels instead of grid electricity is one way to generate 'clean' hydrogen,[17] several technologies are under development to directly convert solar energy to hydrogen, such as photolysis, biolysis, and thermolysis:[12, 18, 19]

- Electrolysis - Electrical energy is used to split water molecules into H_2 and O_2
- Photoelectrolysis - Solar energy is directly used to split water, avoiding the intermediary electricity generation step
- Thermolysis - Energy to split water is provided via high temperature (500° - 2000°C), instead of electrical energy
- Biolysis - Microbiological organisms such as algae and bacteria are used to produce hydrogen from water in the presence of sunlight

Among these, photoelectrolysis-based systems are regarded as the most suitable for green hydrogen generation considering their low environmental impact, relative simplicity, low operating temperature, and ease of large-scale implementation.[20]

1.2. Hydrogen Generation via Photoelectrolysis

Photolytic H_2 generation is a non-polluting, renewable pathway to generate hydrogen. Photolysis, in general, defines a broad range of chemical or electrochemical reactions wherein the dissociation of molecules is achieved under the influence of photons.[21, 22] In the context of solar H_2, dissociation of water molecules to its components (H_2 and O_2) utilizing the energy of solar photons is known as photoelectrolysis.[23] At the heart of photoelectrolysis lies a 'semiconductor' that absorbs incident solar photons (detailed discussion is presented in section 1.2.1). When sufficiently energetic illumination strikes the semiconductor, the photonic energy is absorbed and converted to electrons (e^-) and holes (h^+) in a process known as '*excitation'.*

The excited semiconductor uses the absorbed energy to split *water* molecules. If the energy of excited electrons is higher than the potential necessary to dissociate H_2O, water splitting occurs; and H_2 and O_2 are produced. The electrons participate in the hydrogen evolution reaction and holes in the oxygen evolution reaction. Theoretically, a potential of ~1.23 V is required to split hydrogen from H_2O; however, due to the activation

and kinetic losses, ~1.7 V is typically needed to achieve practical water splitting.[24, 25] If a single semiconductor cannot generate enough potential to split water two or more semiconductors can be combined to reach the required potential (detailed discussion in section 2.3.1).

Photoelectrolysis is classified into two major categories: (i) photocatalytic and (ii) photoelectrochemical hydrogen generation based on the form the photoabsorber (semiconductor) is deployed.[26]

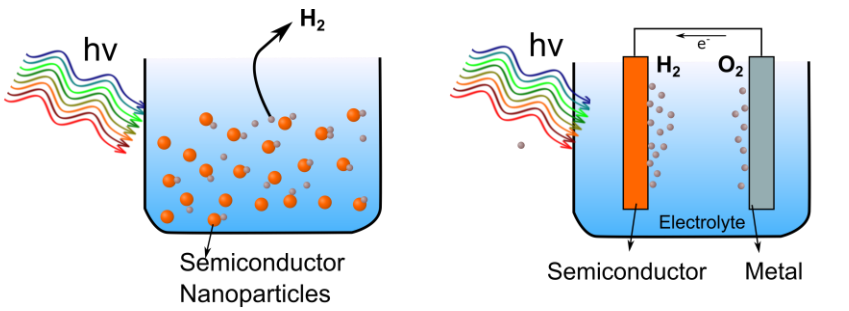

Figure 1.1 Schematics of (a) photocatalytic (suspended photoabsorber) and (b) photoelectrochemical (compact electrode absorber) device configuration for hydrogen generation.

a) Photocatalytic (PC) H_2 Generation

In photocatalytic systems anodic and cathodic reactions occur at the same photoabsorber; typically, the semiconductor photoabsorber in particulate form is dispersed in an aqueous solution (electrolyte), as depicted in Figure 1.1a. For an ideal semiconductor that is able to generate photovoltage of >1.23 V and catalytic towards hydrogen evolution, water splitting occurs at the surface of particles upon illumination, producing a mixture of H_2 and O_2.[27] To prevent the formation of explosive H_2 and O_2 mix, it is essential to suppress the O_2 evolution. Towards this end, sacrificial agents such as methanol, ethanol, sodium sulfite, sodium sulfide, and lactic acid are added to the electrolyte.[28, 29] Sacrificial agents preferentially react with holes thus reducing O_2 evolution. The choice of sacrificial agents depends on several parameters, such as the semiconducting nature of the photoabsorber, i.e., p-type or n-type semiconductivity, valence and conduction band energy levels, chemical stability, etc.[28, 30]

$$2H_2O \xrightarrow{hv} 2H_2 + O_2 \text{ (without sacrificial agent)} \quad (1.3)$$

$$CH_3OH + H_2O \xrightarrow{hv} 3H_2 + CO_2 \text{ (with } CH_3OH \text{ sacrificial agent)} \quad (1.4)$$

$$H_2O + SO_3^{2-} \xrightarrow{hv} H_2 + SO_4^{2-} \text{ (with } Na_2SO_3 \text{ sacrificial agent)} \quad (1.5)$$

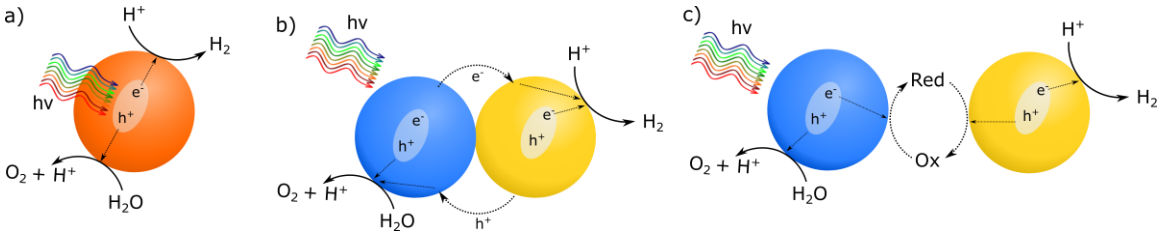

Figure 1.2 **Schematic working principle of (a) single absorber, (b) dual-absorber heterojunction, and (c) dual-absorber z-scheme with intermediary redox couple, depicting photocatalytic hydrogen generation. Arrows indicate charge transport pathways.**

For a non-ideal semiconductor that can only generate a potential less than the water splitting potential (i.e., 1.23 V), more than one semiconductor is used in tandem to achieve the necessary photovoltage. This type of catalysis is known as *heterojunction photocatalysis*.[31] As charge transfer between the semiconductors is essential to increase the photovoltage, it is required that the semiconductors be in direct ohmic contact (as depicted in Figure 1.2b).[32] In the case of not being able to achieve two semiconductors in tandem, an intermediary redox couple is used to assist the charge transfer function between the semiconductors; this is known as *Z-scheme photocatalysis* and offers an efficient way to separate H_2, as water redox reactions occur at spatially different locations.[33] Some of the redox mediators used for this purpose are VO_2^+/VO^{2+}, IO_3^-/I^-, $[Fe(CN)_6]^{3-}/[Fe(CN)_6]^{4-}$ etc.[34, 35]

Although hydrogen generation via the photocatalytic route is appealing, the reported solar-to-hydrogen conversion efficiency of most of the photocatalytic semiconductors is <1%, with very few outliers reporting >5% efficiency.[35, 36] The low efficiency combined with additional costs associated with keeping the photocatalysts in suspension, sacrificial agents, H_2 separation, and intermediary redox couples increase the cost of hydrogen production.[37, 38] However, the field is rapidly evolving, and considerable improvements are expected in the future.

b) Photoelectrochemical H_2 Generation

Like photocatalytic systems, photoelectrochemical H_2 generation uses semiconductors to absorb solar radiation and generate the potential required for water splitting.[22] However, in photoelectrochemical (PEC) cells, the semiconductor absorber is deposited on a conductive substrate that serves as a photoelectrode which is electrically connected to an auxiliary electrode (usually an electronic conductor). Both electrodes are immersed in an electrolyte, as depicted in Figure 1.1b.[26] Upon solar illumination, half of the water-splitting reaction occurs in one electrode and the other half-reaction in the other electrode.[39] This minor tweak offers several advantages for PEC H_2 generation compared to photocatalytic (PC) systems. For example, in instances where the semiconductor absorber cannot produce enough voltage for water splitting, the additional voltage can be externally supplied either from the electricity grid or via solar panels. This is impossible if the semiconductors are dispersed in an electrolyte as in photocatalytic systems. Furthermore, as the hydrogen and oxygen evolution sites are spatially separated, collecting gases is more accessible without the need for sacrificial agents. Owing to these and other advantages, PEC H_2 generation received considerable research attention for green H_2 generation.[22, 40] It will also be the focus of interest of this thesis.

1.2.1. Working Principle

Semiconductor Electrodes

At the heart of a PEC cell lies a semiconductor that absorbs solar radiation, generates high-energy electrons and utilizes them for H_2O redox reaction.[41] Hence, understanding the optoelectronic properties of semiconductors is essential to determine their suitability to serve as photoelectrodes for water splitting.

The semiconducting property of materials is usually explained via the band theory of solids, as depicted in Figure 1.3.[42] When individual atoms are brought together to form a macroscopic solid, the electronic energy levels form a band of energy continuum. The collective distribution of the valence electrons' energy levels is referred to as the valence band, and that of free electrons' energy levels is referred to as the conduction band. Electrons occupy the energy levels according to Pauli's exclusion principle. The probability of a particular energy level (E) occupied by an electron is given by Fermi-Dirac function (f(E)):[43]

$$f(E) = \frac{1}{e^{(E-\mu)/k_B T} + 1} \tag{1.6}$$

where μ is the chemical potential of electrons, k_B is Boltzmann's constant, and T is the absolute temperature.

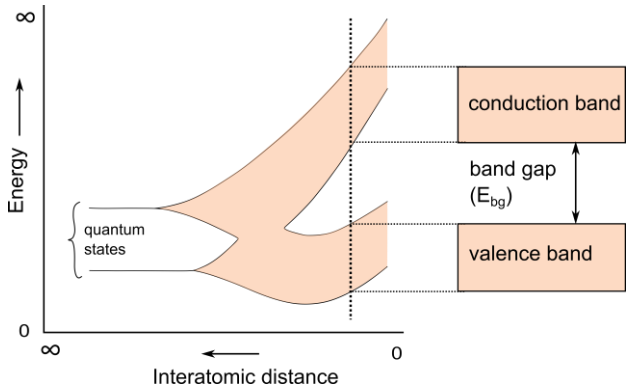

Figure 1.3 Electronic band structure of materials depicting valence band and conduction band formation when individual atoms are brought together to form a bulk solid.

For electrical conductivity (i.e., electron mobility), partially filled energy levels are required. Thus, a mathematically defined energy level where the value of f(E) is 0.5 holds a significant interest which is achieved when E=μ (from Equation 1.6). The distance between this energy level, labelled as the Fermi level (E_F), and the conduction band is often used to interpret the electrical properties of materials.[44] If the Fermi level lies close to the conduction band, the material is expected to display good electrical conductivity (Figure 1.4a). By contrast, insulators' Fermi levels lie further away from the conduction band, i.e., in the middle of a large bandgap (Figure 1.4b). Since the Fermi level is the chemical potential of electrons (i.e., E=μ), it is also the equilibrium energy of electrons in the material. These two definitions are interchangeably used throughout the thesis.

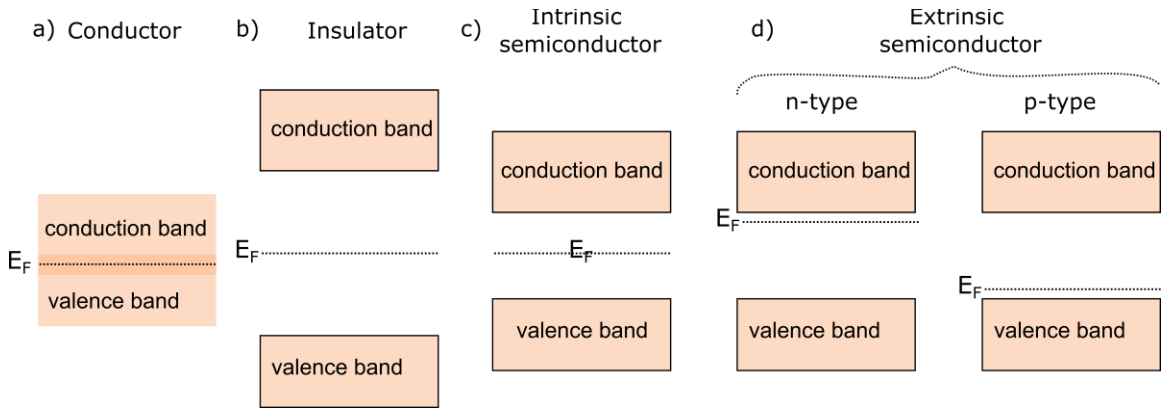

Figure 1.4 Classification of electronic properties of materials based on Fermi level (E_F) positions along with the valence and conduction band energy levels.

A semiconductor exhibits poor electrical conductivity under normal conditions because of a bandgap between the valence and conduction band; E_F lies in the middle of the bandgap (Figure 1.4). However, owing to the smaller bandgap of the semiconductors compared to insulators, the electrical conductivity can be improved by adding dopant atoms i.e., the E_F of semiconductors can be moved towards the conduction band or valence band by adding electron-donating or electron-accepting atoms, respectively.[45] These types of externally doped semiconductors are termed *extrinsic semiconductors,* and doping of silicon (group IV element) semiconductor with boron (group III) or phosphorous (group V) to achieve p-type and n-type conductivity, respectively, is a classic example.

Owing to the small bandgap of the semiconductors, electrons in the valence band can be excited to the conduction band by providing external energy (such as thermal, optical, or electrical) greater than the bandgap; this electronic excitation process is used in solar energy conversion devices.[3] The solar spectrum consists of 43% visible radiation (400–700 nm), 5% UV radiation (300−400 nm), and 52% of infrared radiation (700−2500 nm).[46] The energy associated with photons of a specific wavelength is well defined and given as:

$$E = \frac{hc}{e\lambda}\ (eV) \tag{1.7}$$

$$E = \frac{\left(6.6\times10^{-34}\ J\,s\right)\left(3\times10^{8}\ m\,s^{-1}\right)}{\left(1.6\times10^{-19}\ V\right)\left(\lambda\ \times10^{-9}\ m\right)} = \frac{1237.5}{\lambda\ (nm)}eV \tag{1.8}$$

where h is Planck's constant, c is the speed of light, e is the electronic charge, and λ is the wavelength of photons. An electron can be excited across a bandgap of 1.7 eV using photons with wavelength 728 nm and lower, as per Equation 1.7. Upon solar illumination, photons that have energy greater than the bandgap will get absorbed by the semiconductor and the semiconductor undergoes excitation. Photons with energy less than the bandgap will not excite the semiconductor. This plays a key role in selecting semiconductors for water splitting applications, and more details are discussed in Chapter 2.

Aqueous Electrolytes

A water-splitting reaction consists of two partial reactions. One of the partial reactions is the oxygen evolution reaction ($H_2O \rightarrow O_2 + 4H^+ + 4e^-$) (OER). This is also referred to as an *'anodic reaction'* and produces four protons (H^+) and four electrons (e^-). The other reaction is the hydrogen evolution reaction ($4H^+ + 4e^- \rightarrow 2H_2$) (HER), a *'cathodic reaction'* that occurs spatially at a different location than the OER, as shown in Figure 1.5. A water-splitting reaction is considered complete only when the two partial reactions occur; this requires electrons and protons to be transferred from the anode to the cathode or vice versa. Electronic transport between the anode and cathode is achieved by connecting the electrodes via an external electronic conductor, usually a metal wire (Figure 1.5). For proton or hydroxide ion transport, the ionic conductivity of the water must be increased. Pure water is not an ionic conductor (note: water molecules can undergo self-ionization and produce hydronium (H_3O^+) and hydroxide (OH^-) ions, i.e., $2H_2O \rightleftharpoons H_3O^+ + OH^-$. This may increase the measured ionic conductivity momentarily. However, the products recombine back to water molecules within picoseconds. Hence ionic conductivity resulting from the self-ionization of water is considered negligible.) To increase the ionic conductivity of water, compounds that dissociate into ions, such as H_2SO_4, NaOH, and $FeCl_2$, are added, and the resultant solution is referred to as '*electrolyte*'.

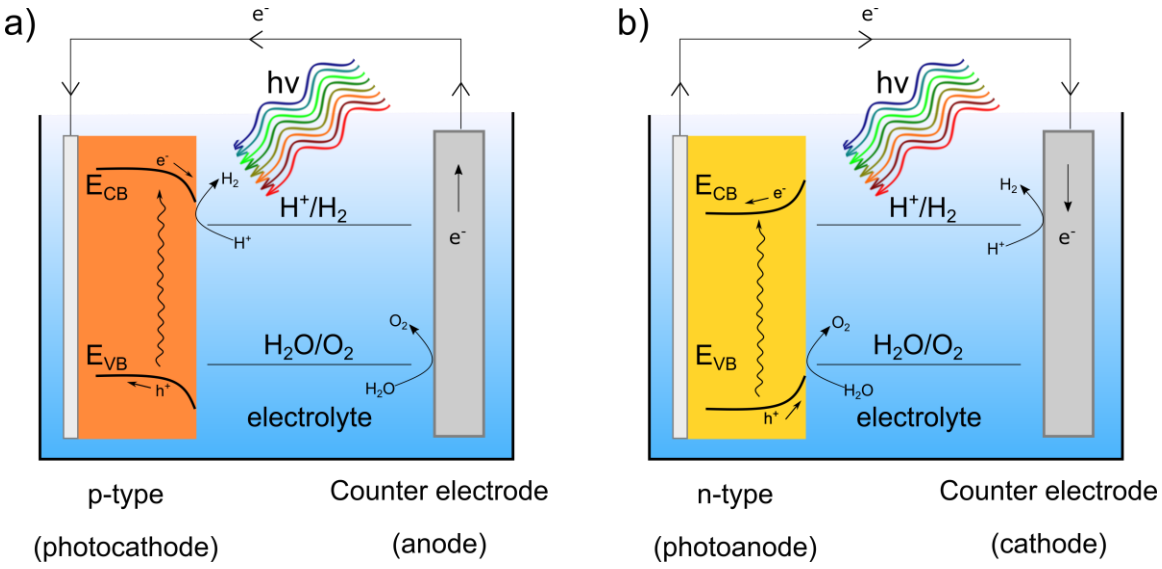

Figure 1.5 Schematic light interaction and electron transport pathways of (a) photocathode (p-type semiconductor), and (b) photoanode (n-type semiconductor) based photoelectrochemical hydrogen generation device.

An electrolyte is a medium that consists of charged species (anions and cations) that will respond to the applied electric potential. Potential is usually applied via two electrodes connected to a power source which are also immersed in the electrolyte. Upon potential application, positive charges in the electrolyte (cations) migrate towards the negative electrode, and negative charges in the electrolyte (anions) migrate towards the positive electrode. The cations consume electrons from the negative electrode and undergo a reduction reaction; the anions donate electrons to the positive electrode and undergo an oxidation reaction. The ions can only accept or donate electrons at a particular potential or higher, inherent to each ionic species known as the redox potential.[47] For example, the reduction of ferrous ions (Fe^{2+}) to iron atoms ($Fe^{2+}+2e^{-}\rightarrow Fe$) occurs at a potential of −0.44 V which is the standard redox potential of the Fe^{2+}/Fe electrochemical reduction reaction. The reaction is not feasible at a potential less than the redox potential. This redox potential of ions is measured with respect to the redox reaction of protons to hydrogen ($2H^{+}+2e^{-}\rightarrow H_2$), which is taken as zero and serves as a reference value (standard hydrogen electrode, SHE), against which all electrochemical potential values are typically reported.

The redox potential is usually reported assuming standard conditions i.e., unit concentration, temperature, and pressure. Redox potential for non-standard conditions is calculated using the Nernst equation:[48]

$$Ox + ne^- \rightleftharpoons Red \quad \left(E = E_{redox}\right) \tag{1.9}$$

$$E_{redox} = E^{o}_{redox} - \frac{RT}{nF} \ln\left\{\frac{a_{Red}}{a_{Ox}}\right\} \tag{1.10}$$

where R is gas constant (8.314 J K^{-1} mol^{-1}), T is temperature, n is the number of electrons involved in the redox reaction, F is Faraday's constant (96485 C/mol), 'a' is activity (or concentration) of the species, and E_{redox} is standard reduction potential.

Semiconductor-Electrolyte Interface

It is good to understand the electrode-electrolyte interface in general before describing the semiconductor-electrolyte interface. The surface of an electrode is negatively charged as electrons can tunnel to a distance of ~0.1 nm outside the surface in a vacuum.[49] Upon being immersed into an electrolyte, the electrode surface is covered with surface charges comprising of water molecules, positively charged cations, and chemisorbed anions. This layer is referred to as the inner Helmholtz plane (IHP) (Figure 1.6).[50] Adjacent to this positively charged layer, negative charges accumulate due to attractive forces. The width of the negative layer is dependent on the concentration of the electrolyte. If the electrolyte concentration is high, the negative layer will form a compact plane (known as the outer Helmholtz plane).[51] For the case of low electrolyte concentration, the negative layer comprises distributed charges and forms diffused double layer, also known as the Gouy layer. The Gouy layer is usually ignored when the electrolyte concentration is high. So, in short, at the electrode/electrolyte interface there exists a zone of charge separation (comprising IHP and OHP, separated by a distance of 0.3 nm) forming a 'double layer' or 'electrical double layer' that is analogous to parallel plate capacitor with capacitance C_{dl}.[49]

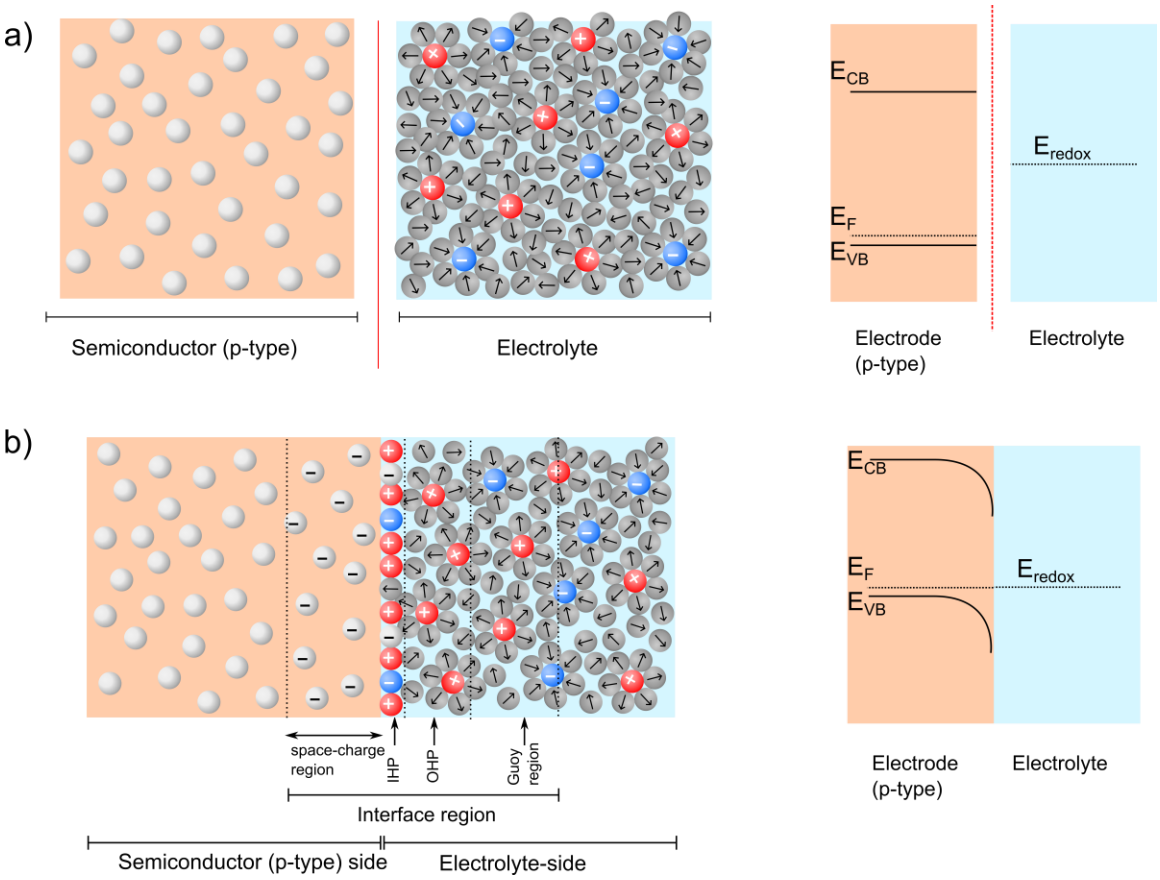

Figure 1.6 Schematic depiction of an electrode (p-type semiconductor)-electrolyte interface a) before and b) after contact, and their corresponding energy level diagram indicating Helmholtz double-layer and space-charge region.

When a semiconductor is immersed in an electrolyte, the two phases try to attain equilibrium, i.e., equilibrium potential of the semiconductor (Fermi level (E_F)) and equilibrium potential of the electrolyte (redox potential (E_{redox})) will try to attain the same energy level.[39] This is achieved by charge transfer across the semiconductor/electrolyte interface (note: this charge transfer occurs in the absence of external potential). As semiconductors usually have a smaller number of mobile charges per unit volume than an electrolyte, to attain equilibrium, charges from the bulk of the semiconductor, 100–10000 Å deep from the semiconductor/electrolyte interface, migrate to the electrolyte.[52] This leaves the semiconductor near the interface depleted of majority charge carriers, and the region is referred to as the depletion region or space-charge region. The depletion region in the semiconductor and a charged layer at the interface) act as a double layer, and its capacitance is known as space-charge capacitance (C_{SC}).[46, 52]

Thus, a semiconductor-electrolyte interface contains two capacitors i.e., double-layer capacitance (Helmholtz double layer, C_{dl}) and space-charge capacitance (C_{SC}) connected in series. The total capacitance (C_{tot}) at the semiconductor-electrolyte interface is given by Equation 1.11. However, as the thickness of the Helmholtz layer is very small compared to the thickness of the space-charge layer, the value of $1/C_{dl}$ is negligible (as capacitance is inversely proportional to the thickness). Hence, the total capacitance (C_{tot}) at the semiconductor/electrolyte interface is assumed to be represented only by the space-charge capacitance (C_{SC}).[52]

$$\frac{1}{C_{tot}} = \frac{1}{C_{SC}} + \frac{1}{C_{dl}} \tag{1.11}$$

Photoelectrochemical H_2 Generation Mechanism

Upon illumination of the space-charge (or depletion) region with photons having energy greater than the semiconductor bandgap (E_{bg}), the electrons in the valence band absorb photons and excite to the conduction band leaving behind a positively charged 'hole.' This energy transition is known as *excitation.* The excited charges typically diffuse to a certain distance (carrier diffusion length, L_D) and then relax to the valence band by releasing the absorbed energy. The time taken by the excited charges to recombine with a hole is termed exciton recombination time (τ) and related to L_D as:[43]

$$L_D \simeq (D\tau)^{\frac{1}{2}} \tag{1.12}$$

where D and τ are excited charges' diffusion coefficient and lifetime, respectively.

However, if the electronic excitation occurs in the depletion region, the photogenerated electrons and holes get separated due to the presence of the internal electric field. Minority carriers drift towards the surface of the semiconductor, while majority carriers drift towards the bulk of the semiconductor. The minority carriers at the surface participate in the redox reaction, and the majority carriers move towards the back of the semiconductor, which are then transported to the counter electrode where they will participate in the balance half of the electrochemical reaction. Hence p-type semiconductors act as photocathodes where minority electrons participate in HER, and n-type semiconductors act as photoanodes where the minority holes participate in OER, as schematically depicted in Figure 1.5.[53]

For a water-splitting reaction to occur, excited charges must have energy higher than that is required for a particular redox reaction, i.e., the CB (or VB) energy levels of the photocathodic (or photoanodic) semiconductor must be higher (or lower) than the HER (or OER) redox potential.[54] The standard redox potentials for water splitting reactions are given below:

Hydrogen evolution reaction (HER):

$$2H^+ + 2e^- \longrightarrow H_2 \ (E_{H^+/H_2} = 0 \ V_{SHE}) \text{ (in acidic electrolyte)} \quad (1.13)$$

$$2H_2O + 2e^- \longrightarrow H_2 + 2OH^- \ (E_{H_2O/H_2} = -0.83 \ V_{SHE}) \text{ (in alkaline electrolyte)} \quad (1.14)$$

Oxygen evolution reaction (OER):

$$2H_2O \longrightarrow O_2 + 4H^+ + 4e^- \ (E_{H_2O/O_2} = 1.23 \ V_{SHE}) \ (\text{in acidic electrolyte}) \quad (1.15)$$

$$4OH^- \longrightarrow O_2 + 2H_2O + 4e^- \ (E_{OH^-/O_2} = 0.40 \ V_{SHE}) \text{ (in alkaline electrolyte)} \quad (1.16)$$

In addition to the band edge position of a semiconductor with respect to water redox energy levels, the applicability of a semiconductor for water splitting is often described using photovoltage and photocurrent. Photovoltage is the electric potential generated by a semiconductor due to light absorption and is the driving force for water splitting. Ideally, photovoltage of more than 1.23 V is necessary for a water-splitting reaction to occur. The maximum photovoltage that can be obtained from the given semiconductor/electrolyte combination is the difference between E_F of the electrode and E_{redox} of the electrolyte.[55]

$$V_{max} = \left| \left(E_F - E_{redox} \right) \right| \quad (1.17)$$

Suppose a chosen electrode/electrolyte combination is not capable of generating enough photovoltage for a water splitting reaction. In such a case, two or more semiconductors can be connected to form a heterojunction electrode (Figure 1.7a) in order to achieve the required potential for overall water splitting. Alternatively, one could replace the auxiliary electrode with a suitable photoelectrode (Figure 1.7b) to achieve the same effect. In such instances, each semiconductor electrode is expected to generate only a part of the overall potential required.

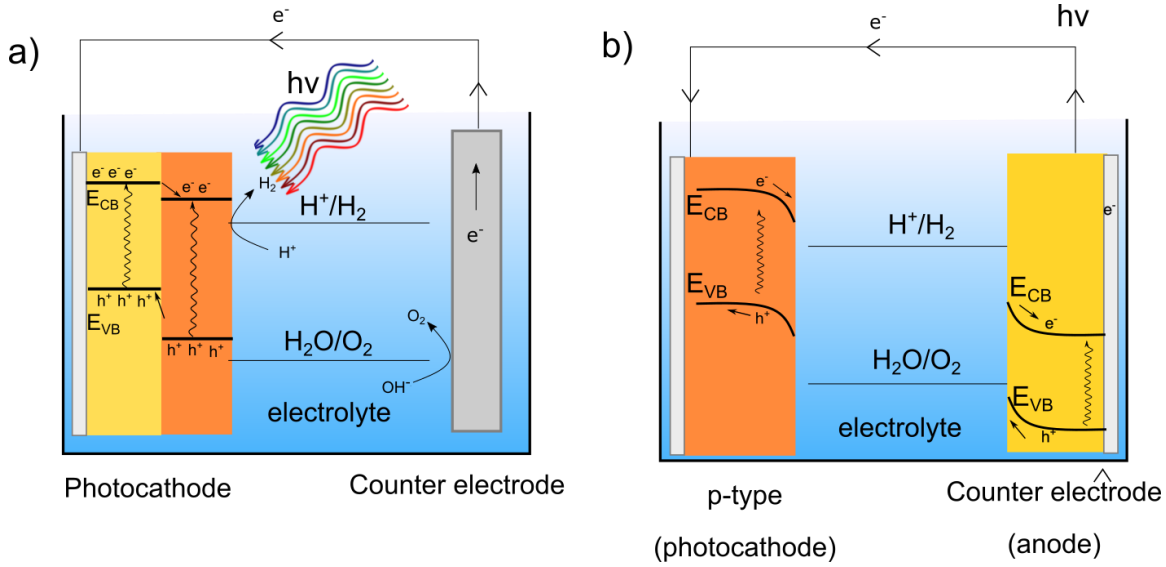

Figure 1.7 **Diagram illustrating (a) band edge positions of a heterojunction photoelectrode and (b) overall water splitting achieved by coupling a photocathode with a photoanode.**

In addition to the photovoltage, a photoelectrode is also expected to produce large numbers of electrons that participate in redox reactions, which can be measured via the electron flow in the external circuit i.e., photocurrents. Higher photocurrents, in ideal situations, translate to higher hydrogen evolution. Photocurrents are directly proportional to the illumination intensity, absorption coefficient, charge carrier density (N), photopotential (E_{ph}), etc.[55] It should be noted that not every photoelectron that is generated will participate in the electrochemical reaction that results in H_2. The electrons may participate in other (photo)electrochemical reactions if extraneous redox potentials lie within the water redox potentials (explored in detail in Chapter 4). Hence, in addition to the photocurrent measurement, it is imperative to verify that electrons consumed in redox reactions are translated to H_2.

To summarise, an ideal semiconductor photoelectrode must possess (i) band edges that straddle water redox potentials, (ii) low bandgap to absorb maximum solar radiation, (iii) generate high photovoltage, (iv) convert the absorbed radiation to photocurrent with minimum recombination, (v) catalytically active towards HER (for photocathode) and OER (for photoanode) reactions, and (vi) be stable in the electrolyte employed without loss in performance. Hence to validate the suitability of a photoelectrode, a wide variety of characterization tools are employed.

1.3. Characterization of Photoelectrodes

The ability of a photoelectrode to absorb maximum solar radiation and convert it into hydrogen plays a crucial role in the selection of photoelectrodes for water splitting. Different parameters such as bandgap, photovoltage, photocurrent, onset potential, faradaic efficiency, and solar-to-hydrogen conversion efficiency provide insights into the photophysical and electrochemical properties of a photoelectrode. Measurement of these parameters plays a crucial role in determining the suitability of any newly developed photoelectrode.

1.3.1. Ultraviolet-Visible Spectroscopy

Ultraviolet-Visible (UV-Vis) spectroscopy is used to measure the light absorbed by the electrode in which light of known intensity (I_o) is allowed to pass through the sample and transmitted light intensity (I) is measured. From the initial and final light intensities, the absorption (A) of the material is determined using the following equation:

$$A = -\log_{10}\left(\frac{I}{I_o}\right) \tag{1.18}$$

As absorption is dependent on the bandgap of the semiconductors, from the absorption measurements bandgap can be estimated using the Tauc relation.[56]

$$(\alpha h\nu)^n = k\left(h\nu - E_g\right) \tag{1.19}$$

where α is the absorption coefficient (obtained by normalizing the absorption A to film thickness), h is Planck's constant, v is the frequency of the incident light, k is the constant of proportionality, and E_g is the bandgap of the semiconductor. A value of ½ or 2 is assigned to 'n' depending on the direct or indirect electron transition nature of the semiconductor, respectively. By extrapolating the $(\alpha h\nu)^n$ values to the baseline in the Tauc plot, the semiconductor's bandgap is estimated (Figure 1.8).[57] For opaque samples, absorption coefficient (α) is calculated from the diffuse reflectance measurements using Kubelka-Munk radiative transfer model.[58, 59]

$$f(R) = \frac{(1-R)^2}{2R} = \frac{\alpha}{s} \tag{1.20}$$

where f(R) is the Kubelka-Munk absorbance function, R is the reflectance, α is the absorption coefficient, and s is the scattering factor which is assumed to be wavelength-independent. After obtaining the absorption coefficient from the Kubelka-Munk function, the bandgap of the samples is calculated using the Tauc relation as outlined above.[32]

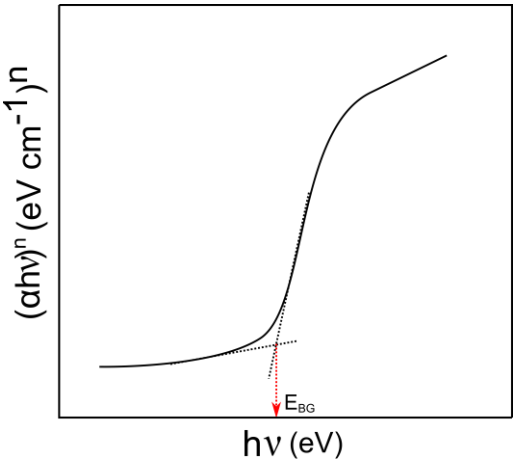

Figure 1.8 Schematic representation of the Tauc plot to calculate semiconductor bandgap.

1.3.2. Photoelectrochemical Characterization

A water-splitting device consists of two electrically connected electrodes (anode and cathode) immersed in an electrolyte, as depicted in Figure 1.7. However, often it becomes necessary to understand the performance of a photoelectrode even when the electrode does not generate sufficient photovoltage for further improvement and when the electrode is expected to be used in a heterojunction. Since the performance of these electrodes cannot be evaluated in a two-electrode setup, a three-electrode electrochemical setup is used. The three-electrode setup consists of a photoelectrode of interest (working electrode), an inert counter electrode, and a reference electrode (of known potential) submerged in an electrolyte, as shown in Figure 1.9. A solar simulator, typically representative of solar irradiation on earth level (AM 1.5G solar spectrum, 100 mW cm^{-2}), is used as a light source in photoelectrochemical measurements. The additional voltage necessary to carry out the water-splitting reaction is provided via a potentiometer.

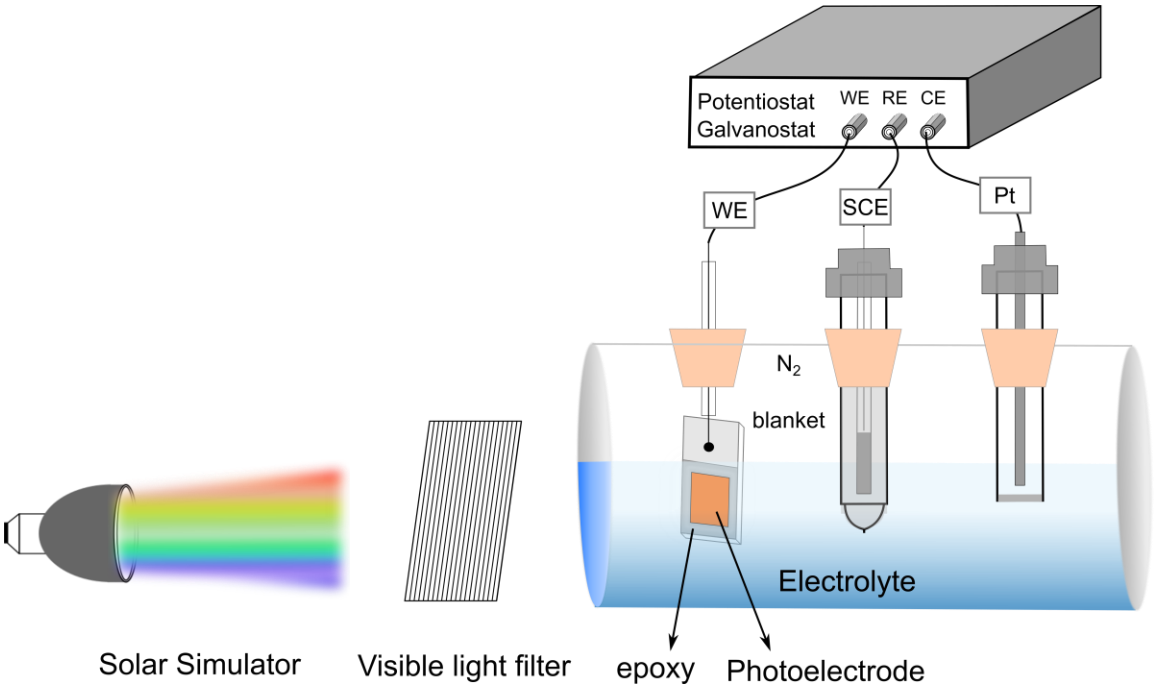

Figure 1.9 **A three-electrode photoelectrochemical set-up with a working electrode (photoelectrode), Pt wire counter electrode, and saturated calomel electrode (SCE) as reference electrode immersed in an electrolyte at room temperature.**

Measurement of Photopotential

Open circuit potential (OCP) measurements offer a straightforward way to measure the photopotential (E_{ph}) generated by a photoelectrode. When a semiconductor electrode is immersed in an electrolyte, the Fermi level (E_F) of the former and the redox potential (E_{redox}) of the latter achieve equilibrium by charge transfer across the electrode/electrolyte interface, resulting in a space-charge region (as described in section 1.2.1). The electric potential arising from charge imbalance at the electrode/electrolyte interface is measured as the open-circuit potential (OCP).

For instance, E_F of a p-type semiconductor is lower in energy than E_{redox}; hence, positively charged holes transfer from the electrode to the electrolyte until E_F reaches the same energy level as E_{redox}, as shown in Figure 1.10. This creates a hole-deficient region in the electrode known as the depletion region or space charge region.[60] It can also be viewed as excess negative charges in the electrode and positive charges in the electrolyte. The charge transfer process continues until positive charges in the electrolyte oppose further hole transfer from the electrode, at which point equilibrium is reached, and net charge transfer across the interface becomes nil.

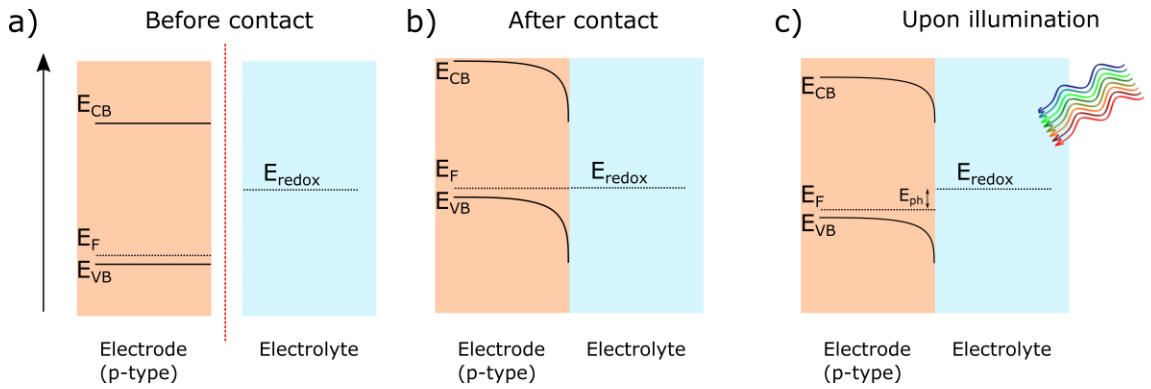

Figure 1.10 Band edge positions of a p-type semiconductor electrode and electrolyte (a) before contact, (b) after contact where equilibrium is attained between the electrode and electrolyte, and (c) upon illumination depicting partial unbending of the bands.

The potential built-up at the electrode/electrolyte interface is measured as the open-circuit potential (OCP). Note that this potential arises due to the equilibration process and without illumination. When the semiconductor is illuminated by light, electrons and holes generated within the space-charge region are separated due to the presence of an internal electric field. The resulting photogenerated electrons (holes) are transferred to the solution, and holes (electrons) accumulate in the semiconductor for p-type (n-type) semiconductors (Figure 1.10). These newly generated charge carriers change the OCP values, and the difference in OCP before and after illumination represents photopotential (E_{ph}) generated by the photoelectrode.[10, 61]

$$E_{Ph} = \left| E_{OCP,dark} - E_{OCP,light} \right| \quad (1.21)$$

A typical OCP graph of a photocathode is shown in Figure 1.11. E_{OCP} under dark signifies the potential that is spontaneously established at the electrode/electrolyte interface upon the immersion of the electrode in the electrolyte. After illumination, E_{OCP} shifts to a more positive potential due to the generation of additional charge carriers (i.e., band bending), characteristic of a p-type photoelectrode. The difference in E_{OCP} measurements under dark and light conditions provides information about the electronic charges generated upon illumination. After the light is turned off, the charges recombine, and the open circuit potential decays to the pre-illumination level. The time taken for the open circuit potential to reach the pre-illumination level provides information about electron-hole recombination i.e., exciton lifetime (τ).[62, 63] The shorter the time taken by OCP to reach the pre-illumination level indicates faster electron-hole recombination.

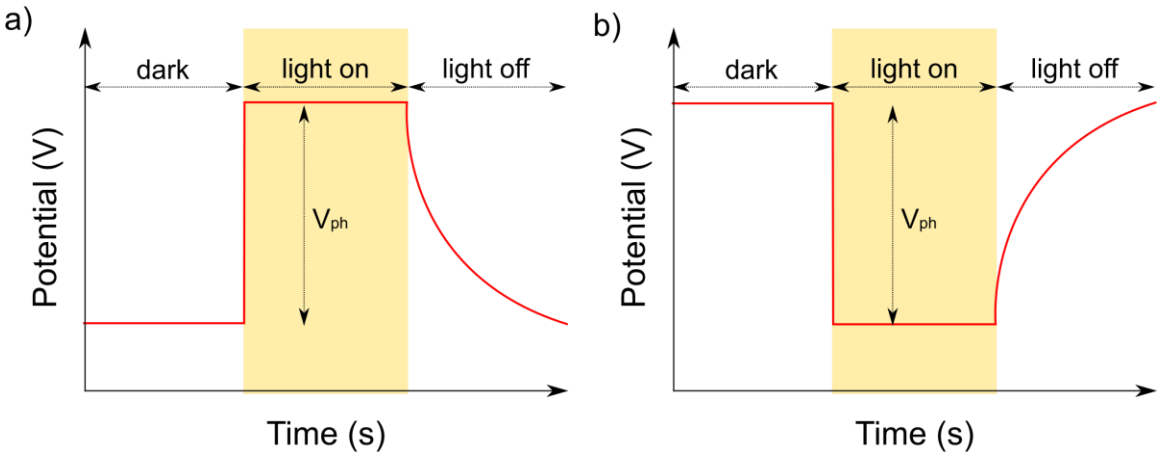

Figure 1.11 Schematic of typical open circuit potential graph (red) of (a) p-type photocathode and (b) n-type photoanode measured under dark and illumination. A positive (or negative) shift in OCP upon illumination indicates a p-type (or n-type) semiconducting characteristic.

Photoelectrolysis via Linear Sweep Voltammetry

Most semiconductor electrodes often do not produce enough photopotential to split water (>1.23 V) and warrant external potential. In such instances, external potential bias is necessary to understand the behaviour of electrodes in the potential region that is unavailable to study in an unbiased electrode. For this, potentiometry is often employed where a controlled amount of external potential is applied, and the current response is recorded. A typical graph of linear sweep voltammetry (LSV) for a p-type photoelectrode under dark and illuminated conditions along with the semiconductor band energy positions is depicted in Figure 1.12. The dark current (j_{dark}) represents electron flow across the electrode/electrolyte interface in the absence of illumination. At a particular applied potential, termed flat band potential (E_{FB}), band bending caused by semiconductor-electrolyte equilibration is removed and the bands become flat (Region III in Figure 1.12). At potentials negative of the E_{FB}, as the semiconductor is depleted of majority charge carriers, minimal currents are observed (Regions I and II in Figure 1.12). When the applied potential is higher than the E_{FB}, the semiconductor acts as a conductor as large numbers of majority charge carriers are introduced in the space-charge region (Region IV, in Figure 1.12).[52]

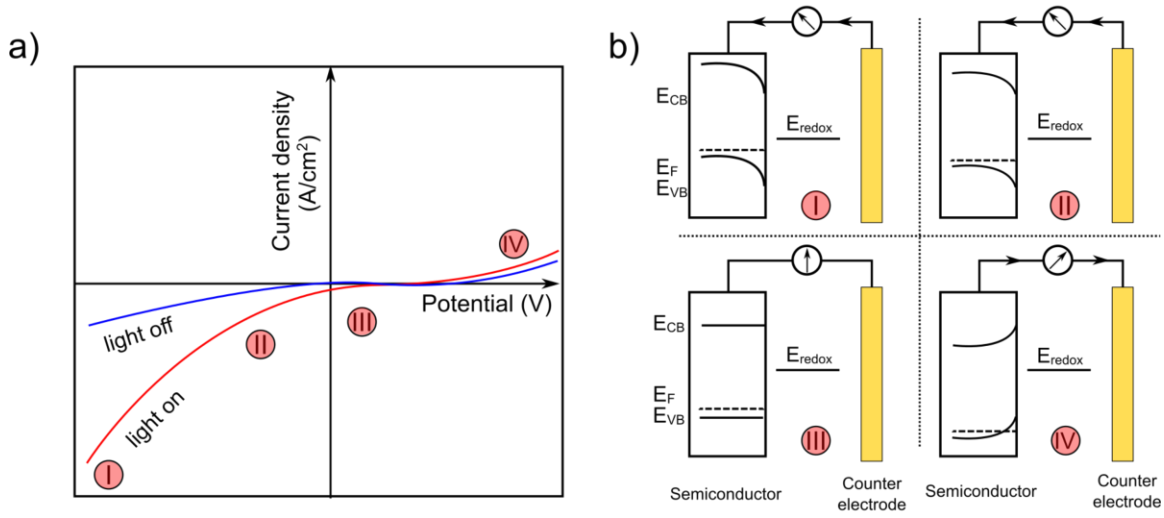

Figure 1.12 Graphical representation of (a) continuous linear sweep voltammetry (LSV) graph of typical p-type photoelectrode (photocathode) measured under dark and light conditions depicting depletion (I and II), the flat band (III), and accumulation (IV) conditions of the photoelectrode, and (b) the corresponding band edge positions.

When performed under illumination, the measured current is termed light current (j_{light}), and the difference between dark current and light current is photocurrent. Upon illumination, photocurrent increases as excitons are efficiently separated due to the internal electric field in the depletion region. Thus, two measurements are required to understand the photoelectrode's performance, i.e., LSV_{dark} and LSV_{light}. However, high applied potential during the first measurement might modify the electrode surface, which in turn would affect the second LSV measurement. Hence LSV measurements are usually conducted in an intermittent manner with alternating dark and light cycles, and the experiment is carried out only once per sample (Figure 1.13).

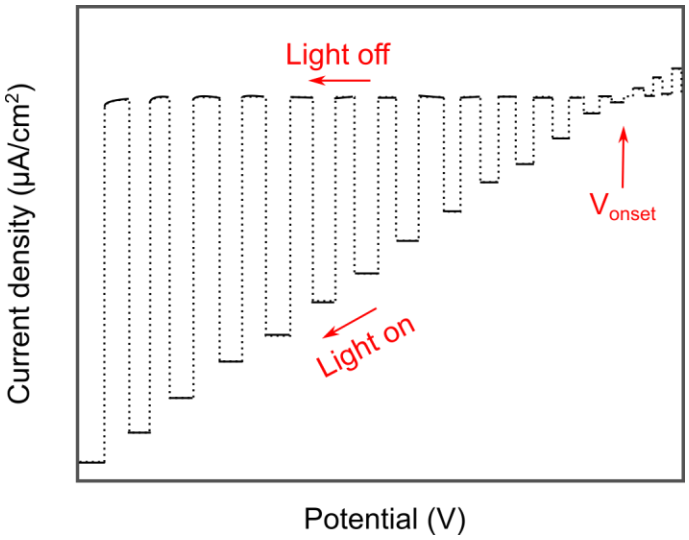

Figure 1.13 **Graphical representation of typical photoelectrolysis graph of p-type photoelectrode with alternate dark (blue) and illumination (red) conditions. The negative shift in photocurrent upon illumination represents the p-type semiconducting nature of the electrode, and minority carriers (electrons) flow across the electrode/electrolyte interface.**

1.3.3. Electrochemical Characterization Tools

Electrochemical Impedance Spectroscopy

Similar to the polarization techniques described in the previous section, electrochemical impedance spectroscopy (EIS) measurement is also a tool to perturb electrochemical systems and understand electron transport characteristics.[64] The electrode/electrolyte assembly in an electrochemical cell emulates the characteristics of electrical elements such as a resistor, capacitor, and inductor. For example, an electrode immersed in an electrolyte can be modelled by an electrical circuit, as shown in Figure 1.14a. The resistance offered by the electrode, electrolyte, and electrode/electrolyte interface for charge transportation is represented by resistors R_{film}, R_s, and R_{CT}, respectively. The presence of a double layer at the interface is accounted for by a capacitor (C_{dl}) connected in parallel with R_{CT}. Impedance (Z) is the measure of total resistance offered by these electrical elements to the flow of an alternating current (AC).

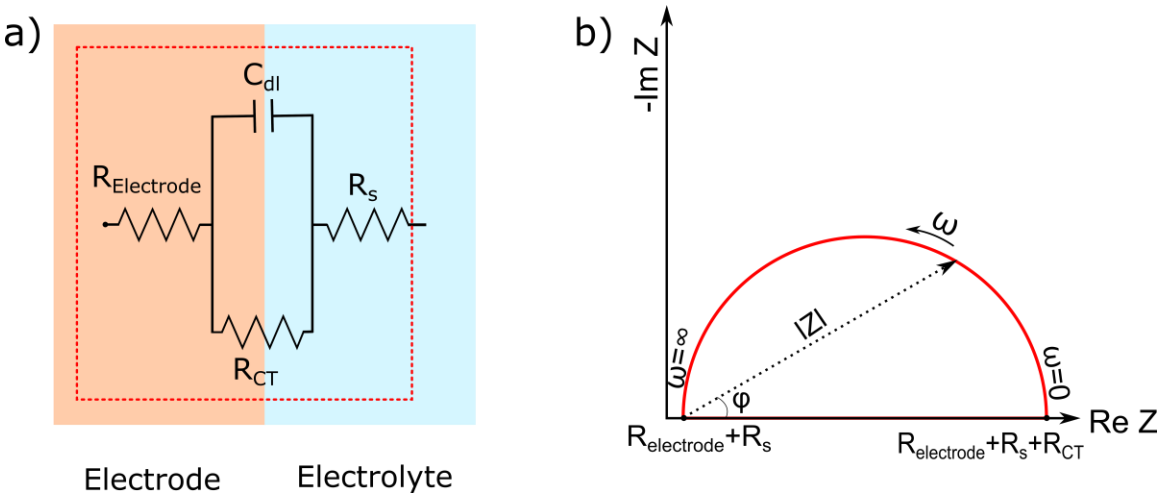

Figure 1.14 (a) Equivalent electrical circuit representing electrode-electrolyte interface[49], and (b) the corresponding Nyquist impedance plot for the depicted electrical circuit.

The EIS probes an electrochemical system using low amplitude alternating current (AC) at different frequencies. For the applied sinusoidal potential E_t, the measured current response I_t is given as:

$$E_t = E_o \sin(\omega t) \tag{1.22}$$

$$I_t = I_o \sin(\omega t + \phi) \tag{1.23}$$

where E_t and I_t are potential and current at time t, respectively. E_o and I_o are the amplitude of the sinusoidal signal, ω (=2πf) is the radial frequency, f is the frequency of the sinusoidal wave, and ϕ is the phase shift (i.e., the difference in phase between the sinusoidal potential and current). From the applied potential and measured current, impedance can be calculated. The impedance of common circuit elements is given below:

Resistor : $Z = R + 0i$ and $\phi = 0$ (1.24)

Capacitor : $Z = 0 + \frac{1}{i\omega C}$ and $\phi = -90^{\circ}$ (1.25)

Inductor : $Z = 0 + i\omega L$ and $\phi = 90^{\circ}$ (1.26)

where i is the imaginary component of the impedance. For direct current, resistance is calculated (according to Ohm's law) from the slope of a straight line when potential and

current are plotted on the X and Y-axes, respectively. When a sinusoidal signal is represented on the X and Y-axis, the resulting shape is not a straight line but an oval shape (known as the Lissajous figure). This shape is represented as a complex function, and hence impedance response contains both real and imaginary parts. For the electrical circuit depicted in Figure 1.14b (highlighted), impedance is given as:[65]

$$Z = R_s + R_{electrode} + \frac{1}{\frac{1}{R_d} + i\omega C_{dl}} \tag{1.27}$$

The measured impedance data is plotted either in polar (r, θ) coordinate or cartesian (x, y) coordinate. In the case of the former, the plot is referred to as the Nyquist plot (|Z|, Φ), and the latter is known as the Bode plot ((*f*, |Z|), and (*f*, Φ)). Nyquist plot for the electrical circuit is shown in Figure 1.14b. At low frequencies, the impedance of the circuit equals to $R_{electrode}+R_{CT}+R_s$ (according to Equation 1.27). At high frequencies impedance of the capacitor becomes very low that $R_{electrode}+R_s$ approximate the total impedance of the circuit. By keeping the ionic conductivity of the solution high, the R_s term becomes negligible, and the measured impedance represents electrode resistance ($R_{electrode}$). Thus, by varying the frequency of the AC signal and appropriately fitting the equivalent circuit, different physical properties of an electrochemical system can be extracted. A more detailed explanation of impedance spectroscopy and its application can be found in the literature.[65, 66]

Mott-Schottky Analysis

Mott-Schottky (M-S) analysis is a tool to probe electronic properties such as semiconducting type (p-type or n-type), donor or acceptor carrier concentration (N_a or N_d), and flat band potential (E_{FB}) of a semiconductor photoelectrode used as an electrode in an electrochemical cell. As described in section 1.3.2, the space-charge region arises during the energy level equilibration between the semiconductor Fermi level (E_F) and E_{redox} of an electrolyte (Figure 1.15a), and E_F of an electrode can be influenced by applying external stimulus such as light or electrical potential. In M-S analysis, E_F is varied by applying external potential, and the resultant effect on the space-charge region is reflected in space-charge capacitance values.[52] The M-S equation (Equation 1.28) relates the space-charge capacitance to the semiconducting characteristics. Thus by measuring the

space-charge capacitance, carrier density of a semiconductor and flat band potential can be calculated using the Mott-Schottky equation:[52, 53]

$$\frac{1}{C^2} = \left(\frac{2}{\varepsilon_o \varepsilon e N A^2}\right)\left(E - E_{FB} - \frac{k_B T}{e}\right) \tag{1.28}$$

$$\text{M-S}_{\text{slope}} = \left(\frac{2}{\varepsilon_o \varepsilon e N A^2}\right) \tag{1.29}$$

where ε_o is the permittivity of free space (8.85×10^{-14} F cm^{-1}), ε is the dielectric constant, and *A* is the area of semiconductor in contact with the electrolyte, *e* is the electronic charge (1.6×10^{-19} C), *N* is donor or acceptor density, k_B is Boltzmann constant, and T is temperature. At room temperature, the term kT/e is approximately 25 mV.

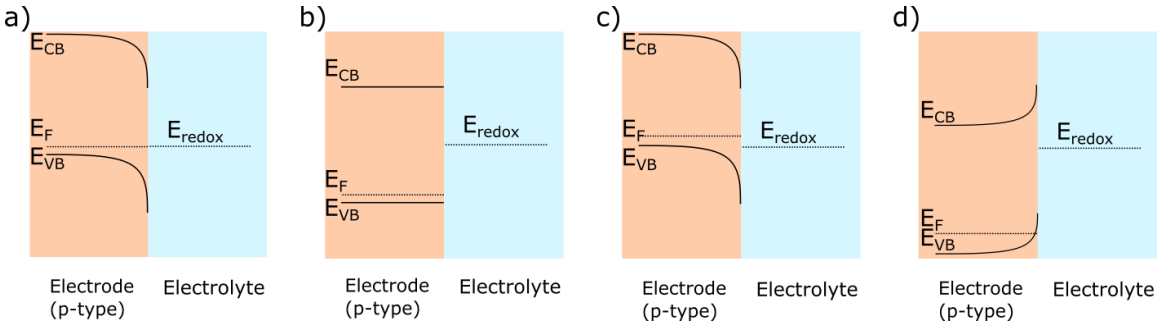

Figure 1.15 Effect of applied potential on valence and conduction band energy levels of a p-type semiconductor when (a) no potential, (b) $E=E_{fb}$, (c) $E<E_{fb}$, and (d) $E>E_{fb}$ corresponding to (a) equilibrium, (b) flat band, (c) depletion, and (d) accumulation conditions in the space-charge region, respectively.

M-S experiment is performed by applying a potential range and measuring the corresponding capacitance (C^{-2}) values which results in a straight line according to Equation 1.28. Positively sloped lines are obtained for n-type semiconductors, and negatively sloped lines are obtained for p-type semiconductors. From the value of the slope (Equation 1.29), charge carrier density (N), and from the intercept of the slope with the potential axis, the flat band potential (E_{FB}) of the semiconductor is calculated.[67] Thus, Mott-Schottky analysis provides a simple way to characterize the semiconducting properties of a photoelectrode.

1.3.4. Quantification of Hydrogen

Gas chromatography (GC) plays a significant role in identifying and quantifying evolved hydrogen from the photoelectrochemical reactor. The efficiency of a photoelectrode is dependent on two energy conversion steps: (i) solar-to-electron conversion and (ii) electron-to-hydrogen conversion. For efficient energy conversion, all the photoelectrons generated due to incident solar energy must be converted to hydrogen and not participate in any unwanted physical or electrochemical processes. GC helps in measuring the evolved hydrogen and thus, in determining the solar-to-hydrogen conversion efficiency.

The GC consists of a 'stationary phase': a small diameter tube with inner walls coated with viscous liquid. The tube is also known as the 'column.' The sample (containing hydrogen) to be analyzed along with a carrier gas (nitrogen) is injected into the column. This mixture is termed as 'mobile phase.' Based on the interaction of the sample with the stationary phase, separation of different gases occur.[68] Retention time of the gases depends on vapour pressure, column temperature, carrier gas flow rate, column length and concentration of the sample, etc. However, with all the other parameters remaining constant, retention time is proportional to the strength of the interaction. Strong interactions result in higher retention time. This difference in the rate of progress of different gases is used to identify the gases present.

Faradaic efficiency is defined as the ratio of measured hydrogen to that of theoretically expected hydrogen from the photocurrent measurements. This indicates the electron-to-hydrogen conversion efficiency of the photoelectrodes.

$$\text{Faradaic efficiency } (\eta_F) = \frac{H_2\ (\text{measured})}{H_2\ (\text{theoretical})} \times 100\% \tag{1.30}$$

$$\text{Faradaic efficiency } (\eta_F) = \frac{H_2\ (\text{measured})}{\left(\frac{j_{photo} \times A \times t}{2 \times e \times N_A}\right)} \times 100\% \tag{1.31}$$

where j_{photo} is the photocurrent density (A cm^{-2}), A is the photoelectrode area (cm^{-2}), N_A is Avogadro's constant (6.02 x 10^{23} mol^{-1}), and e is the electronic charge (1.602 x 10^{-19} C) of an electron.

1.3.5. Definition of Efficiency

A photoelectrode is expected to be as efficient as theoretically possible. However, practical efficiency is usually much lower than the theoretically predicted values due to several constraints and limitations. For example, energy losses associated with exciton recombination, electrode resistance, overpotential requirement, and poor catalytic activity are typically common. Hence, it is important to calculate the electrode efficiency for comparison against benchmark efficiency and other photoelectrodes. A typical performance of a photoelectrode is defined using the solar-to-hydrogen (STH) conversion efficiency (Equation 1.32), which is the ratio of energy required to release the measured hydrogen to the total energy in the input solar radiation.[53]

$$\mathrm{STH} = \left(\frac{\mathrm{mmol}\ \left(\mathrm{H_2\ s^{-1}}\right) \times 237\ \left(\mathrm{kJ\ mol^{-1}}\right)}{\mathrm{P_{total}}\ \left(\mathrm{mW\ cm^{-2}}\right) \times \mathrm{Area}\ \left(\mathrm{cm^{-2}}\right)} \right)_{\mathrm{AM\ 1.5G}} \times 100\% \tag{1.32}$$

where 237 kJ mol^{-1} is the minimum energy required to dissociate one mole of water and P_{total} is the total power density of incident radiation. Alternatively, in terms of measured photocurrent, Equation 1.32 can also be written as:

$$\mathrm{STH} = \left(\frac{\mathrm{I_{sc}}\left(\mathrm{mA\ cm^{-2}}\right) \times 1.23\ \left(\mathrm{V_{RHE}}\right) \times \eta_F}{\mathrm{P_{total}}\ \left(\mathrm{mW\ cm^{-2}}\right)} \right)_{\mathrm{AM\ 1.5G}} \times 100\% \tag{1.33}$$

Where η_F is Faradaic efficiency for hydrogen evolution. In a few instances, a photoelectrode cannot generate the potential necessary for water splitting and warrant additional external potential (V_b) as a bias. In such instances, the efficiency is calculated as,

$$\mathrm{STH_{bias}} = \left(\frac{\mathrm{I_{sc}}\ \left(\mathrm{mA\ cm^{-2}}\right) \times \left[1.23 - \left|\mathrm{V_b}\right|\right]\ \left(\mathrm{V_{RHE}}\right) \times \eta_F}{\mathrm{P_{total}}\ \left(\mathrm{mW/cm^2}\right)} \right)_{\mathrm{AM\ 1.5G}} \times 100\% \tag{1.34}$$

STH efficiency serves as a benchmark against which the performances of different photoelectrodes are compared. Hence, efficiency measurements are carried out and reported under standard conditions defined in the literature to ensure:[53] (i) no additional energy source is present in the form of thermal or chemical biases, (ii) illumination source

conforms to the AM 1.5G standard, and (iii) the detected H_2 is due to water splitting and not from externally added chemicals.

In addition to the above-mentioned experiments and characterization tools, photoluminescence spectroscopy, photoelectrochemical action spectrum, intensity-modulated photocurrent spectroscopy (IMPS), and intensity-modulated photovoltage spectroscopy (IMVS) are also widely employed. However, for this thesis, the techniques described in section 1.3 are adequate to characterize the synthesized photoelectrodes. In the next chapter, different semiconductor photoelectrodes identified for PEC H_2 generation, and their advantages and limitations are discussed.

Chapter 2.

Photoelectrodes for H_2 Generation

2.1. Semiconductor Photoelectrodes

As discussed in the previous chapter, semiconductor photoelectrodes play a crucial role in PEC hydrogen generation application. A viable semiconductor must possess a low bandgap enabling it to absorb a large portion of the solar spectrum; and have an electronic valence, and conduction band edges straddle the redox potentials associated with oxygen evolution reaction (OER) and hydrogen evolution reaction (HER), respectively.[41] Furthermore, the semiconductor is also expected to process the following sequence of steps efficiently: (i) solar light absorption and exciton generation, (ii) exciton dissociation (charge generation), (iii) charge transport, and (iv) charge transfer to the electrolyte.[10, 27, 69]

Besides the above-mentioned optoelectronic properties, the ideal photoelectrode material must possess good chemical stability, catalytic activity, and nontoxicity, be economically viable to implement on a large scale and be competitive enough with the commercially available techniques for hydrogen generation such as steam methane reforming and electrolysis. Based on these considerations, the US Department of Energy (DOE) has defined a set of desired numerical targets for the photoelectrodes to exhibit as a benchmark (Table 2.1) with an ultimate target of 25% solar-to-hydrogen conversion efficiency and produce hydrogen at the cost of $2 per kg.[41, 70]

Table 2.1 US DOE technical targets for photoelectrochemical hydrogen production.[a]

Characteristics	Units	2015 target	2020 target	Ultimate target
Photoelectrochemical hydrogen cost [b]	$ kg^{-1}	17.30	5.70	2.10
Solar to hydrogen (STH) energy conversion ratio	%	15	20	25
Annual electrode cost per TPD H_2	$ yr^{-1}-TPD H_2	2.0M	255K	14K
1-sun hydrogen production rate	kg s^{-1} m^{-2}	1.2×10^{-6}	1.6×10^{-6}	2.0×10^{-6}
Capital cost of concentrator and PEC receiver	$ m^{-2}	200	124	63

[a] Photoelectrode system with solar concentration
[b] Hydrogen cost represents the complete system hydrogen production cost for purified, 300 psi compressed gas.
TPD - metric tons per day

Semiconductors play a crucial role in absorbing solar energy and generating electronic charges of sufficient energy that are subsequently used in water splitting. The semiconducting behaviour is observed across different types of materials (organic and inorganic), chemical compositions, and crystal structures.[45] From the first modern report of photoelectrolysis in the 1970s by Honda and Fujishima,[71] the scientific literature on photoelectrochemical water splitting is vast. Hundreds of photoelectrodes have been tested using various experimental and theoretical tools.[40, 72, 73] Although a few breakthrough studies are summarized in the following sections, a comprehensive review of recent developments can be found in the literature.[54, 74, 75]

2.2. Organic-based Semiconductor Photoelectrodes

2.2.1. Introduction

A class of materials that has attracted considerable research interest for solar energy conversion research is organic semiconductors. Organic semiconductors offer several advantages over inorganic materials in terms of low density, availability, and ease of processing.[76-79] Furthermore, they can be readily deposited conformally on various substrates by spin coating, dip coating, inkjet printing, and roll-to-roll processing in high volume without the need for prohibitive vacuum coating techniques.[80-82] In organic materials, semiconducting behaviour has been observed in amorphous molecular films (e.g., C_{60}, phthalocyanine), molecular crystals (e.g., anthracene, tetracene), conjugated polymer films (polythiophene, polyphenylenevinylene) and others.[83, 84] These materials are used in applications such as light-emitting diodes, field-effect transistors, and solar cells.[85] A brief description of the working principle of conjugated organic polymers (CP) and their application in photoelectrochemical water splitting is given below.

Organic materials with conjugated bonds (i.e., overlapping p-orbitals arising due to alternating single and double bonds which result in electron delocalization) display semiconducting characteristics and their electrical properties can be modified by adding dopant atoms. For the discovery and development of conductive polymers, Heeger, MacDiarmid, and Shirakawa received the Nobel prize in chemistry in 2000.[86, 87] Conjugation describes resonant interaction between the π-electron orbitals of neighbouring atoms in a molecule which results in electron delocalization. As the number of interacting π-orbitals increases, the discreet molecular π-orbitals form a continuous

band which consequently results in a stronger electron delocalization. The energy gap between the bands comprising π-bonding orbitals and π*-antibonding orbitals form the highest occupied molecular orbital (HOMO) and the lowest occupied molecular orbital (LUMO), respectively (Figure 2.1).[88] For simplicity, the HOMO and LUMO levels are analogous to the valence and conduction bands of inorganic semiconductors. Thus, the bandgap of the organic semiconductors and their optoelectronic properties can be influenced by conjugation length or heteroatoms.

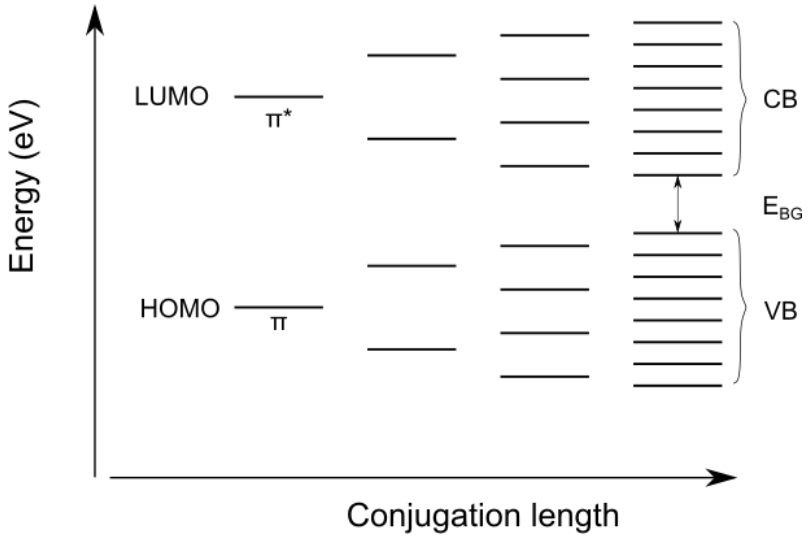

Figure 2.1 Effect of conjugation length on HOMO and LUMO energy levels of conjugated organic semiconductors.

2.2.2. Electronic Processes in Organic Semiconductors

When interacting with electromagnetic radiation of sufficient energy (i.e., energy greater than the corresponding bandgap), organic semiconductors produce exciton, a bound electron-hole pair, wherein an electron in the HOMO energy level is excited to the LUMO level. This leaves behind a positive charge at the HOMO level, which exerts an attractive force on the LUMO electron. Hence, the excited state is meta-stable, and excitons recombine by releasing energy either via non-radiative (such as heat, collision, molecular conformational changes) or radiative processes (such as fluorescence, phosphorescence).[89] Owing to the low dielectric constant ($\epsilon<5$) of organic materials,[90] the strength of attraction between an electron and hole is strong (according to Coulomb's law); hence, they quickly recombine. In order to extract electrical energy, an exciton must be dissociated into free charges before electron-hole recombination. The exciton recombination time of organic semiconductors is on the order of picoseconds (ps) and

exciton diffusion length is 5–20 nm.[91] These types of bound electron-hole excitons are known as Frenkel excitons. This is sharply different from Wannier-Mott excitons observed in inorganics, where exciton dissociates into free charges upon excitation because of the high dielectric constant (ϵ~>12).[92]

To separate a bound electron-hole pair (exciton) into individual charges, additional energy is required to overcome the coulombic attraction. This energy can be provided either via an external electric field or, more commonly, by placing high electron affinity materials serving as an electron acceptor (as depicted in Figure 2.2). The LUMO offset between the donor and electron acceptor provides the necessary energy to dissociate ($E_{dissociation}$) an exciton.[93] Higher LUMO offset results in better exciton dissociation efficiency.

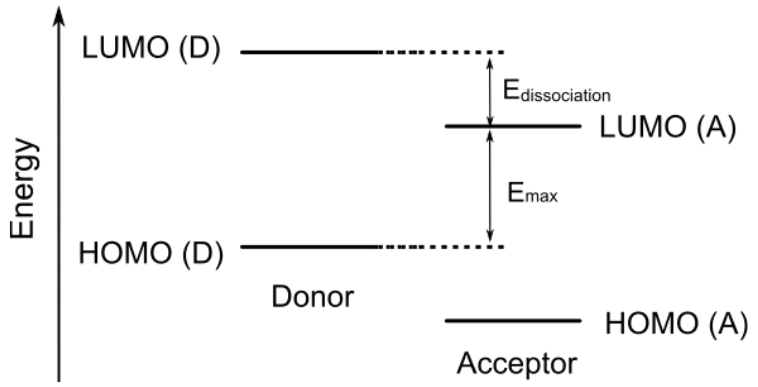

Figure 2.2 Schematic of band energy levels of semiconductor electron donor and acceptor. The LUMO offset ($E_{dissociation}$) indicates energy available for exciton dissociation into individual charges, whereas E_{max} indicates the maximum voltage that can be extracted from a given donor and acceptor combination. Device efficiency depends on the optimization of these two parameters.

For efficient dissociation, an exciton must reach the donor/acceptor interface from the point of generation. The exciton transport (also known as exciton diffusion or energy transfer) occurs either via Förster resonance energy transfer (FRET)[94, 95] or Dexter energy transfer (DET) mechanisms.[88] FRET is based on dipole-dipole interaction for electron exchange where the emission spectrum of the exciton donating and absorption spectrum of the exciton receiving molecules match (Figure 2.3). When this is satisfied, the donor molecules are energetically in resonance with receiving molecules, and exciton transfer occurs. FRET is dominant on the length scale of 1–10 nm range. On the other hand,

Dexter energy transfer signifies the direct exchange of electrons via an overlap of molecular orbitals and a dominant mechanism at a distance of <1 nm.

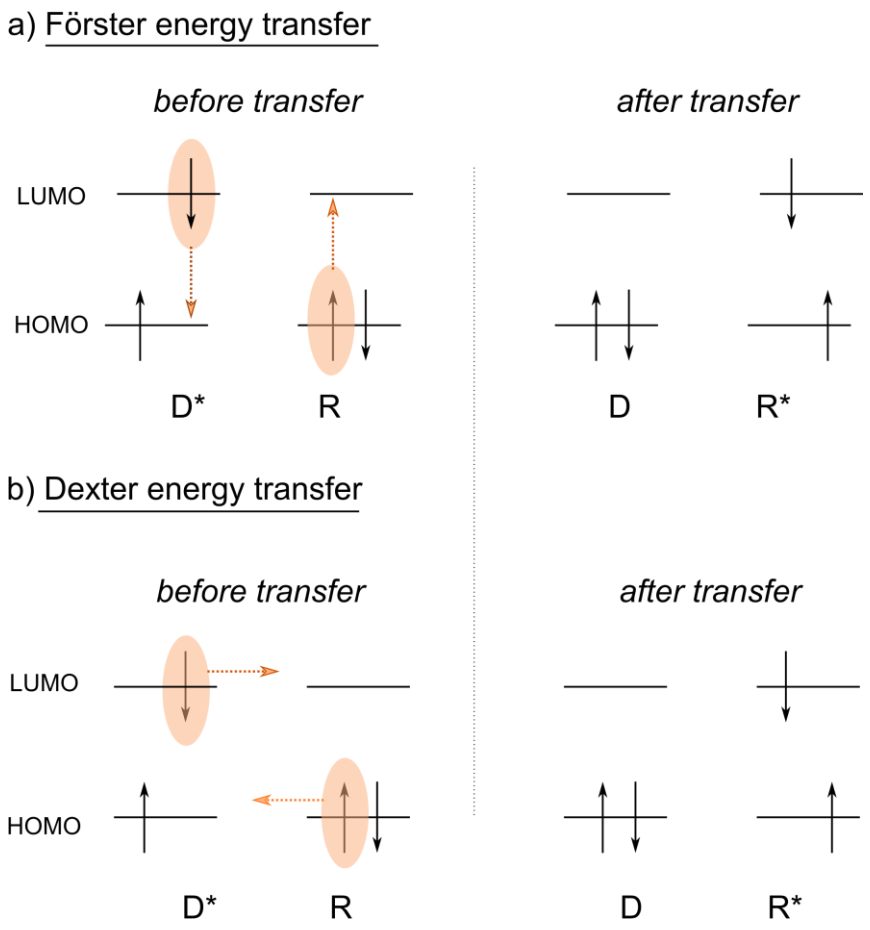

Figure 2.3 Schematic depicting a) Förster and b) Dexter energy transfer mechanisms between exciton donating (D) and receiving (R) molecules.

The bound electron-hole pair dissociates upon contact with an electron acceptor species having sufficient electron affinity, whereby the donor loses an electron.[96] As the diffusion length of an exciton in organic polymers is typically <20 nm,[76, 97, 98] excitons generated further than this distance from a donor/acceptor interface are likely to recombine before separating into charges. A larger donor/acceptor interfacial area incites efficient dissociation of excitonic charges and, consequently, results in a high photon-to-current conversion ratio. This is achieved by modifying the bilayer donor:acceptor interface (Figure 2.4a) to a 3D percolating network known as bulk-heterojunction (Figure 2.4b). After exciton dissociation, the resultant electronic charges can either be used to generate electrical current (organic photovoltaics) or drive a variety of redox reactions (organic

photoelectrochemical cells).[95] For this thesis, only the photoelectrochemical applications are considered. A more detailed report on the development of organic photovoltaics can be found elsewhere.[79, 99, 100]

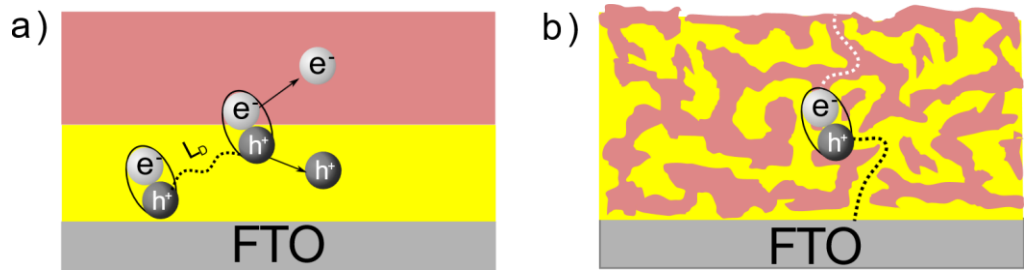

Figure 2.4 **Schematic depicting an exciton dissociation in (a) thin-film bilayer heterojunction electrode, and (b) thin-film bulk-heterojunction electrode in which donor and acceptor semiconductors are distributed in a three-dimensional continuous network.**

2.2.3. History

The discovery of conducting polymers and the ability to modify the conductivity of these materials via chemical syntheses have created immense interest.[101-104] Of the several available semiconducting polymers, polyanilines, polythiophenes, polyphenylenes, and polypyrroles have gained significant attention (Figure 2.5).[105] A brief introduction of the development of organic polymers for solar H_2 generation application is given below.

In 1985, Tang from Kodak Research Laboratories published a heterojunction-based organic solar cell formed between copper phthalocyanine (CuPc) and perylene tetracarboxylic derivative demonstrating considerable enhancement in photovoltaic efficiency over single-layer organic solar cells.[106] Following this, Sariciftci was the first to report a strong electron transfer effect from polymer polyl2-methoxy,5-(2'-ethyl-hexyloxy)-p-phenylene vinylene] (MEH-PPV) to fullerene (C_{60}) under illumination in 1992.[107] Fullerenes offer high electron affinity, near-degenerate LUMO, low-lying anion states, high electron mobility, and 3D–charge transport. This report included two crucial results that raised significant interest in organic solar cells: (i) electron transfer from polymer to fullerene and (ii) electron transfer in bulk-heterojunction '(composite)' form.

The same group then applied the donor:acceptor bulk-heterojunction concept to develop MEH:PPV-based solar cells.[108] To overcome the limited solubility of C_{60}, its

derivative PCBM was used as an acceptor. The resultant bi-continuous network of donor and acceptor showed a significant increase in energy conversion efficiency due to a large increase in interfacial area.[108] C_{60} is a direct bandgap semiconductor with a bandgap of 1.5 eV, and transition between bands is optically forbidden due to high molecular symmetry.[109] This results in a very low absorption coefficient of C_{60}.[94] However, higher fullerenes C_{70} and C_{84} have higher absorption coefficients than C_{60} due to symmetry breakdown. In the same year, Yoshino et al. achieved a higher donor:acceptor interface during BHJ film casting of C_{60} and poly(3-alkylthiophene) due to nanoscale phase separation.[110] Subsequently, Li et al. demonstrated an increased power conversion efficiency of 4.4% by controlling the active layer growth rate and annealing using ITO/PEDOT:PSS/P3HT:PCBM/Al organic solar cell, a record in 2005.[111] Since then, bulk-heterojunction has become standard device structure for organic semiconductor-based devices.

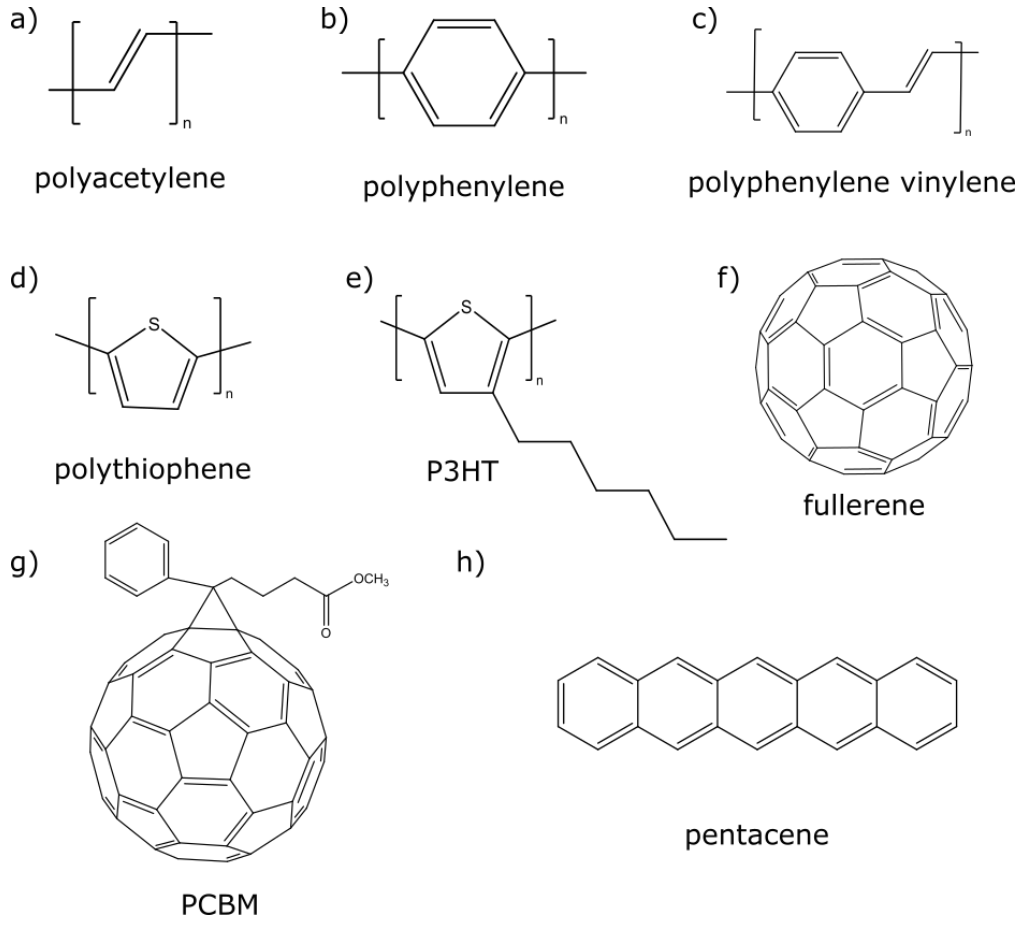

Figure 2.5 Chemical structures of select conjugated organic semiconductors.[112]

As the BHJ devices were gaining momentum in organic solar cells, El-Rashiedy and Holdcroft demonstrated the ability of P3HT to act as a photocathode for the hydrogen evolution reaction in photoelectrochemical cells.[113] The authors also observed a five-fold increase in photocurrent density of P3HT:C_{60} BHJ film over planar P3HT films. Despite these early positive results, organic photoelectrochemical cells remained dormant until Abe et al. published H_2 evolution from phthalocyanine/fullerene bilayer electrode.[114] This was followed by Lanzarini et al., who reported photoelectrochemical proton reduction on P3HT in the presence of an electron acceptor (phenyl-C61-butyric acid methyl ester, PCBM) in 2012. It was through these results that the topic gained renewed interest.[115] While the initial photocurrents reported for planar BHJ film are on the order of microamperes (μA), it is quickly overcome to reach milliampere (mA) level photocurrents by employing post-processing techniques (annealing) and additional layers (charge transport and catalyst).

2.2.4. Development of Organic Photoelectrodes

The development in OPEC devices can be classified into two broad categories: *(i) new material development* – such as new semiconductor synthesis and modification of bandgap, band energy levels, polymer solubility, and stability; and *(ii) device architecture optimization* – device optimization via nanostructuring, increased crystallinity, heterojunction layers such that maximum number of photons is harvested for a given donor:acceptor combination. For this thesis, only the device architecture development is considered, and new material development in organic semiconductors for photovoltaics and photoelectrochemical cells is reviewed elsewhere.[116-118]

The purpose of research on device architecture development is to efficiently convert generated excitons into charge carriers that can be utilized for the intended chemical reactions. This is achieved by increasing the efficiency of the charge generation, charge transport, and charge extraction processes.

(i) Charge generation: In a bilayer donor:acceptor device shown in Figure 2.4a, an exciton is generated when a photon with energy greater than the bandgap irradiates the polymer semiconductor. The generated exciton diffuses to a certain length (exciton diffusion length, L_D) and then recombines by releasing energy. Exciton that is generated within the exciton diffusion length from donor:acceptor interface is readily separated into

charges and then transported across the donor and acceptor phases towards the respective contacts. An exciton that is generated further than the exciton diffusion length from the donor:acceptor interface recombines, and its energy will be lost. Thus, to increase the exciton separation, the BHJ concept is used, which significantly increases the donor:acceptor interface. The BHJ phase separation and domain morphology must be optimized such that it will provide maximum exciton dissociation and not interfere with charge transport.[94, 119]

(ii) Charge transport: Charge transport is the limiting factor to photoelectrodes' performance after charge generation.[120, 121] It depends on the polymers' degree of conjugation, crystallinity, and carrier concentration. While the degree of conjugation and dopant concentration is controlled during semiconductor synthesis, the crystallinity of the film can be modified during film processing via thermal annealing. Increased crystallinity results in high carrier mobility as charges can easily move from one chain to an adjacent chain i.e., interchain transport. Annealing at a temperature of 120–150 °C for 10–30 min is typically reported to increase the performance of organic solar cells due to increased crystallinity, partial demixing of P3HT and PCBM phases, better film homogeneity and polymer domain interconnectivity.[122-125] These factors contribute to a significant increase in charge transport characteristics of annealed films.

(iii) Charge extraction: To increase the charge collection at the electrode/electrolyte interface, and at the electrode/back contact interface, charge transport layers such as hole transport (HTL) and electron transport (ETL) layers are employed. The charge transport layers selectively allow one type of charges to pass through, thus avoiding back migration of charges and consequently recombination.[126, 127] Some of the widely used charge transport layers are depicted in Figure 2.6. Furthermore, the transport layers also act as protective layers against the degradation of the materials.[76] On top of transport layers, electrocatalysts are deposited to increase the reaction kinetics.

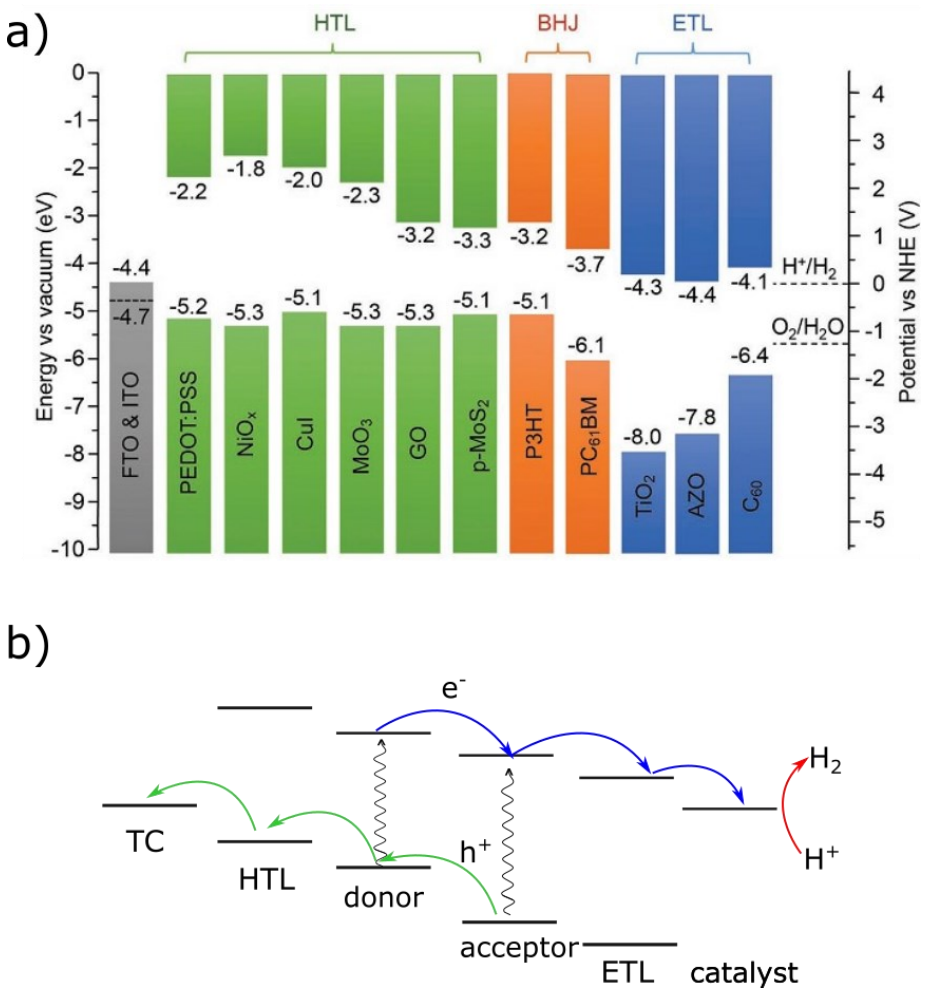

Figure 2.6 **(a). HOMO and LUMO energy levels of different hole (HTL) and electron (ETL) transport layers along with energy levels of P3HT and PCBM.[128] Reprinted with permission from Yao, L.; Rahmanudin, A.; Guijarro, N.; Sivula, K. *Adv. Energy Mater.* 2018, 8, 1802585. Copyright 2018 Wiley-VCH Verlag GmbH & Co. (b) Hole (h^+) and electron (e^-) charge transport pathways in an electrode having the device architecture of transparent conductor/hole transport layer/donor:acceptor BHJ/electron transport layer/catalyst.**

Hence, modern OPEC devices have advanced to a standard architecture of transparent conductor/ hole transport layer / donor:acceptor BHJ / electron transport layer / catalyst layer (TC/HTL/BHJ/ETL/Catalyst). By using this architecture, the current density obtained from OPEC cells has increased significantly. For example, Bourgeteau et al., reported an enhanced OPEC device performance by employing electron transport layer (PEDOT:PSS) and hole transport layer (LiF/Al) along with hydrogen evolution catalyst (MoS_3) forming the device architecture ITO/PEDOT:PSS/P3HT:PCBM/LiF:Al/Catalyst.[129] The electrode achieved a photocurrent density of 8 mA cm^{-2} at 0 V_{RHE} on par with

inorganic photoelectrodes. However, the stability was very low and lost 12% of the photocurrent in 10 min. Similarly several studies reported high photocurrents by employing P3HT:PCBM BHJ with different HTL (MoO_x,[130-133] WO3,[134] GO,[135] NiO,[130] CuI,[132, 136-138] PEDOT/PSS,[129, 139] WS_2,[140] CuO_x[141]), ETL (TiO_2,[132, 136, 137, 140] LiF/Al[129]), and HER catalysts (Pt,[132, 139] MoS_3,[129, 140, 142] RuOx[137]). These devices consistently delivered the photocurrents in the range of 5–8 mA cm^{-2}.

In addition to the traditional P3HT and PCBM based devices, other semiconducting polymers are also examined for PEC applications. Li et al., synthesized an electrode comprising PTB7 (poly[(4,8-bis-(2-ethylhexyloxy)-benzo(1,2-b:4,5-b′)dithiophene)-2,6-diyl-alt-(4-(2-ethylhexyl)-3-fluorothieno[3,4-b]thiophene-)-2-carboxylate-2-6-diyl]) donor and $PC_{61}BM$ acceptor along with CuO_x as HTL and TiO_x as ETL. The electrode delivered high photocurrent density (−7.23 mA cm^{-2}) and onset potential (0.6 V_{RHE}), and despite employing thin TiO_x (15 nm) protective film displayed poor stability and lost 75% of the photocurrents within one hour.[143]

Increased stability was achieved by Sivula et al., when the fullerene acceptors were replaced by non-fullerene perylene diimide based acceptors. Photocurrents up to 8 mA cm^{-2} were observed from the photoelectrode (ITO/MoO3/PTB7Th:PDI-V/RuO_2) along with impressive stability i.e., only 33% of photocurrents were lost in 20 hours. The stability of these electrodes can further be enhanced by employing a protective ETL layer.[144] Recently, photocurrents of more than 10 mA cm^{-2} and onset potential of 0.8 V were achieved from the photocathode FTO/CuO_x/PBDB-T:ITIC/TiO_x/Pt,* setting a record for OPEC devices.[141] In a short period of research, the performance of organic photoelectrodes increased considerably both in terms of photocurrent output (from sub-μA to ~10 mA) and stability (from <15 minutes to 10 hours) within a decade.[145, 146]

2.3. Inorganic-based Semiconductor Photoelectrodes

Inorganic semiconductors are ordered crystalline materials, where the atoms are covalently bonded with neighbouring atoms, and electrons are delocalized throughout the

* [**PBDB-T** (poly[(2,6-(4,8-bis(5-(2-ethylhexyl)thiophen-2-yl)-benzo[1,2-b:4,5-b′]dithiophene))-alt-(5,5-(1',3'-di-2-thienyl-5′,7′-bis(2-ethylhexyl)benzo[1′,2′-c:4′,5′-c′]dithiophene-4,8-dione))]).
ITIC (3,9-bis(2-methylene-(3-(1,1-dicyanomethylene)-indanone))-5,5,11,11-tetrakis(4-hexylphenyl)-dithieno[2,3-d:2′,3′-d′]-s-indaceno[1,2-b:5,6-b′]dithiophene)]

crystal. These electrons' allowed and forbidden energy levels form VB and CB levels (Figure 1.3).[45] The semiconducting behaviour is observed across different inorganic groups such as individual elements (e.g., Si, C, Ge), compounds (e.g., GaAs, CdS), and oxides (e.g., TiO_2, Cu_2O, Fe_2O_3). The origin of semiconducting behaviour is briefly explained in section 1.2.1. The VB and CB positions of select semiconductors used in PEC applications are depicted in Figure 2.7, along with theoretically expected photocurrent density from a particular bandgap.

Before proceeding further, it is important to recollect the applicability of photoelectrodes to a particular redox reaction is dependent on its semiconducting nature i.e., p-type semiconductors for HER and n-type semiconductors for OER. This is the result of the nature of charge distribution in the depletion region, as discussed in section 1.2.1. As the incident light generates electron and hole pairs in the depletion region, the electric field in the depletion region forces one type of charge towards the electrolyte and the other type towards the back contact of the semiconductor. For example, internal electric field set up in the depletion layer of the p-type semiconductor forces electrons towards the surface where it takes part in HER, and forces holes towards the back of the semiconductor. As the charge that needs to be transported to the back of the semiconductor is a hole and the semiconductor is of p-type, which typically has good hole mobility, p-type semiconductors are ideal for serving as photocathodes; similarly, n-type semiconductors are ideal for serving as photoanodes.

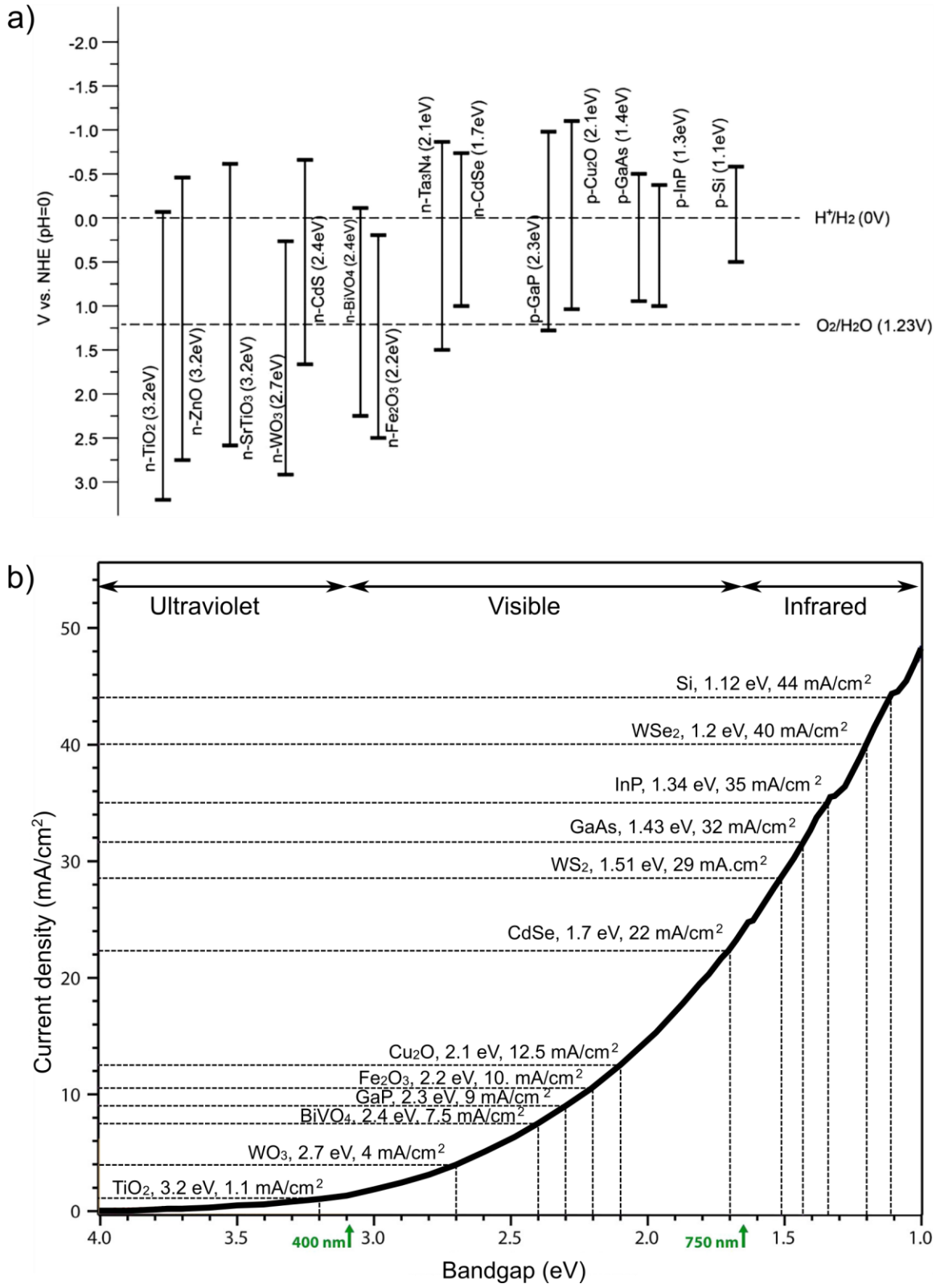
a)
V vs. NHE (pH=0)
-2.0
-1.5
-1.0
-0.5
0.0
0.5
1.0
1.5
2.0
2.5
3.0
n-TiO2 (3.2eV)
n-ZnO (3.2eV)
n-SrTiO3 (3.2eV)
n-WO3 (2.7eV)
n-CdS (2.4eV)
n-BiVO4 (2.4eV)
n-Fe2O3 (2.2eV)
n-Ta3N4 (2.1eV)
n-CdSe (1.7eV)
p-GaP (2.3eV)
p-Cu2O (2.1eV)
p-GaAs (1.4eV)
p-InP (1.3eV)
p-Si (1.1eV)
H+/H2 (0V)
O2/H2O (1.23V)
b)
Ultraviolet
Visible
Infrared
Si, 1.12 eV, 44 mA/cm2
WSe2, 1.2 eV, 40 mA/cm2
InP, 1.34 eV, 35 mA/cm 2
GaAs, 1.43 eV, 32 mA/cm2
WS2, 1.51 eV, 29 mA.cm2
CdSe, 1.7 eV, 22 mA/cm2
Cu2O, 2.1 eV, 12.5 mA/cm2
Fe2O3, 2.2 eV, 10. mA/cm2
GaP, 2.3 eV, 9 mA/cm2
BiVO4, 2.4 eV, 7.5 mA/cm2
WO3, 2.7 eV, 4 mA/cm2
TiO2, 3.2 eV, 1.1 mA/cm2
Current density (mA/cm2)
0
10
20
30
40
50
4.0
3.5
400 nm
3.0
2.5
2.0
750 nm
1.5
1.0
Bandgap (eV)

Figure 2.7 **(a) Valence and conduction band energy levels of semiconductors typically used in PEC applications along with water redox potentials.[46] Reprinted with permission from Jiang, C.; Moniz, S. J. A.; Wang, A.; Zhang, T.; Tang, J. *Chem. Soc. Rev.* 2017, 46, 4645. Copyright 2016 The Royal Society of Chemistry. (b) Plot depicting maximum theoretical photocurrent density that can be extracted from the given semiconductor bandgap.[147] Reprinted with permission from Liu, C.; Dasgupta, N. P.; Yang, P. *Chem. Mater.* 2013, 26, 415. Copyright 2013 American Chemical Society.**

2.3.1. Strategies to Increase Performance

While photoelectrodes consisting of a planar film of semiconductor (as depicted in Figure 2.4a) are relatively common, most of the highly efficient electrodes are comprised of semiconductors with one or more physical or chemical modifications such as nanostructuring, annealing, doping, and catalysts to boost the performance of the photoelectrodes. Hence a brief introduction to these techniques is given below, followed by the development of photoelectrodes:

Doping

Doping is a common strategy to enhance the optical and electronic properties of semiconductors. It is typically used to convert an intrinsic semiconductor to an extrinsic semiconductor (i.e., p-type or n-type), with Si being the classic example where phosphorus (P) or boron (B) doping is used to emulate n-type or p-type semiconducting behaviour, respectively. For PEC applications, doping is primarily carried out to achieve one or more of the following properties:

(i) *To increase electronic mobility* – Ta doping of Fe_2O_3 serves as an example to demonstrate the effect of electronic mobility on photoelectrodes' performance. Upon doping, each substitutional Fe^{3+} site gains two positive charges when replaced by Ta^{5+}, and two electrons are added to the lattice to maintain charge equilibrium. Thus, Ta-doped Fe_2O_3 exhibits significantly higher photoactivity than the non-doped electrode due to increased electron mobility.[148]

(ii) *To increase optical absorption* – Dopant atoms introduce additional energy levels in the bandgap, and at sufficient concentrations these energy levels form bands. When these energy bands occur near VB or CB energy levels reduction in bandgap occurs. Thus, by careful selection of Dopant atoms band energy levels

can be influenced. For example, by varying the concentration of In doping the bandgap of GaN can be tuned from 3.4 eV to 0.65 eV.[149] Dopant atoms such as C,[150] N,[151] S,[152, 153] and H[154] are widely used to increase the optical absorption of TiO_2 semiconductors, a wide bandgap semiconductor capable of only absorbing in UV wavelength. The combined effect of increased carrier density and change in electronic energy levels are often utilized to influence photoelectrode performance.[155]

Heterojunction

The expected functions of a photoelectrode—such as significant irradiant light absorption, efficient charge generation and transport, catalytic towards HER and OER redox reaction, and being stable in highly acidic or alkaline conditions—are challenging to be satisfied by a single semiconductor. Hence, more than one semiconductor is often combined in a heterojunction architecture to obtain satisfactory electrode performance. By having two semiconductors of different bandgap, complementary sections of the solar light can be absorbed, as depicted in Figure 2.8. However, care must be taken to avoid the impediment of charge flow between the semiconductors.

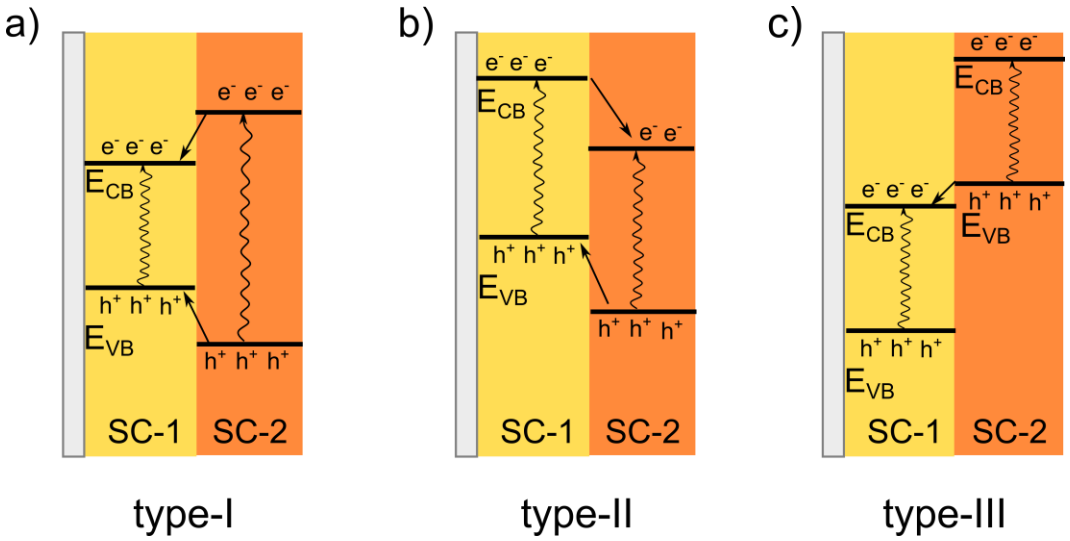

Figure 2.8 Schematic depicting types of heterojunctions based on the relative positions of band energy levels. Arrows indicate electron or hole transfer across the semiconductors.

Of the three different combinations imaginable, only the type-II configuration is suitable for photoelectrode applications owing to the cascade charge transfer. Heterojunctions are usually achieved by conformally locating a second semiconductor with

a suitable bandgap and position of band edges. The second electrode serves one or more of the following functions: to absorb the complementary wavelength of light,[156] to protect the underlying semiconductor by avoiding direct contact between photoelectrode and electrolyte, and to minimize recombination by efficient charge extraction.[157-159] Typical examples of heterojunction photoelectrodes are Cu_2O/TiO_2,[160] WO_3/TiO_2,[161] $BiVO_4/WO_3$.[162]

Nanostructures

Nanostructuring offers several advantages over planar electrodes, however, two main reasons are: *(a) To increase the electrode surface area* - the energy conversion efficiency of a photoelectrode is directly proportional to electrode/electrolyte interfacial area i.e., a larger interfacial area provides a higher number of reaction sites for the redox reactions. To increase the electrode/electrolyte interface, nanostructures such as nanoparticles, nanowires, and nanotubes are typically employed (Figure 2.9). *(b) To increase charge collection* efficiency - In planar electrodes, excitons generated further than the one diffusion length from depletion layer width will not contribute to redox reaction.[163] This is a typical loss mechanism in materials with high optical absorption length but low exciton diffusion length, i.e., the excited charges generated deep in the photoelectrode recombine before reaching the electrode/electrolyte interface.[164] By employing two-dimensional nanostructures such as nanowires or nanorods that depict the feature size as carrier diffusion length, a maximum number of charges can be captured.[165-167]

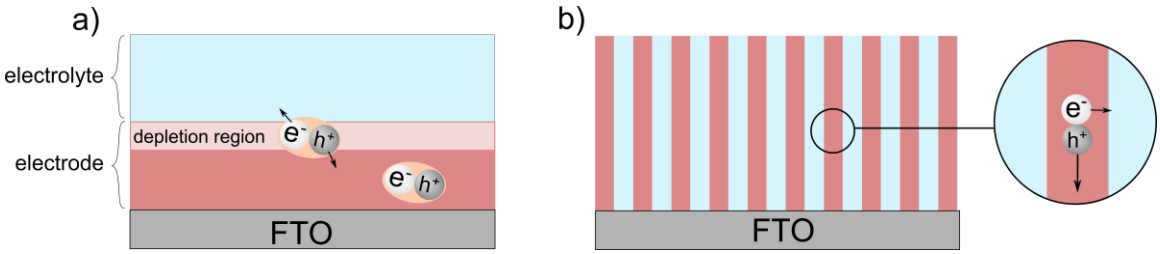

Figure 2.9 Schematic depicting charge generation in depletion layer in (a) planar and (b) nanostructured photoelectrodes.

Electrocatalyst

Catalysts improve reaction kinetics by reducing the overpotential required for HER and OER reactions. Besides providing active sites for redox reactions, catalysts increase photoelectrode's performance by removing energetic carriers from the semiconductor,

thus preventing electron-hole recombination. The performance of a particular catalyst is evaluated by the overpotential required to reach a current density of 10 mA cm^{-2}.[168] The catalysts CoO_x, Co-Pi, Ni-Fe oxides, IrO_2, RuO_2, NiO_x for oxygen evolution and Pt, RuO_x, MoS_2, NiMo alloy, CoP for hydrogen evolution reactions are commonly used.[24, 169-172]

In addition to the stratagems mentioned above, techniques such as surface passivation,[173] increased crystallinity,[122, 123] crystal plane orientation,[174, 175] and defect engineering[176] are also often employed to increase the performance of a photoelectrode. Some of the widely studied inorganic semiconductor-based photoelectrodes are discussed in the upcoming sections.

2.3.2. Development of Inorganic Photoelectrodes

Oxide-based Semiconductors

Among semiconductors, oxides display exciting characteristics such as ease of synthesis, earth abundance, and low cost. The TiO_2 (3.2 eV, n-type) semiconductor is the most widely studied semiconductor for solar hydrogen generation applications owing to its excellent chemical stability, non-toxicity, earth-abundant and band edges straddle water redox potentials.[71] However, due to its large bandgap nature, TiO_2 is capable of absorbing only the UV wavelengths and not the visible or infrared wavelengths, which constitute a significant portion of solar irradiation. Hence, despite attractive physical properties, the solar to hydrogen conversion efficiency of TiO_2 is very low for practical applications. For the same reason, ZnO (3.3 eV, n-type),[177] NiO (3.6 eV, p-type)[178] oxides having a similar bandgap as TiO_2 were also deemed unsuitable as photoelectrodes. Efforts to increase the efficiency of photoelectrodes through various techniques such as thermal annealing, nanostructuring, and doping did not yield sufficient enhancement. However, these oxides play a crucial role in protecting other unstable semiconductors when conformally coated on the surface of other semiconductors in a heterojunction design, on account of their excellent chemical stability and visible light transparency.[137]

Besides TiO_2, oxide semiconductors possessing lower bandgap such as Fe_2O_3 (n-type, 2.2 eV),[69, 179] WO_3 (n-type, 2.7 eV),[180, 181] $BiVO_4$ (n-type, 2.4 eV),[182, 183] CuO (p-type, 1.5 eV),[184-186] and Cu_2O (p-type, 2.1 eV)[187] have attracted significant research interest. They are not only capable of absorbing a significant portion of the visible light, but are also earth-abundant, and possess suitable band edge positions that straddles either HER or

OER, thereby being capable of serving as photocathode or photoanode, respectively. Though these materials displayed a significant increase in performance over large-gap semiconductors, the observed STH efficiency is much less than the theoretically predicted values (shown in Figure 2.7). These lower values are typically attributed to one or more of the following: (i) short charge carrier diffusion length, (ii) fast electron-hole recombination (~ps), (iii) poor catalytic activity, (iv) low carrier mobility, and (v) poor stability.[188, 189] Hence, research in oxide semiconductors is mostly devoted to addressing these issues by employing nanostructures, dopants, heterojunction design, and electrocatalysts.[190, 191] By incorporating these techniques, the Grätzel group was able to achieve a photocurrent density of 10 mA cm^{-2} from a nanostructured Cu_2O photoelectrode having the architecture of FTO/Cu_2O/Ga_2O_3/TiO_2/RuO_x (Figure 2.10)[192-195] compared to the 2 mA cm^{-2} that is typically observed for planar Cu_2O films.[196] Furthermore, the photocurrents remained stable for over 100 hours making it one of the leading candidates for inorganic photocathodes.

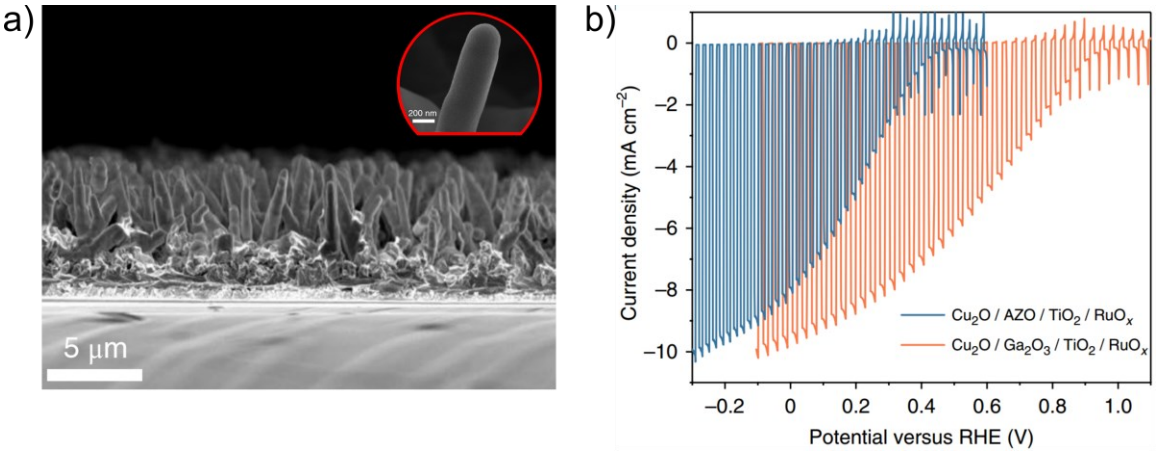

Figure 2.10 (a) SEM micrograph of vertically grown Cu_2O nanowires, and (b) the chopped light LSV of corresponding nanowire-based photoelectrodes.[197] Reprinted with permission from Pan, L.; Kim, J. H.; Mayer, M. T.; Son, M.-K.; Ummadisingu, A.; Lee, J. S.; Hagfeldt, A.; Luo, J.; Grätzel, M. *Nat. Catal.* 2018, 1, 412. Copyright 2018 Macmillan Publishers Limited.

Non-oxide-based Semiconductors

While the performance of oxide semiconductors has considerably improved over the last decade, non-oxide inorganic semiconductor research is populated with materials borrowed from photovoltaics. Semiconductors belonging to group IV (Si),[198] group III-V (GaAs, GaInP InP),[199, 200] group II-VI (CdS, CdTe, Cu(In, Ga)$(S,Se)_2$,

$Cu_2ZnSn(S,Se)_4$[201, 202] occupy a significant portion as these materials possess optimum bandgap for solar light absorption and suitably placed band edge positions relative to water redox potentials. Although photovoltaic efficiency of >20% and current densities up to 30 mA cm^{-2} have been reported for multijunction devices consisting of the above-mentioned semiconductors, translating the similar performance to PEC application has been challenging.[203, 204] For instance Lewrence et al., reported an STH efficiency of 19% using RuO_2−GaAs/GaInAs/GaInP/AlInP−TiO_2−Rh photoelectrode which achieved 85% of theoretically predicted values for the chosen semiconductors.[205] Furthermore, several authors have reported achieving STH efficiencies of up to 20% using perovskite-Si based devices, a current record.[206-208] While it is enticing to think about having a p-n junction encapsulated in protective materials and catalysts (known as buried p-n junction), high-cost requirements and poor stability of these semiconductors hinder their widespread adaptation. However, as these systems achieve high STH efficiency compared to the PEC devices which currently achieve only <5% STH efficiency,[72, 209] PV-based systems serve as a benchmark for PEC electrode development.

(note: Before proceeding further, an important distinction must be made regarding the working principle of these materials. In photovoltaic research, the solar cells derive potential from the depletion layer formation at the p-n junction, while in typical PEC research, photopotential is generated due to the depletion region formation at the electrode/electrolyte interface. A more detailed discussion is beyond the scope of this thesis and can be found in the literature.[54, 200, 210])

Photoelectrodes made of semiconductors such as Si, CdS, and GaP display good photocurrents but are unstable in the PEC operating environment. However, protection of these electrodes is achieved by conformally depositing transparent, protective films such as TiO_2 or NiO via atomic-layer deposition (ALD), which is a promising but prohibitively expensive method for practical applications.[11, 46, 165, 211] For instance, Si combined with appropriate protective and catalyst layer can produce hydrogen but exhibits poor long-term stability.[212] The current inorganic research for PEC application is focused on (a) testing novel photoelectrode materials (e.g., Sb_2Se_3, $BiVO_4$, $CuBiO_4$ etc.) to achieve increased efficiency, (b) finding low-cost protective layers as an alternative to ALD,[213, 214] and (c) developing earth-abundant co-catalysts.[155]

2.4. Thesis Scope

One of the main criteria for PEC H_2 generation put forth by the U.S Department of Energy is to achieve high solar-to-hydrogen (STH) conversion efficiency at a low cost (section 2.1). Several inorganic and organic semiconductors, including Fe_2O_3,[215] CuO,[184, 216] Cu_2O,[217, 218] $BiVO_4$,[219] CdS,[217] GaInP,[49, 220] P3HT:PCBM and PBDB-T:ITIC have been widely explored as photoelectrodes for water splitting.[46, 92, 221-223] However, observed trends in the literature suggest that high-cost materials (Ga, In, Pt, Rd, Au, etc.) and expensive coating techniques such as atomic layer deposition and physical vapour deposition are required to fabricate electrodes that yield high STH efficiency.[224, 225] The maximum reported STH efficiency of the majority of the low-cost electrodes is almost an order lower than the theoretically predicted values, suggesting that there is considerable room for improvement.[225-228] However, to date, no single semiconductor satisfactorily meeting all the DOE requirements has been discovered or synthesized.[229] One of the main reasons for a PEC device to not achieve theoretically expected efficiency is energy losses. The losses can broadly be classified as losses associated with a photoactive component of the device (donor, acceptor, D/A interface)[120] and non-photoactive components of the device (poor charge collection, recombination due to poor catalytic activity). As seen in the previous section, the synthesis and application of charge transport and catalytic layers are mostly optimized. Hence to improve the efficiency, BHJ efficiency needs to be improved.

A BHJ film is generally prepared by depositing a solution containing a mixture of donor and acceptor molecules on an electrode, followed by solvent evaporation. During film formation, as the solvent evaporates, one of the two molecules becomes insoluble before the other. This causes phase separation and results in a bi-continuous network of donor and acceptor molecules throughout the film. However, the phase separation is not constant across different donor-acceptor combinations and largely depends on miscibility, molecular weight, concentration, deposition temperature, method of deposition, and any physical or chemical interaction with each other and the substrate.[120, 230] Hence it is difficult to obtain consistent device performance for the given donor:acceptor combination owing to the lack of control over the domain size of phases. To overcome this, nanoparticle-based electrode architecture is proposed wherein the domain sizes of the donor and acceptor phases can be fixed during the nanoparticle synthesis.[79]

2.4.1. Hypothesis

BHJ electrodes are classified as (i) thin-film BHJ - a planar film of finely distributed donor and acceptor phases (as depicted in Figure 2.4b) or (ii) nanoparticle BHJ - a planar film containing nanoparticles of donor and acceptor phases (as depicted in Figure 2.11) based on the distribution and morphology of donor and acceptor phases. Thin-film-based donor:acceptor BHJ architecture is a commonly used technique to increase the photoconversion efficiency of organic photoelectrodes by increasing the interfacial area of the donor/acceptor domains. To achieve this, donor and acceptor materials are dissolved in a suitable (usually halogenated) solvent and cast onto a substrate. During film formation, the solvent evaporates, and the donor and acceptor components segregate into separate domains[231-233] producing an interpenetrating nanoscale donor/acceptor blend throughout the film, thereby increasing the interfacial area.[111, 234, 235]

On the other hand, nanoparticle-based BHJ architecture aims to increase device efficiency by combining the beneficial effect of heterojunction and nanostructures. It also offers a way to exercise control over phase segregation in large volume applications because the domain size of segregation is dictated by the size of the nanoparticles.[232, 236-239] A BHJ device employing nanoparticles can be classified as (i) core-shell structured or (ii) blended or (iii) Janus-type, or (iv) randomly distributed NPs based on the distribution of donor and acceptor materials (Figure 2.11).

In a core-shell-based BHJ architecture, the donor and acceptor species are present in a molecularly controlled manner, i.e., each nanoparticle contains a donor phase surrounded by an acceptor phase or vice versa. (Figure 2.11a). Efficient exciton dissociation occurs at the donor:acceptor interface within the nanoparticle. However, the generated electrons or holes cannot be efficiently transported across a large number of nanoparticles towards the electrolyte or electrode contact, as a continuous charge transport pathway for the generated charged species does not exist. For instance, in a photoelectrode comprising nanoparticles of core(p-type, donor)-shell(n-type, acceptor) structure only electrons can be efficiently transported by the shell (acceptor) across a large number of nanoparticles, whereas holes are trapped within the NP's core.[240] This promotes electron-hole recombination and results in decreased photoconversion efficiency.

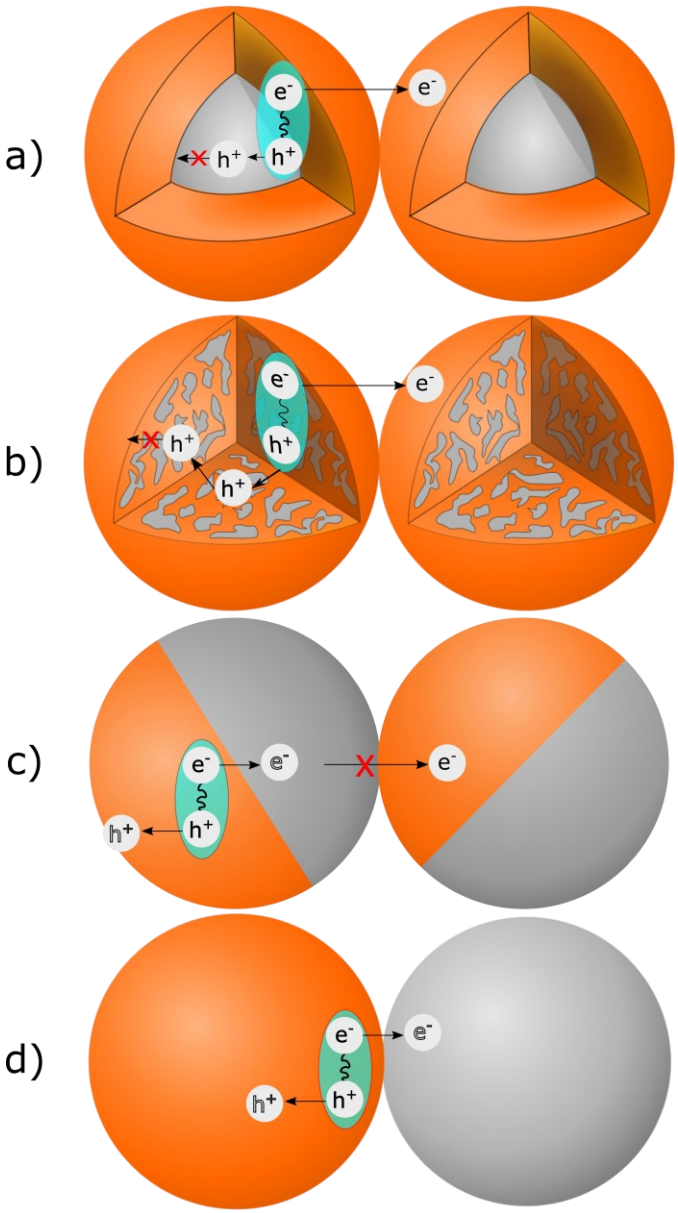

Figure 2.11 Schematic of different types of bulk-heterojunction nanoparticles, namely, (a) core-shell, (b) blended, (c) Janus-type, and (d) randomly-distributed structures based on the arrangement of donor and acceptor phases (D-Donor, A-Acceptor).

The blended architecture consists of nanoparticles comprising a thorough blend of donor and acceptor species, as depicted in Figure 2.11b. As different materials possess different surface energy during nanoparticle formation, the material with lower surface energy will predominantly occupy the surface. Hence this structure resembles a core-shell structure with a BHJ core and low-surface energy material largely occupying the surface.[240] Even negating this core-shell effect, charge transport between adjacent

nanoparticles is cumbersome due to the lack of a continuous charge transportation path.[122] Despite this, studies have shown that blended nanoparticle-based BHJ electrodes perform better than core-shell electrodes because of the charge trapping in the latter.

Unlike core-shell and blended nanoparticle-based electrode architecture, a continuous charge transport path may exist in Janus (Figure 2.11c) and randomly distributed configurations (Figure 2.11d) of donor-acceptor NPs. In both configurations, the existence of a continuous pathway for charge carrier transport cannot be externally controlled and is dependent on particle distribution. Hence these serve as templates to explore nanoparticle-based BHJ devices. However, owing to the difficulties in synthesizing significant quantities of Janus-type nanoparticles, this thesis explores the photoelectrochemical behaviour of randomly distributed BHJ electrodes which is rarely examined for photoelectrochemical H_2 generation application.

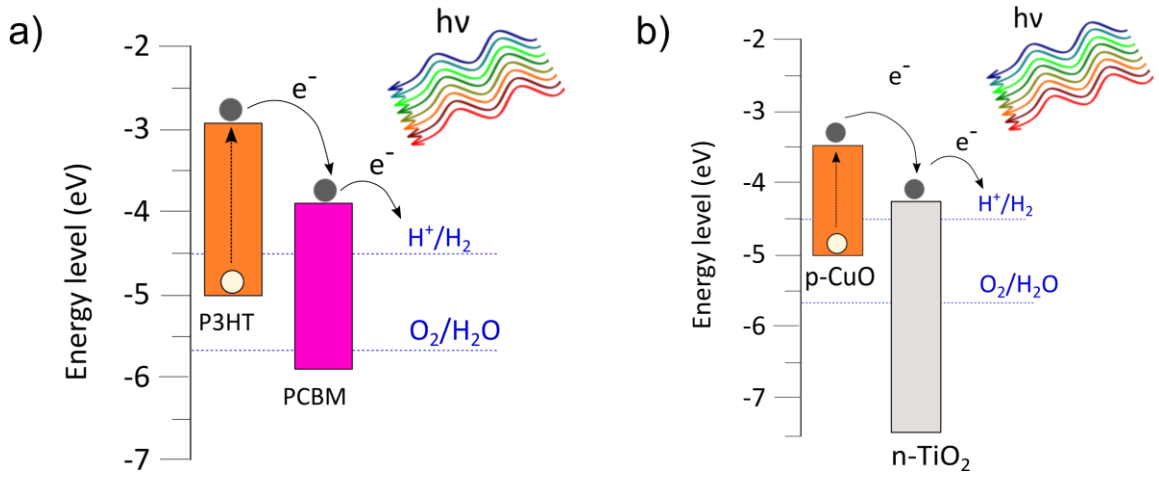

Figure 2.12 Charge carrier flow direction upon illumination depicted over energy level diagram of a) organic semiconductors poly(3-hexylthiophene) (P3HT) and phenyl-C61-butyric acid methyl ester (PCBM), and b) inorganic semiconductors cupric oxide (CuO) and titanium dioxideTiO_2 (note: potential values are represented for pH 0).

Towards this goal, organic semiconductors P3HT (p-type) and PCBM (n-type), and inorganic semiconductors CuO (p-type) and TiO_2 (n-type) have been selected where p-type semiconductors act as electron donors and n-type semiconductors act as electron acceptors (as depicted in Figure 2.12). The rationale behind the choice of semiconductors and the methods to prepare disordered, phase-separated nanoparticle BHJ electrodes are discussed in the upcoming chapters.

Chapter 3.

Photocathodic Hydrogen Evolution from Catalyzed Nanoparticle Films Prepared from Stable Aqueous Dispersions of P3HT and PCBM

Sections of this chapter have been reproduced in part with permission from Fortin, P. J.; Rajasekar, S.; Chowdhury, P.; Holdcroft, S. *Can. J. Chem.* **2018**, 96, 148. Copyright 2018, NRC Research Press, and from Rajasekar, S.; Fortin, P. J.; Tiwari, V.; Srivastva, U.; Sharma, A.; Holdcroft, S. *Synth. Met.* **2019**, 247, 10. Copyright 2018, Elsevier B.V. Only the contributions made to the papers by S. Rajasekar are presented in this chapter.

3.1. Introduction

Poly(3-hexylthiophene) (P3HT) is a hexyl-substituted derivative of conjugated polythiophene - a quintessential polymer whose optoelectronic properties have been well studied and relatively understood; it serves as a model system to explore the photoelectrochemical properties of proposed randomly distributed nanoparticle-based BHJ research.[96] The hexyl side chain increases the solubility of the polythiophene and influences the structural, optical, and electronic properties of the polymer.

Owing to the asymmetry of the 3-hexylthiophene when monomers are coupled, based on the relative position of the sidechain, three different coupling configurations can be imagined i.e., head-to-tail (H-T), head-to-head (H-H), and tail-to-tail (T-T). A polymer chain that contains only H-T configurations is denoted as regioregular and that contains a mix of coupling configurations as regiorandom (Figure 3.1). Regioregular polymers are widely used for photoelectrochemical applications as these are shown to produce polymer films with a high degree of structural order that results in higher carrier mobilities which often translates to higher device efficiency.[234]

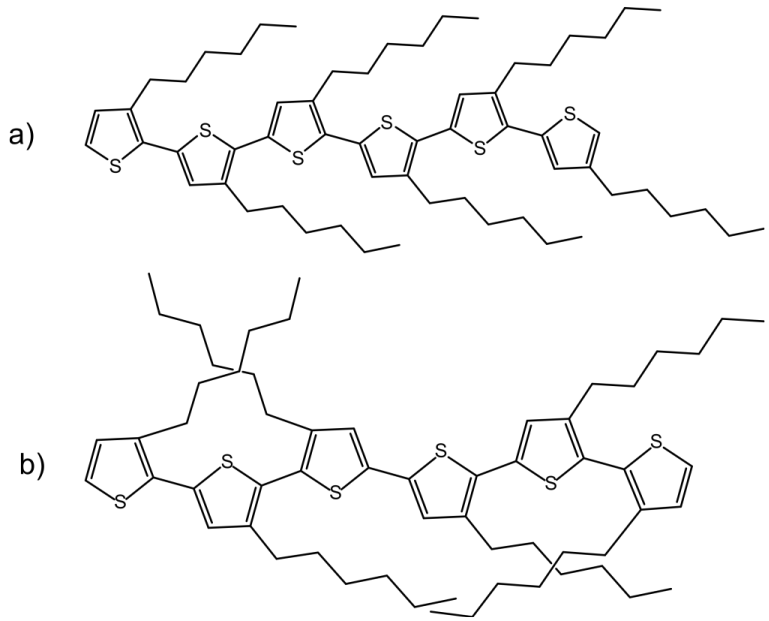

Figure 3.1 Schematic representation of poly(3-hexylthiophene) chain with (a) regioregular and (b) regiorandom structure.

P3HT has a bandgap of ~2 eV with a conduction band edge more negative than the standard electrochemical potential of H^+/H_2, as shown in Figure 2.12. It has a high optical absorption coefficient but a low exciton diffusion length, leading to exciton recombination. To overcome this, a PCBM electron acceptor in a BHJ form is typically used as described in section 2.2.1. The sequence of events leading to hydrogen evolution[241] in this system is shown in Figure 2.12a for the case where PCBM serves as the electron acceptor and Pt electrocatalyzes the hydrogen evolution reaction.

Two widely used methods to synthesize organic polymer nanoparticles are (i) precipitation and (ii) miniemulsion.[242, 243] In the precipitation method, polymer nanoparticles are formed by dissolving the polymer in a suitable solvent, usually a halogenated organic solvent, and adding this to a poor solvent, typically alcohol-based, to collapse the polymer chains, thereby forming nanoparticles.[122, 244] A schematic of this method for the case of P3HT and PCBM is shown in Figure 3.2. Each nanoparticle consists of a thoroughly mixed blend of donor and acceptor, np(P3HT:PCBM). Though this method produces nanoparticles in a few simple steps, the nanoparticles often coalesce over a short period, leading to precipitation and loss of usable dispersed material.[245] Moreover, halogenated organic solvents, used in the initial preparation step pose potential health and environmental risks for large-scale industrial applications.[243, 246]

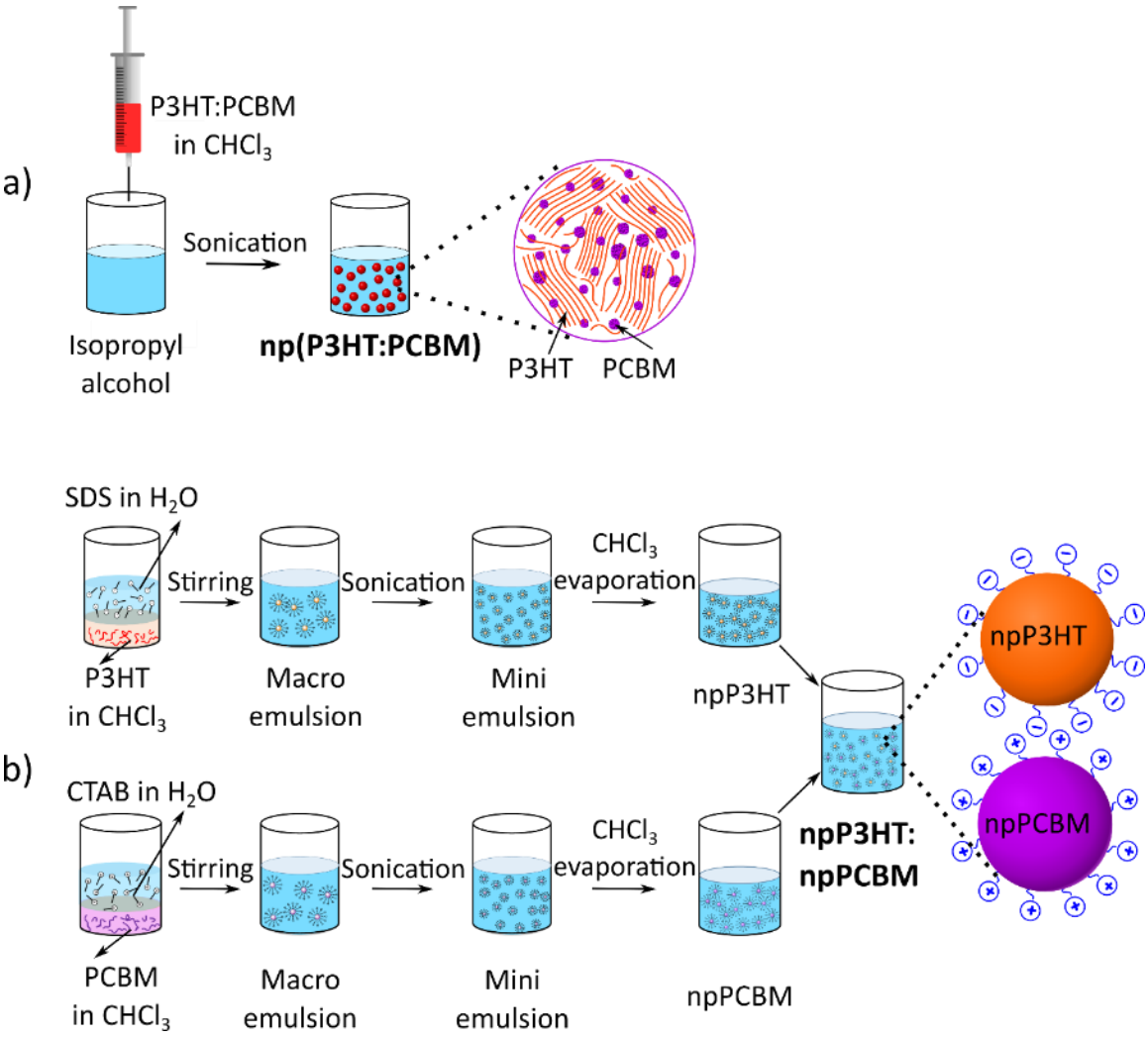

Figure 3.2 **Schematic representation of (a) synthesis of np(P3HT:PCBM) nanoparticle dispersion via precipitation method, formed by adding P3HT and PCBM dissolved in a good solvent to a poor solvent.[244] (b) Synthesis of npP3HT:npPCBM nanoparticles via the miniemulsion method. P3HT nanoparticles are prepared with an anionic surfactant, SDS, and PCBM nanoparticles are prepared with a cationic surfactant, CTAB, prior to their combination to form an aqueous-based dispersion.**

In the miniemulsion method, NPs can be prepared in an aqueous solution.[247, 248] The polymer is dissolved in a suitable solvent (which is immiscible with water) and subsequently added to water containing a surfactant to create an oil-in-water system. By applying a high shear force to the mixture, nanodroplets of polymer solution are formed, stabilized by surfactant. By allowing evaporation of the organic solvent, a surfactant-stabilized, water-based dispersion of polymer nanoparticles is produced, as illustrated in Figure 3.2. The advantage of the miniemulsion method over the precipitation method is

that it produces stable, water-based nanoparticle dispersions. The evaporated halogenated solvents may be captured and recycled.[232, 248-252]

P3HT:PCBM nanoparticles synthesized by the conventional miniemulsion method, where both P3HT and PCBM are initially dissolved together, have been shown to possess a core-shell morphology, with a PCBM rich core, due to P3HT having a lower surface energy of 26.9 mJ/m^2 than PCBM (38.2 mJ/m^2). Hence PCBM predominantly occupies the core of the nanoparticle while P3HT dominates the shell.[237, 242, 243, 253] An X-ray microscope image of a nanoparticle prepared via the miniemulsion method depicting core-shell structure is shown in Figure 3.3. The core-shell structure limits both the generation of charges from photogenerated excitons and the transportation of electronic charges across the electrode.[232] For this reason, and due to the presence of passive surfactants, which may impede charge transfer between nanoparticles, the OPV performances of active layers prepared in this manner are reported to be lower than nanoparticles prepared by the precipitation method.[82, 237, 242, 243, 254, 255]

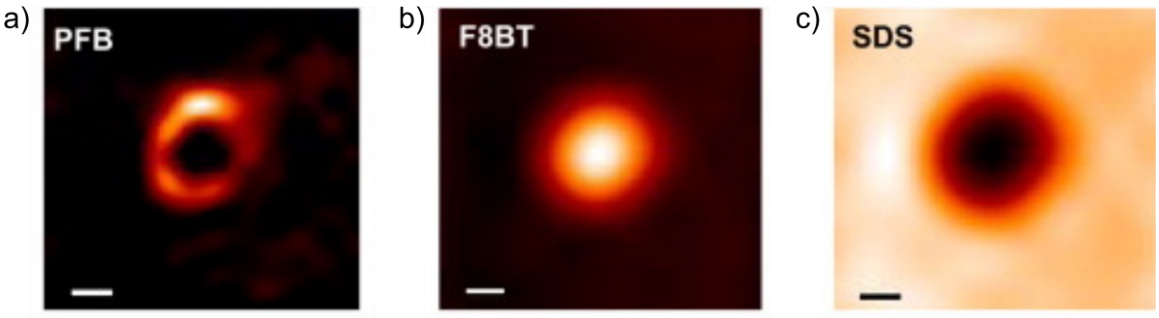

Figure 3.3 **Scanning transmission X-ray microscope image of PFB:F8BT donor:acceptor nanoparticle prepared via miniemulsion method using SDS surfactant depicting core-shell nanostructure. (PFB – poly(9,9-dioctylfluorene-co-N,N-bis(4-butylphenyl)-N,Ndiphenyl-1,4-phenylenediamine); F8BT – poly(9,9-dioctylfluorene-co-benzothiadiazole; scale bar – 50 nm).[254] Reprinted with permission from Stapleton, A.; Vaughan, B.; Xue, B.; Sesa, E.; Burke, K.; Zhou, X.; Bryant, G.; Werzer, O.; Nelson, A.; David Kilcoyne, A. L.; Thomsen, L.; Wanless, E.; Belcher, W.; Dastoor, P. *Sol. Energy Mater. Sol. Cells* 2012, *102*, 114. Copyright 2012 Elsevier B.V.**

In this chapter, a method to prepare photoactive films for PEC hydrogen evolution utilizing stable, chloroform-free, water-based nanoparticle dispersions that avoid the core-shell morphology through the independent formation of P3HT (npP3HT) and PCBM (npPCBM) nanoparticles is presented. The two independently prepared nanoparticle solutions were combined to prepare the final npP3HT:npPCBM dispersions and then

deposited onto a transparent conducting substrate. Ultra-low loadings of Pt catalyst were subsequently deposited by photoelectrochemical deposition to produce photocathodes capable of evolving H_2 without the need for additional multilayer deposition processes. This study reports the properties of npP3HT:npPCBM films and compares them to analogous films of np(P3HT:PCBM) prepared by the precipitation method. For comparison, the photoelectrochemical performance of nanoparticle BHJ is shown with that of analogous planar BHJ. A more detailed comparative study of planar and nanoparticle BHJ (np(P3HT:PCBM)) can be found in the research literature.[244]

3.2. Materials and Experimental Methods

Regioregular poly(3-hexylthiophene) (RR-P3HT, 91–94%) and 6,6-phenyl-C61-butyric acid methyl ester (PCBM) (> 99.5%) were purchased from Rieke Metals Inc. and American Dye Source Inc., respectively. Potassium hexachloroplatinate (K_2PtCl_6) was procured from Johnson and Matthey Inc. HPLC-grade chloroform ($CHCl_3$, ≥99.9%), sodium dodecyl sulfate (SDS, 70%), and cetyltrimethyl ammonium bromide (CTAB, 95%) were obtained from Sigma-Aldrich. Indium tin oxide (ITO) coated glass was purchased from Colorado Concept Coatings LLC. All reagents were of analytical grade and used without further purification. Aqueous solutions were prepared from deionized (DI) water purified using a Milli-Q water purification system (18 MΩ, EMD Millipore).

3.2.1. Miniemulsion Nanoparticle Synthesis

P3HT and PCBM nanoparticles were prepared by the miniemulsion method using SDS and CTAB surfactants, respectively, as follows (illustrated in Figure 3.2b). P3HT (10 mg) was dissolved in 1 mL $CHCl_3$ and stirred overnight at 55 °C (solution **A**). SDS (2 mg) was dissolved in 1 mL distilled water (solution **B**) to form a solution at critical micelle concentration (CMC). Solution B was added to solution A and stirred at 1000 rpm for 60 minutes at room temperature (RT) to form a macroemulsion, which was transferred to an ultrasonic bath and sonicated (Branson 1510 ultrasonic cleaner) for 30 minutes at RT to form a miniemulsion as indicated by the colour change of the emulsion from bright orange to dark green. The miniemulsion was stirred at 61 °C for 15 minutes to remove $CHCl_3$, and the resulting nanoparticle dispersion was filtered and stored (note, the emulsion is termed as “dispersion” upon evaporation of the organic solvent). PCBM

nanoparticles (npPCBM) were synthesized in an analogous manner, except a cationic surfactant (CTAB (0.3 mg)) was used at its CMC. The npPCBM dispersion was added dropwise to the npP3HT dispersion while the latter was immersed in an ultrasonic bath (Branson 1510 ultrasonic cleaner) and finally filtered through a cotton-tipped glass pipette to yield a water-based dispersion of npP3HT:npPCBM.

3.2.2. Precipitation Nanoparticle Synthesis

Dispersions of P3HT:PCBM nanoparticles i.e., P3HT and PCBM blended within each nanoparticle, were prepared by the precipitation method as illustrated in Figure 3.2a by dissolving 10 mg of P3HT and 10 mg of PCBM separately, each in 1 mL of $CHCl_3$, stirring overnight at 55 °C. The solutions were mixed, and 1.5 mL of the mixture was added by syringe to 4 mL of isopropyl alcohol (IPA) under sonication at room temperature for 1 minute (Branson 1510 ultrasonic cleaner). The obtained dispersion of np(P3HT:PCBM) was filtered through a cotton-tipped glass transfer pipette before spin coating and used within 24 hours.

3.2.3. Thin-film Synthesis

P3HT:PCBM bulk-heterojunction thin-film electrodes were prepared by mixing 10 mg of P3HT and 10 mg of PCBM separately, each in 1 mL of $CHCl_3$, stirring overnight at 55 °C. The solutions were mixed and filtered through a 0.45 μm PTFE filter before spin-coating onto a clean indium tin oxide (ITO) based transparent conducting substrate. Since ITO possesses a very large bandgap in the range of 3.5–4.3 eV, it is transparent to 85–90% of the visible light spectrum. Hence, it generates negligible photocurrent under illumination making it an ideal candidate to study photoelectrodes.[256, 257]

3.2.4. Fabrication of Photoelectrodes

ITO coated glass slides were cleaned sequentially under sonication for 10 minutes in soapy water, DI water, ethanol, and IPA, followed by O_2 plasma treatment (Fischione Instruments model 1020 plasma cleaner) using 25% O_2 in Ar for 10 minutes. The P3HT:PCBM nanoparticle dispersion was spin-coated (100 μl/cycle) onto 2 cm × 1 cm ITO slides at 2000 rpm for 60 s. A film thickness of ~200 nm was achieved with ten spin-coating cycles.

Pt catalyst was photoelectrochemically deposited on top of polymer nanoparticle films by applying a cathodic potential of −0.1 V_{SCE} to the electrode under chopped light illumination (100 mW cm^{-1}) in 0.1 mM K_2PtCl_6/1M H_2SO_4. Sulfuric acid (H_2SO_4) was added to increase the ionic conductivity of the electrolyte. At the applied cathodic potential $PtCl_6^{2-}$ anion undergoes reduction according to Equation 3.1 as its redox potential (0.744 V_{SHE}) lies substantially below the CB of P3HT and PCBM. The mass of platinum deposited was calculated from the charge passed during electrodeposition.[258] In this work, 1 μg cm^{-2} of Pt was deposited on the nanoparticle films. At this low of a Pt loading, the Pt is deposited as nanoparticles, as demonstrated later in this report.

$$PtCl_6^{2-} + 4e^- \longrightarrow Pt + 6Cl^- \quad (E_{Pt^{4+}/Pt} = 0.744\ V_{SHE}) \tag{3.1}$$

3.2.5. Characterization of Electrodes

The particle size distribution of the nanoparticles was measured by dynamic light scattering (DLS) using a NanoSeries Nano-ZS (Malvern Instruments, UK) equipped with a helium-neon laser source (Power = 4.0 W: λ = 633 nm). Dispersions of nanoparticles were diluted in water to avoid multiple light scattering. Typically, 10 μL of dispersion was diluted with 2 mL of water. The size of the nanoparticles was calculated from the diffusional properties of the nanoparticles using Stokes-Einstein equation.[259] Each measurement was performed in triplicate. Error bars report the standard deviation of the nanoparticle size between measurements.

The film thickness of nanoparticles coated on ITO glass was measured using an Alpha-step IQ profilometer (KLA-Tencor). Scanning electron micrographs were collected using an FEI Nova NanoSEM with a beam acceleration voltage of 5 kV and a working distance of 5 mm. Nanoparticle-coated ITO substrates were fixed to an aluminum stub using carbon tape. UV-Vis analysis was carried out on diluted dispersions of nanoparticles in quartz cuvettes using a Cary 300 Bio UV-Visible spectrophotometer. Absorption spectra of nanoparticle films were measured on ~200 nm thick nanoparticle films on ITO.

3.2.6. Photoelectrochemical Measurements

For photoelectrochemical measurements, a 200 W Xe/Hg lamp was used as the light source (Ushio America, Inc) in conjunction with a visible light band-pass filter (FSQ-

KG 3, Newport Corp., λ: 300–700 nm) and neutral density filter (Thorlabs Inc.) to achieve an irradiation intensity of 100 mW cm^{-2}. The intensity of irradiant light was measured using a broadband power meter (841-PE, Newport Corporation) equipped with an Ophir thermal detector head (3A-P-SHV1). The cell configuration was designed to allow irradiation of the photoelectrode–electrolyte interface through the electrolyte, as shown in Figure 1.9. A water filter was placed in front of the electrochemical cell to minimize the heating of the electrolyte. Electrochemical measurements were performed using a Pine Bipotentiostat (AFC-BP1), and data were analyzed using Aftermath Scientific Data Organization software (ASTP-B01 Module). PEC measurements were performed using a 3-electrode configuration with a saturated calomel reference electrode (SCE) (+0.24 V vs. SHE) and a Pt wire as a counter electrode in 0.1M H_2SO_4 at room temperature. The electrolyte solution was purged with nitrogen (N_2) for one hour before electrochemical measurements to remove dissolved gases.[258]

3.2.7. Quantification of Hydrogen

The headspace of the electrochemical cell was analyzed for H_2 gas using a 5 mL syringe, fitted with an airtight valve (Series A-2, VICI Precision Sampling), and analyzed using Agilent Technologies 6890N GC system equipped with a thermal conductivity detector. A 2.13 m Agilent J&W GC packed column in stainless steel tubing was used (inner diameter 2 mm, HayeSep N packing material, 60/80 mesh size). Argon was used as a carrier gas at a flow rate of 30 mL min^{-1} under 46.2 psi. A detailed description of this apparatus has been reported previously.[258]

3.3. Results and Discussion

Aqueous dispersions of npP3HT and npPCBM were independently synthesized via the miniemulsion method using SDS and CTAB surfactants, respectively. The bright orange colour of P3HT in $CHCl_3$ transformed to dark green upon formation of the miniemulsion and became pink after evaporation of $CHCl_3$. Similarly, the purple colour of PCBM in $CHCl_3$ turned white during miniemulsion formation and deep yellow after evaporation of $CHCl_3$. The npPCBM dispersion was added dropwise to the npP3HT dispersion under sonication to form a 1:1 blend of npP3HT:npPCBM dispersion in aqueous media, which appeared red. The change of colour in different stages of

preparation is attributed to the change in physical characteristics of the emulsion such as changes in droplet size, concentration, and also photoabsorbers' liquid to solid transformation. These changes affect light scattered by the droplets both individually and collectively as a group, and also light absorbed by the photoabsorbing molecules. [260]

3.3.1. Material Characterization of Nanoparticles

The dynamic light scattering technique was used to calculate the size of nanoparticles dispersed in an appropriate solution. The particle size is computed using the Stokes-Einstein relationship (Equation. 3.2), which applies to infinitely dilute solutions. For DLS measurements, 10 µL of nanoparticle dispersions were diluted by adding 2 mL H_2O. During measurement, a laser beam (λ = 633 nm) is shone through nanoparticle dispersion which scatters the light. As the nanoparticles move due to Brownian motion, the scattering pattern also changes, and an auto-correlation function tracks these movements and provides information on the diffusion coefficient of nanoparticles at that temperature and medium. The radius of the nanoparticle is calculated from the diffusional properties of the nanoparticles using the Stokes-Einstein equation:[259]

$$D = \frac{k_B T}{3\pi\eta d} \tag{3.2}$$

where D is diffusion coefficient, k_B is Boltzmann constant, T is temperature, η is viscosity, and d is the hydrodynamic diameter.[261] DLS measures the hydrodynamic diameter of the nanoparticles, which is slightly larger than its actual radius. DLS measured particle sizes of npP3HT:npPCBM and np(P3HT:PCBM) dispersions are shown in Figure 3.4.

Plots of the particle size distribution of P3HT nanoparticles and PCBM nanoparticles determined by DLS are shown in Figure 3.4. The average diameters (Z_{avg}) of npP3HT and npPCBM were 110 nm and 412 nm, respectively. The larger size of npPCBM is due to the lower concentration of CTAB surfactant (0.3 mg mL^{-1} vs. 2 mg mL^{-1} for SDS), as the particle size is inversely proportional to surfactant concentration.[252] The particle size of the npP3HT:npPCBM dispersion was measured as 151 (Figure 3.4c). For comparison, nanoparticles comprising a blend of P3HT and PCBM, i.e., np(P3HT:PCBM) prepared via the precipitation method, possessed an average diameter of 140 nm (Figure 3.4d).

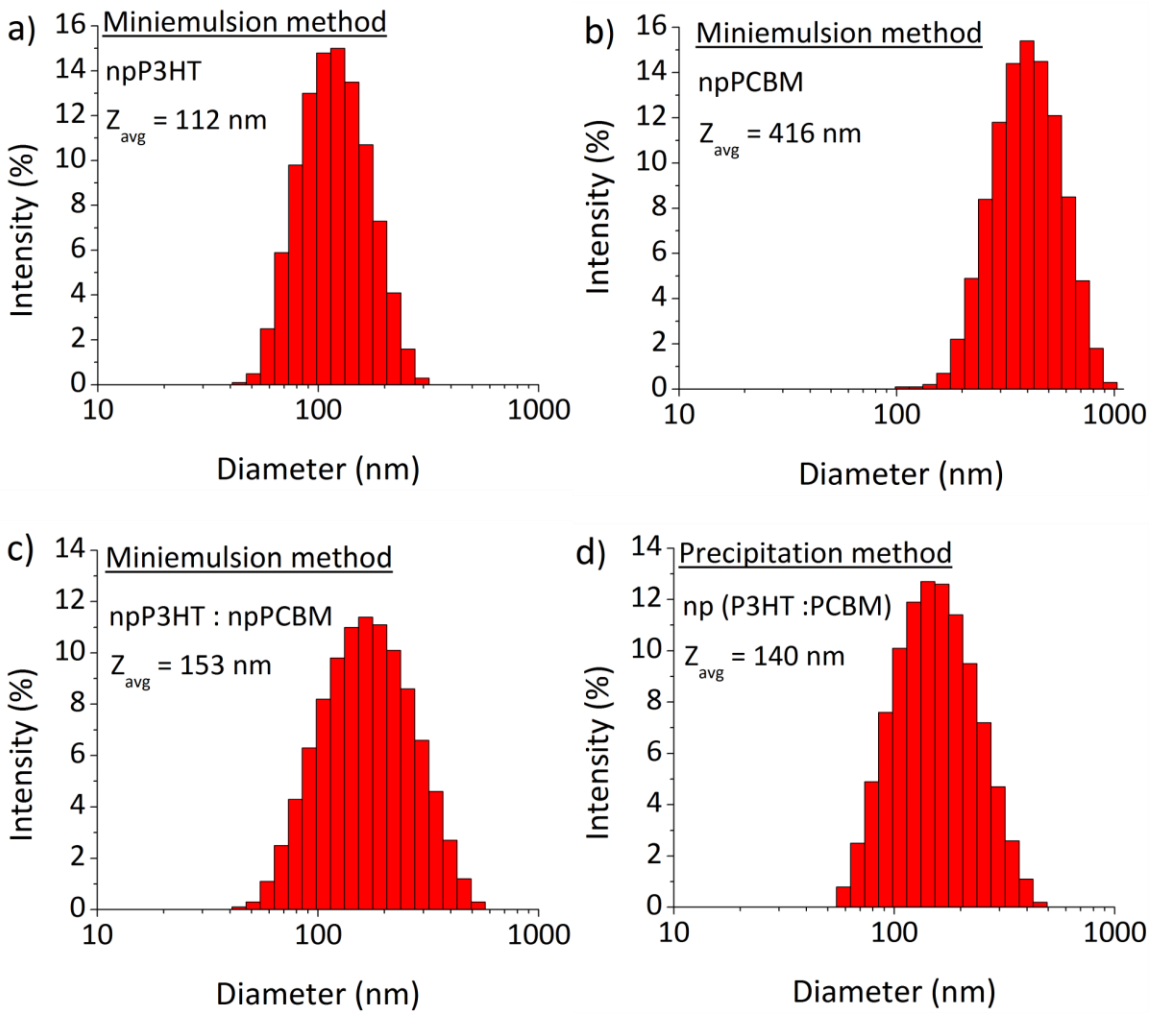

Figure 3.4 **Particle size distribution of miniemulsion nanoparticles: (a) npP3HT synthesized using SDS surfactant at critical micelle concentration (2 mg mL^{-1}), (b) npPCBM prepared in CTAB surfactant at critical micelle concentration (0.3 mg mL^{-1}), (c) a dispersion of npP3HT:npPCBM obtained by combining npP3HT and npPCBM prepared via miniemulsion method, and (d) a dispersion of np(P3HT:PCBM) prepared via the precipitation method.**

The DLS measured size of npP3HT and npPCBM mixture is different from the individual nanoparticles it comprises, as observed in Figure 3.4. The size of individual nanoparticles synthesized with different surfactant concentrations and their blend is shown in Figure 3.5. When an equal concentration of surfactants was used, nanoparticles of npP3HT (SDS, 2 mg mL^{-1}) and npPCBM (CTAB, 2 mg mL^{-1}) with sizes 118 nm and 106 nm were formed, respectively. The diameter of the npP3HT:npPCBM mixture, on the other hand, was measured as 992 nm. This surreal increase in value is postulated to be due to the Coulombic effect between positive (npPCBM) and negative (npP3HT) charged

particles that arise from cationic (CTAB) and anionic (SDS) surfactants. As this decreases the diffusion coefficient, the calculated particle size increases according to the Stokes-Einstein relationship (Equation. 3.2). Therefore, the DLS measured diameter of the nanoparticle mixture (i.e., 992 nm) is an artifact of measurement and does not represent the true size of the nanoparticles.

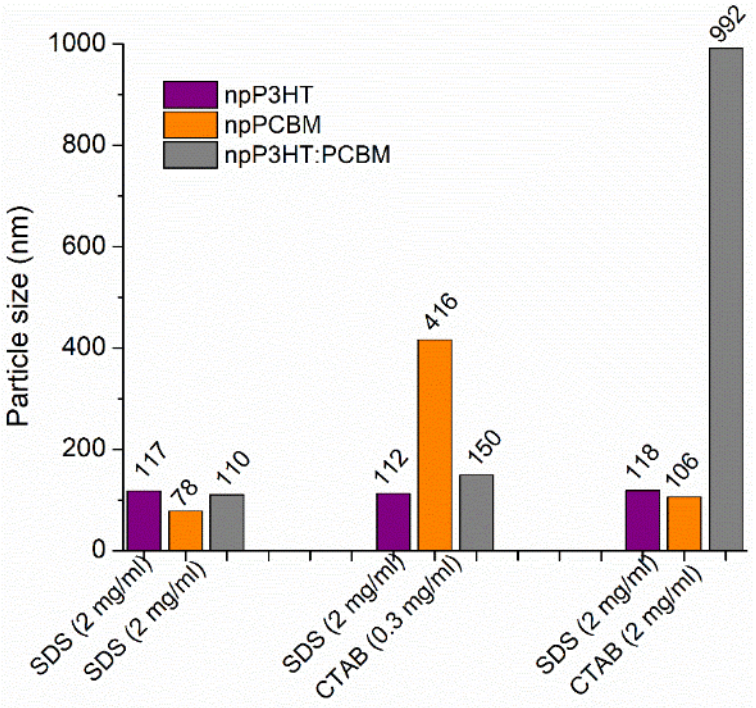

Figure 3.5 **Dynamic light scattering (DLS) measured size of npP3HT (orange) and npPCBM (purple) prepared via miniemulsion method using different concentrations of SDS and CTAB surfactants. When the two nanoparticles are mixed, the measured size is depicted as npP3HT:npPCBM (grey). Surfactant type and concentration used for synthesizing the nanoparticle (x-axis) are plotted against nanoparticle size (y-axis).**

The npP3HT:npPCBM dispersion prepared via the miniemulsion method appeared stable with no signs of agglomeration or precipitation after one month, as illustrated by the plot of average particle size with time (Figure 3.6). On the other hand, dispersions of np(P3HT:PCBM) prepared via the precipitation method agglomerated rapidly, and the onset of precipitation from the solution started to occur within a few hours.

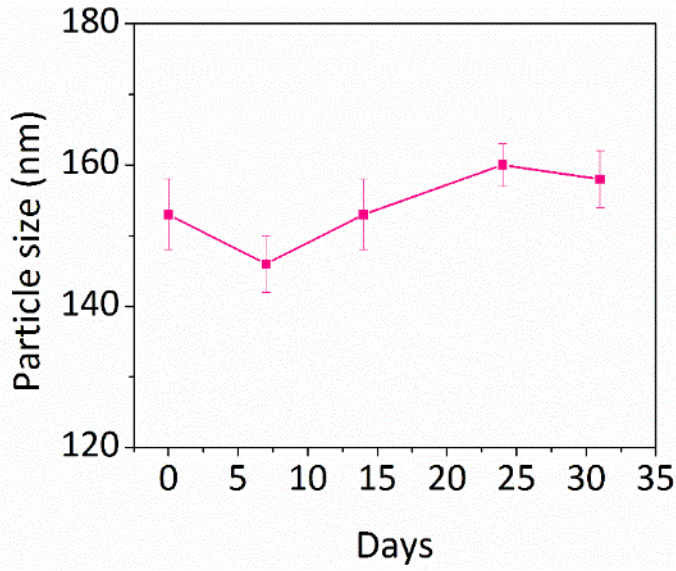

Figure 3.6 **DLS-determined particle size of npP3HT:npPCBM prepared by the miniemulsion method measured over 30 days, depicting the stability of the nanoparticle dispersions. (note: The error values represent deviation between experiments and not the nanoparticle size distribution).**

Nanostructured P3HT:PCBM films were prepared on ITO by spin-coating the npP3HT:npPCBM or np(P3HT:PCBM) dispersions (Figure 3.7). Onto these films, Pt nanoparticles were electrodeposited. Representative SEM images of these films are shown in Figure 3.8. In both examples, the nanoparticles form an interconnected network structure, but it is notable in npP3HT:npPCBM films where P3HT and PCBM nanoparticles can be easily distinguished. In this instance, npPCBM particles appear larger (~350 nm) and brighter than npP3HT particles (~90 nm). The particle diameters are less than those obtained by DLS, as DLS measures the hydrodynamic diameter of particles, resulting in calculated diameters being larger than the true particle size.[244] The much smaller bright spots are Pt particles (~50 nm). It was observed that Pt particles preferentially deposit on PCBM, which is consistent with PCBM accepting photogenerated electrons from P3HT, as illustrated in Figure 3.8.

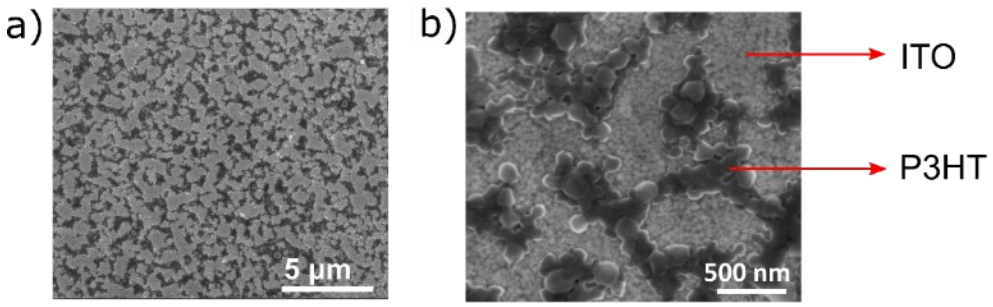

Figure 3.7 **SEM image of P3HT nanoparticles after one spin coat of the npP3HT dispersion on ITO. Bright areas are exposed ITO, and dark areas are P3HT nanoparticles. (b) Magnified image of (a) depicting partial coalescence of P3HT nanoparticles.**

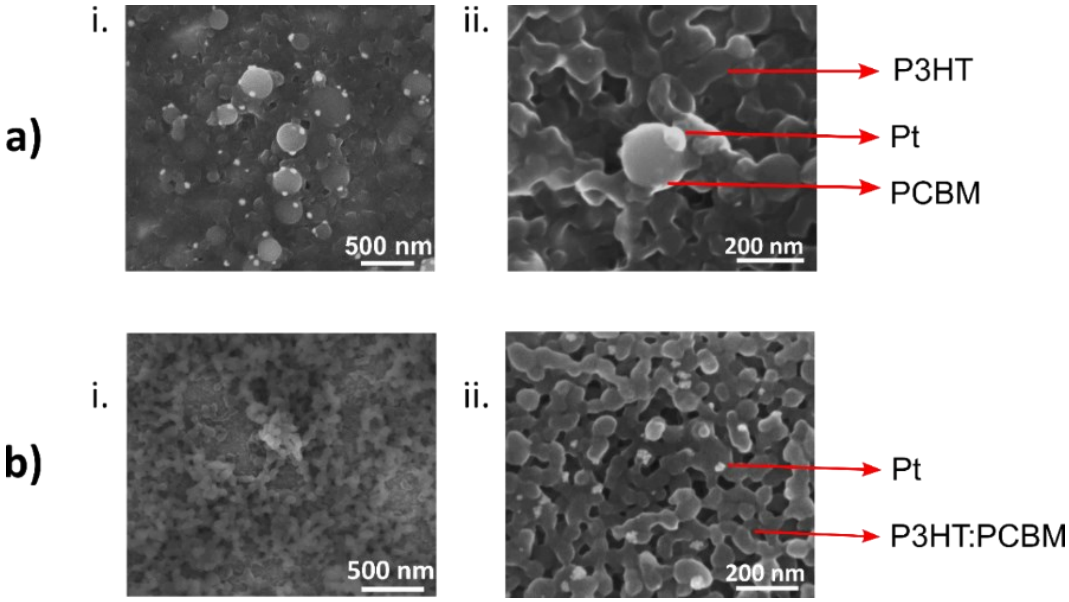

Figure 3.8 **SEM images of npP3HT:npPCBM films under different magnification. The larger, brighter particles are npPCBM, the darker interconnected particles are npP3HT, and the smaller bright spots are Pt. (b) SEM image of np(P3HT:PCBM) film, illustrating no distinction between P3HT and PCBM domains due to the well-blended nature.**

Energy Dispersive X-ray (EDX) elemental mapping was carried out to understand the distribution of npP3HT after spin coating. Thin films of npP3HT dispersion, prepared via the miniemulsion method, were cast onto the ITO substrate. After only one spin coat, the ITO substrate remains partially exposed. The npP3HT and ITO regions are identified by EDX elemental mapping of indium (In), oxygen (O), sulfur (S), and carbon (C), as shown in Figure 3.9. Where bright signals from indium and oxygen are observed, carbon and sulfur signals diminished and vice versa, indicating nanoparticle covered and uncovered areas of the ITO electrode.

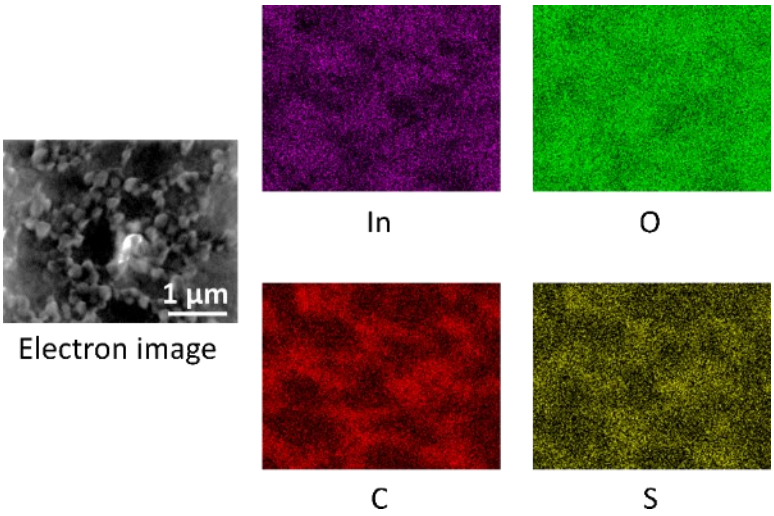

Figure 3.9 Energy Dispersive X-ray (EDX) elemental mapping of npP3HT on ITO along with elemental distribution map of indium (In), oxygen (O), carbon (C), and sulfur (S).

The absorption spectra of nanoparticle films prepared by spin coating dispersions of npP3HT:npPCBM and np(P3HT:PCBM) are shown in Figure 3.10. Three distinct peaks are observed, which are characteristic of P3HT; a broad peak is observed at 517 nm, with shoulders at 555 nm and 610 nm corresponding to 0–1 and 0–0 transitions respectively.[262-265] The shape and magnitude of vibronic shoulders have been shown to provide insight into the structural order within the P3HT domains.[266] Comparing the absorption spectra of the npP3HT:npPCBM dispersions and their films to np(P3HT:PCBM) dispersions and films, it is observed that although both films show peaks at similar wavelengths, a slightly increased vibronic shoulder intensity is observed for npP3HT:npPCBM particles, indicating a higher degree of structural order within P3HT domains.[262, 264]

When molecules transform from liquid to solid, they form aggregates of molecules. Depending on the orientation of polymer monomers in an aggregate, they are classified as H-type (face-to-face arrangement) or J-type (head-to-tail arrangement) aggregates.[267] The absorption characteristic of aggregates is different from that of individual monomers and it has been shown before that absorption spectra of P3HT can be modelled using the H-aggregate model of Spano.[262, 264] The ratio of the intensities of the 0–0 and 0–1 vibronic transitions is related to the free exciton bandwidth (W) which provides insight into interchain structural order.[263, 266]

$$\frac{A_{0-0}}{A_{0-1}} = \left(\frac{1 - 0.24W / E_p}{1 + 0.073W / E_p} \right)^2 \quad (3.3)$$

In Eqn. 1, E_p is the energy of C=C stretching (~170 meV), $\frac{A_{0-0}}{A_{0-1}}$ is the ratio of the intensity of the vibronic shoulders in the UV-Vis spectrum (at 610 nm and 555 nm).

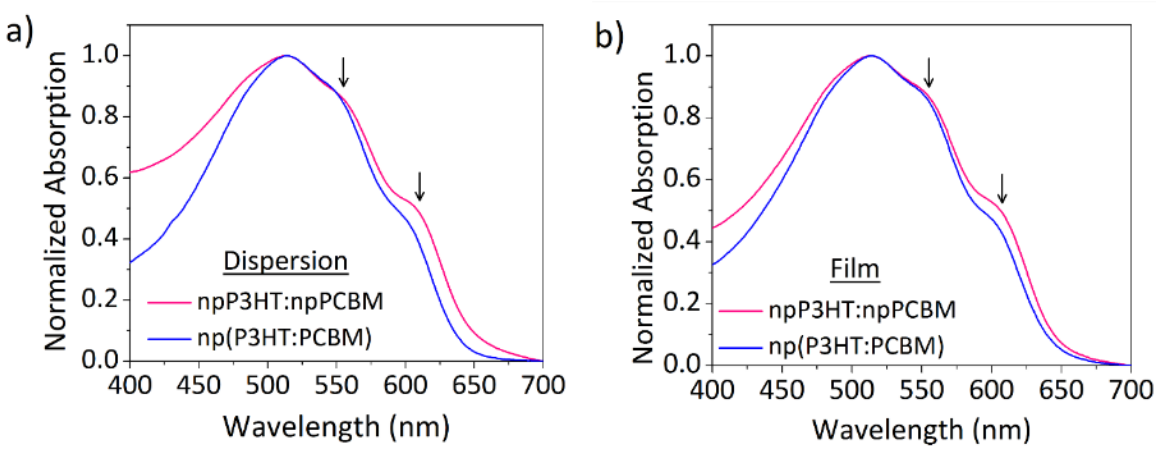

Figure 3.10 Normalized UV-Vis absorption spectrum of (a) P3HT:PCBM nanoparticle dispersions prepared via miniemulsion and precipitation methods and (b) the corresponding nanoparticle films spin-coated on ITO.

The exciton bandwidth, W, of npP3HT:npPCBM films was calculated to be 157 meV, which is lower than for np(P3HT:PCBM) films (193 meV), and indicates a high structural order (i.e., crystallinity) within nanoparticles prepared *via* miniemulsion method. This is due to the npP3HT:npPCBM being comprised of individual npP3HT and npPCBM nanoparticles, as it has been previously shown that the addition of PCBM disrupts the long-range order of the P3HT chains in P3HT:PCBM thin films.[268, 269] Consequently, it is expected that, due to increased interchain packing and interparticle connectivity, npP3HT:npPCBM films exhibit higher charge carrier mobility than np(P3HT:PCBM) films.[268, 270, 271]

3.3.2. (Photo)electrochemical Characterization of Photoelectrodes

Photoelectrochemical measurements were carried out using npP3HT:npPCBM and np(P3HT:PCBM) films, onto which Pt was deposited, in 0.1M H_2SO_4 under visible light (100 mW cm^{-2}) irradiation at room temperature in three-electrode configuration with

ITO/P3HT:PCBM NPs/Pt as the working electrode, a Pt wire counter electrode, and a saturated calomel electrode (SCE) reference electrode. Photopotential and photocurrent measurements were carried out to gain insight into the dynamics of the photoelectrode. The photopotential, E_{ph}, which is the driving force of the photoelectrode, is the difference between the Fermi level of the bulk semiconductor under illumination and the redox potential of the species in solution.[272] The photopotential (E_{ph}) was measured via open circuit potential (OCP) measurements (as discussed in section 1.3.2).

$$E_{Ph} = \left| E_{OCP,dark} - E_{OCP,light} \right| \tag{3.4}$$

$E_{OCP,dark}$ was −0.05 V (after stabilizing for 100 s) for ITO/npP3HT:npPCBM/Pt electrodes (Figure 3.11). Upon illumination, E_{OCP} shifts to a more positive potential which is characteristic of a p-type photoelectrode and attained a value of more than +0.250 V. From OCP measurements in dark and light, E_{ph} is estimated to be 0.3 V. A similar value was observed for ITO/np(P3HT:PCBM)/Pt photoelectrodes.

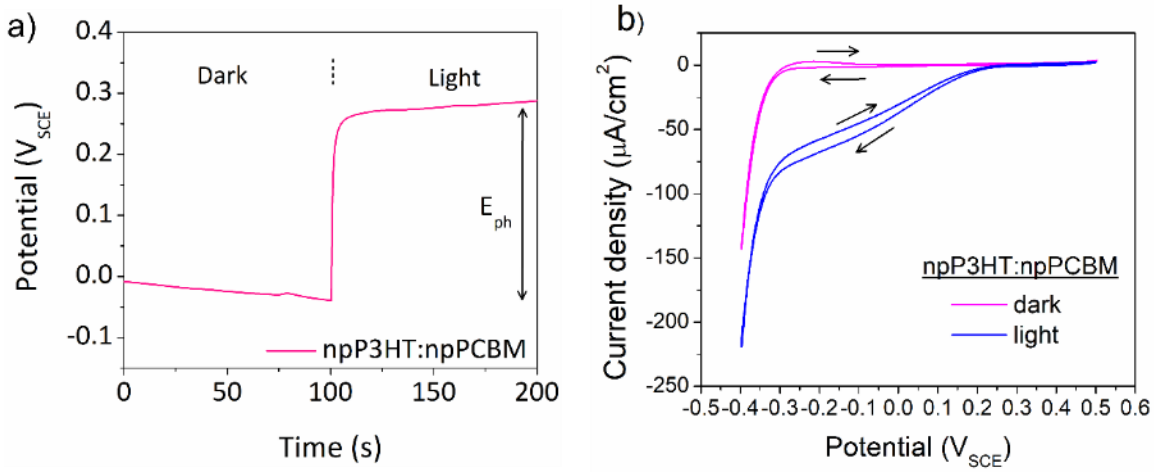

Figure 3.11 Graph depicting (a) open circuit potential and (b) cyclic voltammogram of P3HT:PCBM nanoparticle films prepared via miniemulsion method measured in both light (I=100 mW cm^{-2}, λ: 300–700 nm) and dark conditions in 0.1M H_2SO_4.

A cyclic voltammogram of the electrode performed in the potential range of 0.5 V to −0.4 V under dark and light conditions with a 5 mV s^{-1} scan rate is shown in Figure 3.11b. During the dark scan, the photocathode was not active and showed negligible current density till −0.35 V, after which the current density started to increase due to significant band bending and charge flow across the interface caused by the applied potential. The photocathode is significantly active under illumination, and the photocurrent

started to increase at 0.2 V compared to the dark current and continued to rise till −0.32 V. Then, the slope of the current density changed, indicating the onset of an electrocatalytic reduction process that is not due to the photoactivity of the electrode.

Linear sweep voltammetry curves for nanoparticle and thin-film electrodes were measured between +0.6 V_{SCE} and −0.4 V_{SCE} and subjected to five-second intervals of dark and illumination are shown in Figure 3.12. Cathodic and anodic current regions are labelled as regions I and II, respectively. The photocurrents increase with increasing negative applied potential to 100 μA cm^{-2}, wherein the residual current is negligible in the absence of light. The onset potential (E_{onset}) for photocathodic current is ~0.4 V_{SCE} (0.64 V_{SHE}) for the npP3HT:npPCBM electrodes, while E_{onset} of the np(P3HT:PCBM) electrodes is substantially more negative (~0.1 V_{SCE}, i.e., 0.34 V_{SHE}). Thus, the minimum additional potential thermodynamically required to photoelectrochemically split water (1.23 V) is thus 0.59 V and 0.94 V for npP3HT:npPCBM and np(P3HT:PCBM) electrodes respectively. For comparison, a planar P3HT:PCBM electrode is shown in Figure 3.12c.

Photoelectrolysis of the nanoparticle and thin-film electrodes was carried out at a constant potential of −0.24 V_{SCE} (0 V_{SHE}) with alternate dark and light cycles, the results of which are shown in Figure 3.12d–f. Negligible current densities were observed under dark conditions, while photocurrent densities of −65 μA cm^{-2} and −35 μA cm^{-2} were measured for ITO/npP3HT:npPCBM/Pt and ITO/np(P3HT:PCBM)/Pt photoelectrodes respectively. Photoelectrolysis of ITO/npP3HT:npPCBM/Pt electrode prepared from freshly synthesized nanoparticles and that prepared from nanoparticles after storing for an extended period yielded similar photocurrents, indicating the photoactive stability of the synthesized nanoparticles (Figure 3.13). Photocurrents from the nanoparticle electrodes are significantly higher than the planar (ITO/P3HT:PCBM/Pt) electrode which is less than −10 μA cm^{-2}.

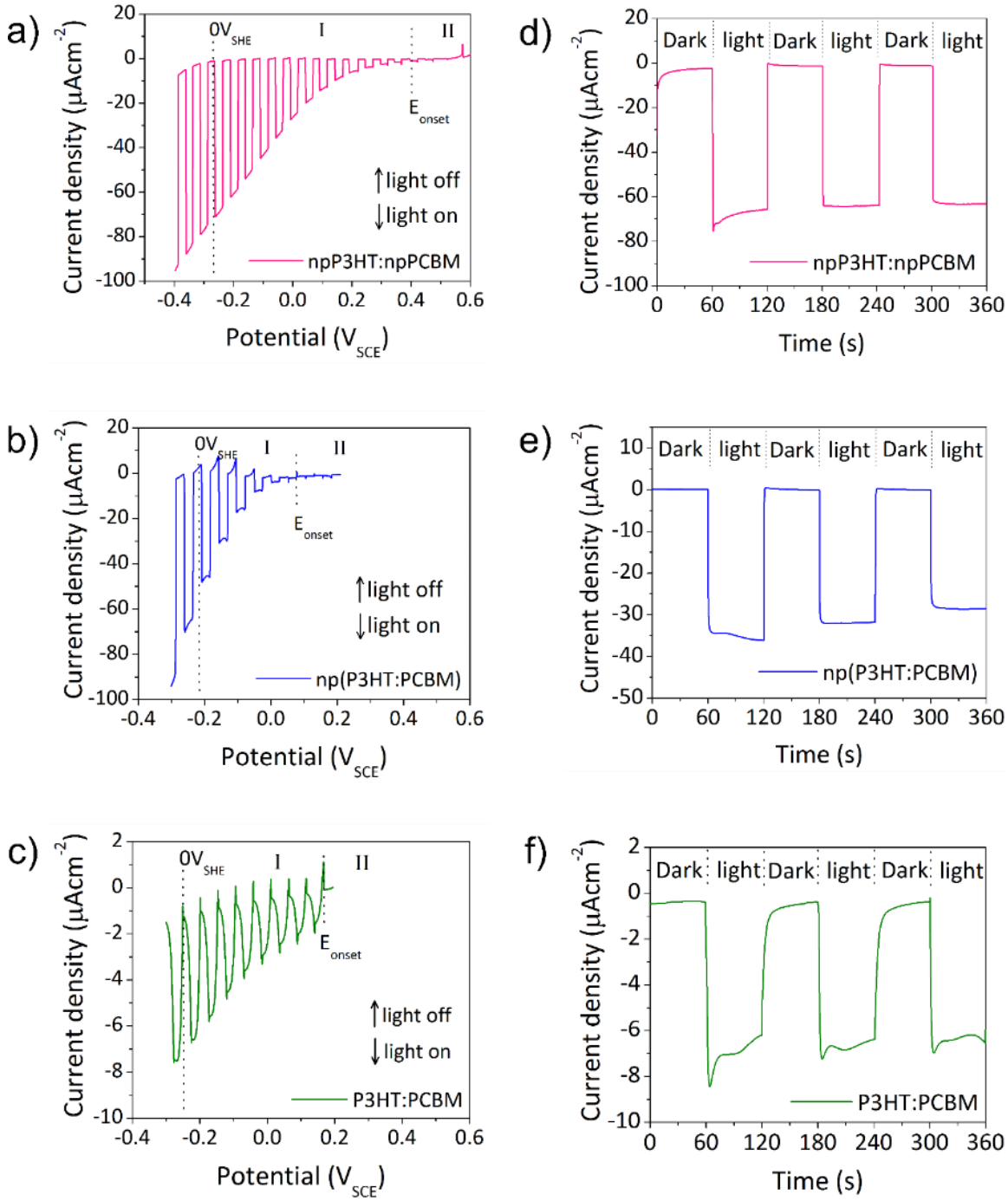

Figure 3.12 **(a–c) Linear sweep voltammetry and (d–f) photoelectrolysis of ITO/npP3HT:npPCBM/Pt (pink), ITO/np(P3HT:PCBM)/Pt (blue) and ITO/P3HT:PCBM/Pt (green) photocathodes. LSV measurements were carried out under chopped light illumination 5 s dark and 5 s light at 5 mV/s. Photoelectrolysis of the electrodes was tested with intermittent light illumination at −0.24 V_{SCE} (0.0 V_{SHE}). Tests were carried out in 0.1 M H_2SO_4 with 100 mW cm^{-2} (λ: 300–700 nm) illumination intensity. Pt and SCE were used as counter and reference electrodes, respectively.**

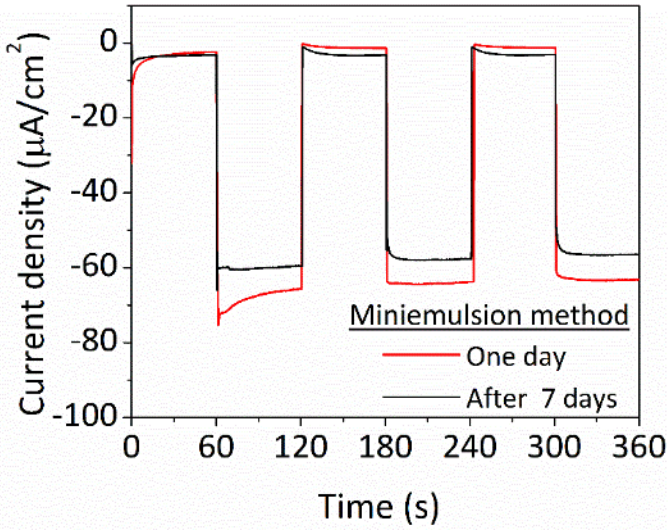

Figure 3.13 Photoelectrolysis of ITO/npP3HT:npPCBM/Pt photoelectrodes prepared by depositing miniemulsion nanoparticles on an ITO within one day and after storing the nanoparticle dispersion for seven days under intermittent light illumination (I=100 mW cm^{-2}, λ: 300–700 nm) in 0.1M H_2SO_4 at −0.24 V_{SCE} (0.0 V_{SHE}) with Pt and SCE as counter and reference electrodes, respectively.

Photograph of an ITO/npP3HT:npPCBM/Pt photoelectrode immersed in the photoelectrochemical cell, taken during photoelectrolysis at −0.24 V_{SCE} (0.0 V_{SHE}) is shown in Figure 3.14, where gas bubbles can be observed evolving from the electrode surface. To identify the liberated gas, GC analysis of the head-space of the photoelectrochemical cell was carried out as previously described (Figure 3.15).[244] As a control experiment, hydrogen was electrolytically generated by applying −0.35 V_{SCE} to Pt foil for 10 s passing 37 mC of charge, with Pt wire and an SCE serving as counter and reference electrodes respectively, immersed in 0.1M H_2SO_4. The evolved hydrogen was then quantitatively analyzed.[244] From the elution trace of the GC chromatographs, the gas evolved from the photocathode was confirmed to be hydrogen (Figure 3.15), and from the Coulombic charges passed, the quantity of hydrogen liberated was calculated to be 0.63 μmol hr^{-1} cm^{-2} with a minimum of 70% Faradaic efficiency. This reduced Faradaic efficiency is attributed to the formation of oxygen electron transfer complex [$P3HT^{+}$:O^{2-}] which is known to trap electrons[258, 273, 274] and also to the inefficiencies in hydrogen collection and measurement.

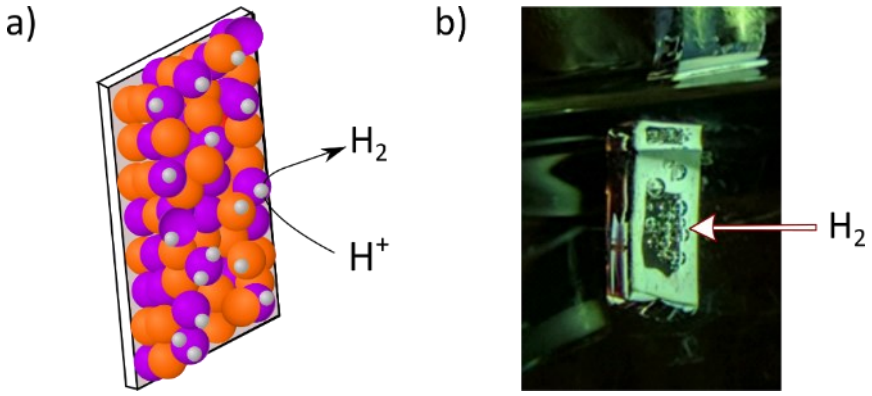

Figure 3.14 **(a) Schematic depicting npP3HT(orange):npPCBM(purple) nanoparticle coated ITO substrate and Pt catalyst (grey) and (b) photograph of photocathode during photoelectrolysis showing H_2 evolution.**

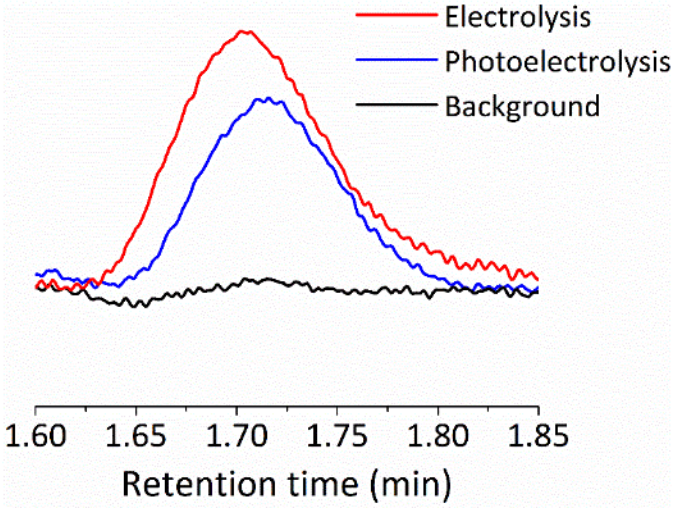

Figure 3.15 **Gas chromatogram of evolved gas from miniemulsion (npP3HT:npPCBM) nanoparticle film (blue) after electrolysis for one hour at −0.24 V_{SCE} in 0.1M H_2SO_4, with 100 mW cm^{-2} illumination. The reference curve (red) was obtained by analyzing the hydrogen generated from Pt foil WE when −0.35 V_{SCE} was applied for 10 s passing 37 mC of charge. (CE: Pt wire, RE: SCE, Electrolyte: 0.1M H_2SO_4). Background - ambient air (black). Y-axis: GC detector signal.**

3.4. Conclusion

npP3HT and npPCBM nanoparticles were individually prepared by miniemulsion in an aqueous solution using surfactants of opposite charge. The prepared nanoparticles displayed good stability without agglomeration or precipitation due to the presence of

surfactants in the dispersion. The individual dispersions were mixed to form stable dispersions that can be cast conformally on ITO to form water-insoluble films. During film casting the nanoparticles partially coalesce to form a P3HT:PCBM bulk-heterojunction film. UV-Vis analysis of the film indicated higher structural order in miniemulsion prepared nanoparticle film. Irradiation of films electrocatalyzed with Pt nanoparticles yielded a higher photocurrent and positive onset potential compared to films prepared from dispersions of homogeneous nanoparticles of P3HT/PCBM. By separating the npP3HT and npPCBM nanoparticles, the long-range order within P3HT nanoparticles and, consequently, the electronic properties are preserved. The synthesized miniemulsion BHJ electrode exhibited higher photocurrent and onset potential than the planar BHJ electrode and the nanoparticle BHJ electrode prepared via the precipitation method.

Chapter 4.

CuO Nanoparticle-based p-n Bulk-heterojunction Photocathodes

Sections of this chapter have been reprinted with permission from Rajasekar, S.; Tiwari, V.; Srivastva, U.; Holdcroft, S. *ACS Appl. Energy Mater.* **2020**, 3, 9, 8988–9001, Copyright 2020, American Chemical Society. The work presented in this chapter are the contributions made to the paper by S. Rajasekar.

4.1. Introduction

Copper (II) oxide (CuO) is an abundant, environmentally-friendly material used in many applications, including solar energy conversion,[184, 216, 275] superconductors,[276] bio-medical,[277] and sensor applications.[278, 279] It is a p-type semiconductor because of the mobile holes caused by the presence of Cu vacancies.[280] Owing to this, CuO semiconductors display bandgap in the range of 1.2–1.8 eV which is dependent on the preparation method. This low bandgap nature allows CuO to absorb a significant portion of the solar light. Furthermore, the valence and conduction band edges of CuO straddle the electrochemical potential for the hydrogen evolution reaction (HER) potential, as shown in Figure 4.1, making it one of the potential photocathodes for solar water splitting.[92, 191, 281] Theoretically, CuO is capable of achieving maximum photocurrent density of 29 mA cm^{-2} and STH conversion efficiency of 35%.[53, 227, 272]

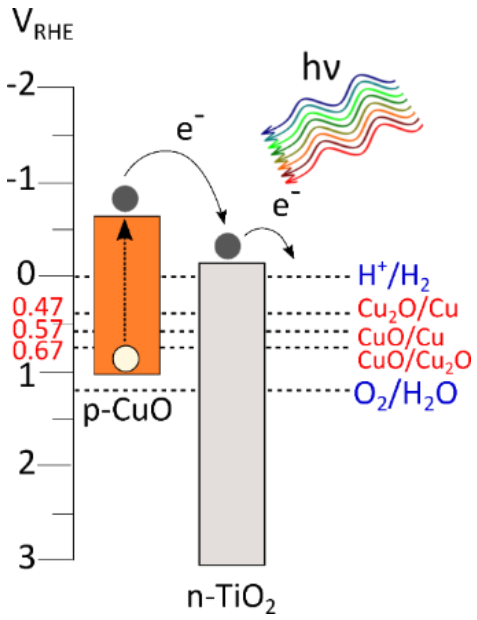

Figure 4.1 **Schematic depicting valence and conduction band energies of CuO and TiO_2 along with electron transfer pathway upon illumination (note: potential values are represented for pH 0).**

Despite possessing attractive properties, CuO is not a widely studied photocathode owing to the concern that it is incapable of reducing protons, as the redox potentials associated with copper oxide lie between those of water (Figure 4.1). Thus, it is more likely that photogenerated electrons reduce CuO to Cu_2O or Cu rather than reduce H^+ to H_2 gas. For example, at −0.1 V applied potential (ignoring the effect of pH on potential), the overpotential for H^+ reduction is −0.1 V ($\Delta E_{HER} = -0.1 - 0\ V_{SHE}$), but for CuO reduction the overpotential is −0.77 V [$\Delta E_{(Cu2+/Cu+)} = -0.1 - 0.67$ V]. Thus, of the two competing reactions, i.e., proton reduction and CuO reduction, the latter is thermodynamically more favourable.

$$2H^+ + 2e^- \longrightarrow H_2 \qquad E_{HER}=0.0-0.059pH \qquad (4.1)$$

$$Cu_2O + 2H^+ + 2e^- \longrightarrow 2Cu + H_2O \qquad E=0.471-0.059pH \qquad (4.2)$$

$$CuO + 2H^+ + 2e^- \longrightarrow Cu + H_2O \qquad E=0.570-0.059pH \qquad (4.3)$$

$$2CuO + 2H^+ + 2e^- \longrightarrow Cu_2O + H_2O \qquad E=0.669-0.059pH \qquad (4.4)$$

$$H_2O \longrightarrow \tfrac{1}{2}O_2 + 2H^+ + 2e^- \qquad E_{OER}=1.228-0.059pH \qquad (4.5)$$

However, a series of recent publications established that appropriately protected CuO might, in fact, be employed as a photoelectrode to evolve H_2 by modifying the kinetics of the reduction reaction, such as by employing protective/catalyst layers. [216, 275, 282-285] From the literature reports, the photocurrent density achieved using CuO photocathodes is ~2 mA cm^{-2}, far less than the maximum theoretical photocurrent density.[275] This is believed to be due to the high exciton recombination rate that arises because of the high ratio of the light absorption length to the exciton diffusion length.[286-288] The optical absorption length of CuO is in the order of microns, but the exciton lifetime is <50 ps,[286, 287], and the carrier diffusion length is just ~40 nm.[289] Thus, photogenerated electrons are more likely to recombine before reaching the electrode/electrolyte interface.

Based on the premise mentioned above, separation of the charges before recombination may be possible by locating an acceptor with suitable band edge positions close to CuO (as shown in Figure 4.1). Among the available materials, TiO_2 was chosen for this purpose. TiO_2 is an electrochemically stable, abundant, and widely studied photocatalyst that may be used in conjunction with CuO.[290, 291] The valence and conduction band energy levels of TiO_2 form a type-II band alignment as shown in Figure 4.1.[288, 292-294] Previous reports that studied photocathodes with an appropriately protected TiO_2 (50–100 nm) thin-film achieved higher photocurrents and stability.[197, 295] Furthermore, it is a wide bandgap (>3 eV) semiconductor and absorbs only UV wavelength which comprises only 3.5% of the total solar radiation. Hence, by using TiO_2 in combination with CuO, the interference of the former in the observed photocurrents can be assumed to be negligible, which offers an effective way to probe the effect of the BHJ in CuO photoelectrodes. This study systematically explores the effect of the donor:acceptor ratio on the photoelectrochemical behaviour of randomly distributed NPs (Figure 2.11c) of CuO and TiO_2 to form BHJ photoelectrodes.

4.2. Experimental Methods

4.2.1. Nanoparticle Synthesis

Nanoparticles for the preparation of (npCuO:npTiO$_2$) BHJ photoelectrodes were either commercially procured from Sigma-Aldrich or synthesized via the co-precipitation method: (i) BHJ photoelectrodes using commercially obtained NPs were achieved by mixing the required amount of copper (II) oxide (CuO, 50 nm) and titanium dioxide (TiO_2,

Aeroxide P25, 21 nm) nanoparticles; (ii) for co-precipitation synthesis 0.1M copper nitrate ($Cu(NO_3)_2$ $2.5H_2O$) and titanium chloride ($TiCl_4$) solutions were stirred together for 1 hour, and the pH was adjusted to 9 by adding ammonia (25% NH_3 solution). The resultant precipitates were separated and washed in ethanol three times and then annealed at 400 °C for 2 hours.

4.2.2. Fabrication of Photoelectrodes

For the preparation of FTO/npCuO photoelectrodes, 30 mg of commercial CuO NPs was disaggregated in a mortar and pestle, followed by the addition of 30 µL of acetylacetone and 30 µL of polyethylene glycol. The mixture was ground until a homogenous viscous paste was achieved, at which stage 1 mL of ethanol was added to form a nanoparticle dispersion. The slurry was mixed thoroughly for 30 minutes. FTO-coated glass slides (Aldrich, resistance – 8 Ω sq^{-1}) were cleaned sequentially under sonication for 10 minutes in soapy water, DI water, acetone, and ethanol. The CuO NP dispersion was deposited onto FTO transparent conducting slides by drop-casting, and the electrodes were annealed at 600 °C for 2 hours to increase the crystallinity of CuO and to facilitate electrical contact between individual NPs.[296, 297] (note: As inorganic semiconductors require high-temperature annealing at which ITO electrodes are known to undergo performance deterioration and display high resistance, FTO was used as a substrate for inorganic semiconductors instead of ITO substrates used in Chapter 3)[298] To prepare FTO/npCuO:npTiO$_2$ photoelectrodes, a percentage (x) of TiO_2 NPs were mixed with CuO NPs, and the mixture was deposited as described above, resulting in randomly distributed npCuO:npTiO$_2$ bulk-heterojunction electrodes.

For BHJ electrode preparation, the thickness of the electrode was maintained at 10 µm for different ratios of BHJ electrodes. This is achieved by preparing several electrodes for each BHJ composition by varying the amount of NP mix deposited on the electrode and then the electrode with the desired thickness, that is ~10±1 µm (measured using a Bruker DektakXT surface profilometer) was selected. Thicker films were deposited to verify the effect of BHJ architecture in transporting the charges from deep within the electrode to the surface. Photoelectrode preparation for BHJ NPs synthesized via the co-precipitation route followed the same procedure as mentioned before. To differentiate this from the commercial NPs, the electrodes were indicated as FTO/cp-(npCuO:npTiO$_2$), where cp refers to co-precipitation.

4.2.3. Deposition of TiO_2

Thin films of TiO_2 protecting layer were obtained via spin coating titanium(IV) isopropoxide (TTIP) solution. First, TTIP was stabilized in diethanolamine in a 1:2 molar ratio by stirring overnight, and then the solution was adjusted to 0.1M by adding DI water. This solution was spin-coated (30 µl $cycle^{-1}$) on top of electrodes at 1500 rpm for 60 s, followed by annealing at 400 °C for 2 hours (3 °C min^{-1}).

4.2.4. Deposition of Pt

Platinum NPs as an HER catalyst were electrochemically deposited on top of photoelectrodes following the same procedure as described before.[299] In short, applying a potential of −0.1 V_{SCE} to an electrode immersed in 1 mM aqueous solution of H_2PtCl_6 for 15 minutes in the dark results in deposition of 89 µg of Pt per cm^2.

4.2.5. Characterization of Nanoparticles

Material Characterization: The electrode morphologies were examined using scanning electron microscopy (SEM) (JEOL, JSM 6610LV) operated in the secondary electron mode using an accelerating voltage of 20 kV. The crystallinity of the NPs was analyzed by X-Ray diffraction (XRD) using a Malvern Panalytical instrument equipped with an SSD monochromator and Cu Kα (1.54 Å) radiation source at a scan rate of 2^o 2θ min^{-1}. Raman spectroscopic measurements were recorded using a HORIBA LabRAM HR evolution instrument.

Electrochemical Characterization: Electrochemical measurements were performed using IviumStat, a multichannel potentiostat in a three-electrode configuration with a saturated calomel reference electrode (SCE) (+0.24 V vs. SHE) and a Pt mesh as the counter electrode in N_2-purged 0.5M Na_2SO_4 (pH 5.5) at room temperature. The potential values were converted from the SCE reference scale to the RHE scale using the Nernst equation (Equation 4.6), compensating for the effect of pH on the potential.

$$E_{RHE} = E_{SCE} + 0.241 + 0.059\ pH \quad (4.6)$$

The electrochemical cell was designed to allow irradiation of the photoelectrode–electrolyte interface through the electrolyte. A solar simulator (Photo Emission Tech Inc.,

model SS300 AAA) was used as the light source for photoelectrochemical measurements, which illuminated the electrode surface with AM1.5G (100 mW cm^{-2}) radiation produced from a 300 W Xe lamp. The electrode surface was covered with epoxy to expose only 0.2–0.3 cm^2 area for electrochemical studies.

Mott-Schottky Analysis: Mott–Schottky analysis was conducted using Iviumsoft software in the cathodic direction from 0.8 V to −0.8 V_{SCE} with a scan rate of 25 mV per step using an applied frequency of 1 kHz.

Electrochemical Impedance Spectroscopy (EIS): EIS studies were carried out in the dark using an alternating current (AC) signal in the frequency range of 10^5 Hz to 1 Hz and an amplitude of 10 mV_{rms}.

4.2.6. Quantification of Hydrogen

The detection of hydrogen was carried out by analyzing the sample collected from the headspace of the electrochemical cell using a 25 mL syringe fitted with an air-tight valve and a PerkinElmer Clarus 580 gas chromatography (GC) system. Reference H_2 was obtained by electrolysis in N_2-saturated 0.5M Na_2SO_4 (pH 5.5) solution using Pt working and counter electrodes by applying −0.1 V_{RHE} for 15 min.

4.3. Results and Discussions

4.3.1. SEM Microscopy Analysis

The nanoparticulate electrodes were prepared by the drop-casting method as described in the experimental methods section. The microstructure of FTO/npCuO electrodes before and after annealing at 600 °C is shown in Figure 4.2. After annealing, the measured particle sizes of 100–150 nm were larger than their initial size of 50 nm, indicating that the NPs fuse during annealing. Furthermore, the NPs were observed to have partially coalesced (Figure 4.3a), establishing an electrical connection between particles throughout the film, which is desirable for charge transportation.

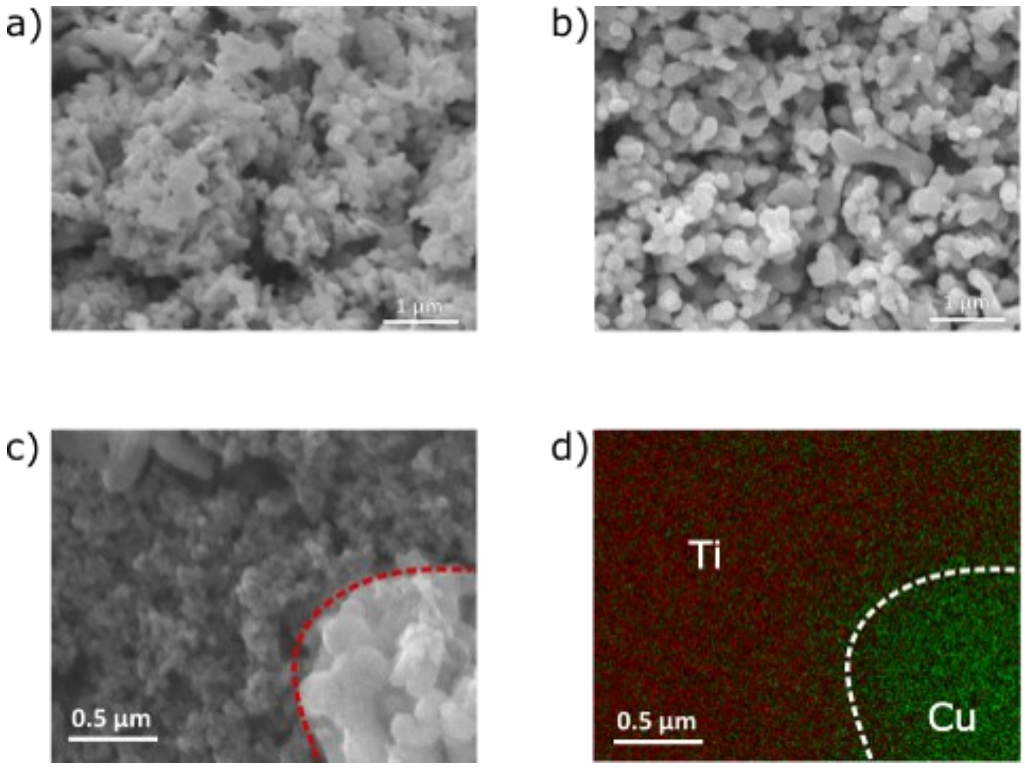

Figure 4.2 Scanning electron micrograph of CuO nanoparticles (a) before and (b) after annealing at 600 °C. (c) Micrograph and corresponding (d) Energy dispersive X-ray (EDX) elemental mapping image of npCuO:npTiO$_2$ after thermal annealing at 600 °C, showing the elemental distribution of Cu and Ti.

SEM images of FTO/npCuO:npTiO$_2$ BHJ electrodes prepared by varying the mass ratio of npCuO to npTiO$_2$ are shown in Figure 4.3. As the electrical conductivity of CuO [294, 300] is significantly higher than TiO$_2$, [301] CuO NPs appear brighter than TiO$_2$ NPs in the SEM images. The contrast and size difference between CuO (~150 nm diameter) and TiO$_2$ (~25 nm diameter) make it easy to visually distinguish the particles, which is also confirmed by energy-dispersive X-ray spectroscopy elemental analysis (Figure 4.2). In the BHJ electrodes, TiO$_2$ NPs occupy the spaces between CuO NPs, as shown in Figure 4.3. However, with higher percentages of TiO$_2$ (>50 wt%), the distance between CuO NPs increased to a point where there appeared to be no electrical connection between CuO NPs in the film.

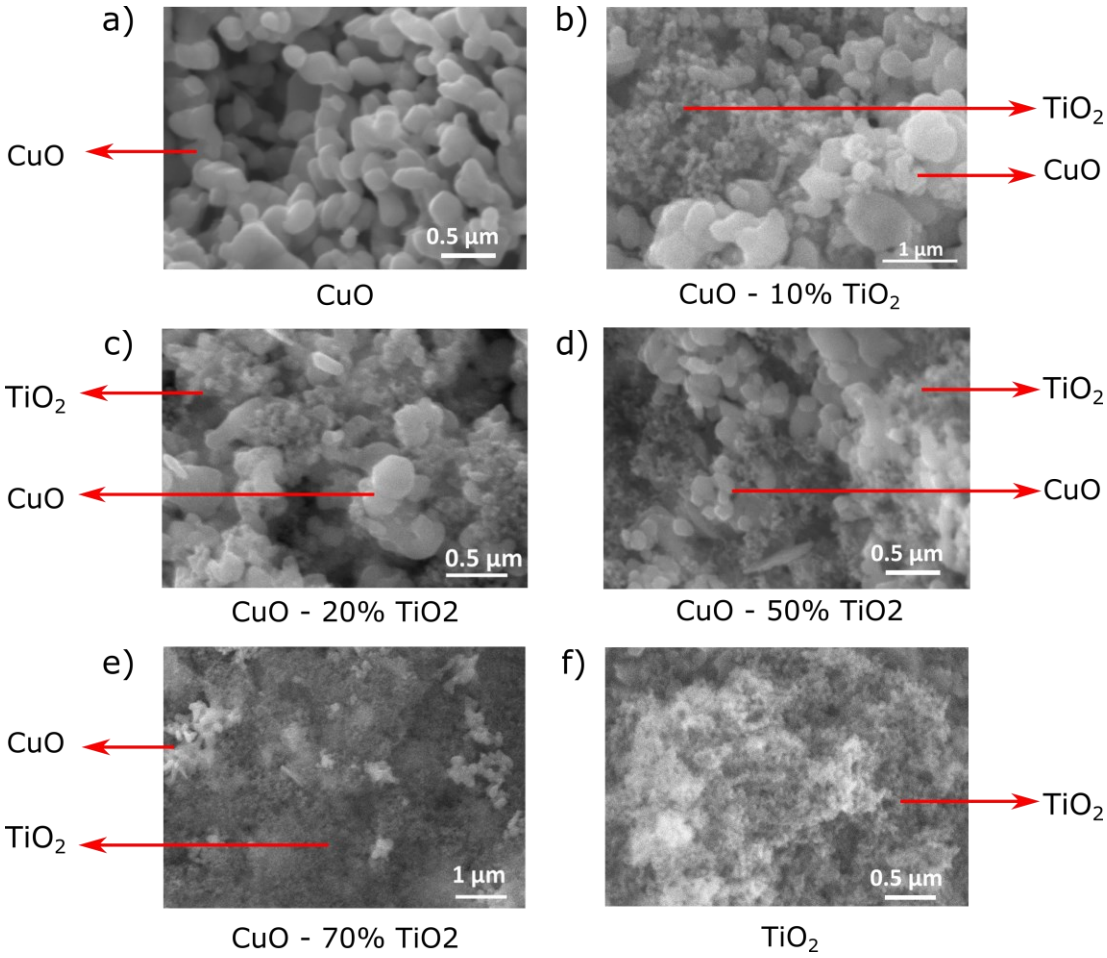

Figure 4.3 **Scanning electron microscope image of npCuO:npTiO$_2$ BHJ electrode with different weight percentages of TiO$_2$ after annealing at 600 °C. (a) CuO, (b) CuO-10%TiO$_2$, (c) CuO-20%TiO$_2$, (d) CuO-50%TiO$_2$, (e) CuO-70%TiO$_2$ and (f) TiO$_2$, representing 0, 10, 20, 50, 70, and 100 wt% TiO$_2$, respectively.**

4.3.2. X-Ray Diffraction Analysis

In addition to morphology, the crystallographic orientation of the photoelectrode plays an important role in the photoelectrodes' performance and stability.[302] Hence, crystal plane orientation and phases present in the electrode after annealing were analyzed using X-ray diffraction (XRD), and the results are shown in Figure 4.4. For pure npCuO photocathodes, characteristic XRD peaks were observed at 32.54º, 35.58º, 38.8º, 48.8º, 51.54º, and 53.54º, corresponding to (110), ($\bar{1}$10), (111), ($\bar{2}$02), (020), and (202) crystal planes respectively (JCPDS 48-1548). This indicates the polycrystalline nature of the film with the rest of the peaks arising from the FTO substrate. For pure TiO$_2$ electrodes, peaks were observed at 25.5º, 27.71º, and 48.3º, assigned to (101), (110) and (200) planes

emerging from the anatase and rutile phases of TiO_2 (Anatase – JCPDS 21-1272, Rutile – JCPDS 21-1276). For FTO/npCuO:npTiO$_2$ BHJ electrodes with increasing npTiO$_2$ content, an increase in the intensity of the TiO_2 peaks was observed concomitant with a decrease in scattering intensity corresponding to CuO. All the observed peaks can be accounted for by considering CuO, TiO_2, and FTO; no new phases were formed as a result of annealing.

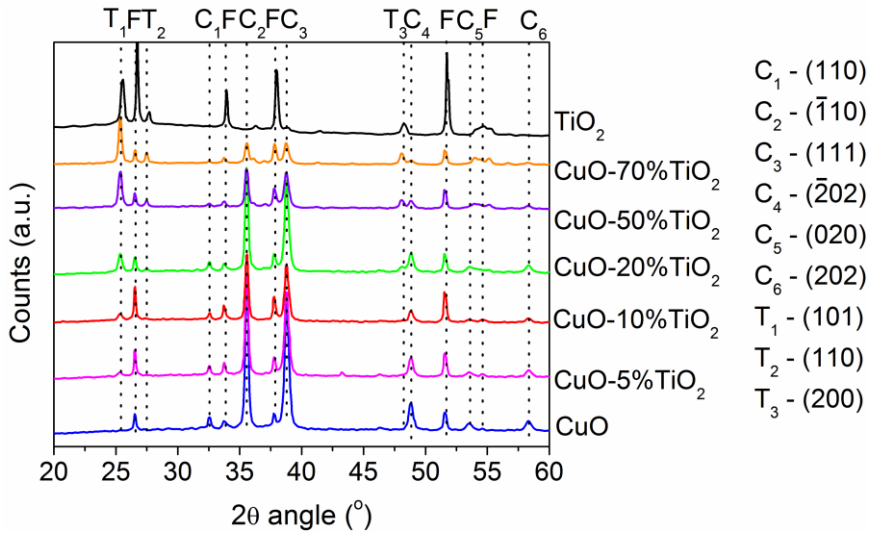

Figure 4.4 **X-ray diffractograms of FTO/npCuO:npTiO$_2$ BHJ photoelectrodes with different npCuO:npTiO$_2$ ratios after thermal annealing at 600 °C. F, C$_x$, and T$_x$ indicate peaks corresponding to FTO, CuO, and TiO$_2$, respectively.**

4.3.3. UV-Vis Spectroscopy

The absorption spectrum of the films was calculated from the Kubelka-Munk function of the reflectance spectrum shown in Figure 4.5. The npCuO film had an absorption edge of approximately 850 nm and absorbed the entire visible spectrum (up to 350 nm), indicative of a small bandgap semiconductor. For BHJ electrodes with decreasing npCuO content, a similar characteristic spectrum was observed but with reduced intensity, indicating a decrease in light absorption because of the presence of a large bandgap (npTiO$_2$) semiconductor. TiO_2 only electrodes displayed absorption peaks at 340 nm, corresponding to the absorption of UV wavelength, and at 480 nm, which is determined to arise from the sample holder. When the backside of the sample was covered with black tape, the artifact disappeared. The direct bandgap value of the CuO photoelectrodes as calculated from the Tauc relation [f(hv)^2 vs. hv] was 1.36 eV

(Figure 4.5b), while that of TiO_2 was 3.15 eV, consistent with typically reported values in the literature.[303, 304]

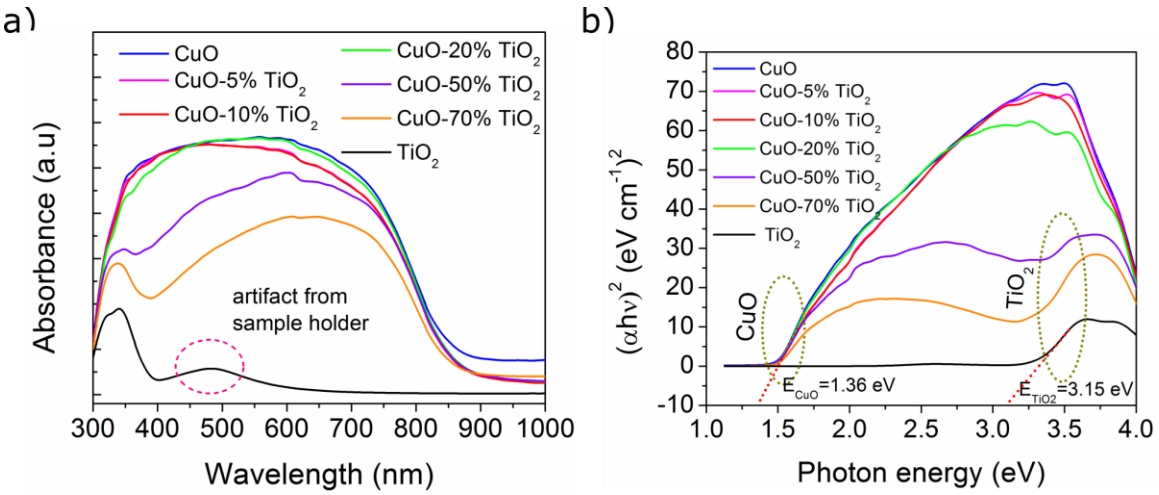

Figure 4.5 **(a) Kubelka-Munk (absorbance) transformation of the UV-Vis diffuse reflectance spectrum, and (b) Tauc plot for measuring the bandgap for FTO/npCuO:npTiO$_2$ BHJ photoelectrodes.**

4.3.4. Mott-Schottky Analysis

An electrode must display p-type characteristics to be used as a photocathode. Since BHJ electrodes contain both p-type CuO and n-type TiO_2, Mott-Schottky analysis was performed to determine the semiconducting nature of the photoelectrode. For FTO/npCuO photocathodes, a straight line with a negative slope (-2.78×10^{11} F^{-2} cm^4 V^{-1}) was observed, indicating p-type semiconducting behaviour (Figure 4.6a). The acceptor charge carrier density for FTO/npCuO was calculated to be 4.95×10^{19} cm^{-3}, similar to the values reported in the literature for CuO (~10^{19} cm^{-3}).[284, 305] When a small amount of npTiO$_2$ was introduced (5 wt%) to form the npCuO:npTiO$_2$ BHJ, Mott-Schottky plots revealed both negatively (-10.7×10^{11} F^{-2} cm^4 V^{-1}) and positively (5.96×10^{11} F^{-2} cm^4 V^{-1}) sloped lines, signifying the dual (p-type and n-type) semiconducting nature of the BHJ film. The p-type charge carrier density of npCuO:npTiO$_2$ BHJ photoelectrodes was calculated to be 1.2×10^{19} cm^{-3}, a four-fold decrease compared to that of the pure npCuO photoelectrodes. Reduced charge carrier densities diminish charge transport across the film and electron transfer at the electrode/electrolyte interface as it results in a narrower width of the depletion layer.[154] Meanwhile, the n-type behaviour of the film arises because of the presence of TiO_2. As the percentage of npTiO$_2$ in the film was increased from 5 wt% to 70 wt%, the p-type nature of the BHJ photocathode concomitantly decreased, and n-

type behaviour increased (Figure 4.6b). The electrode with pure npTiO$_2$ exhibited only a positively sloped line indicating pure n-type behaviour of the film.

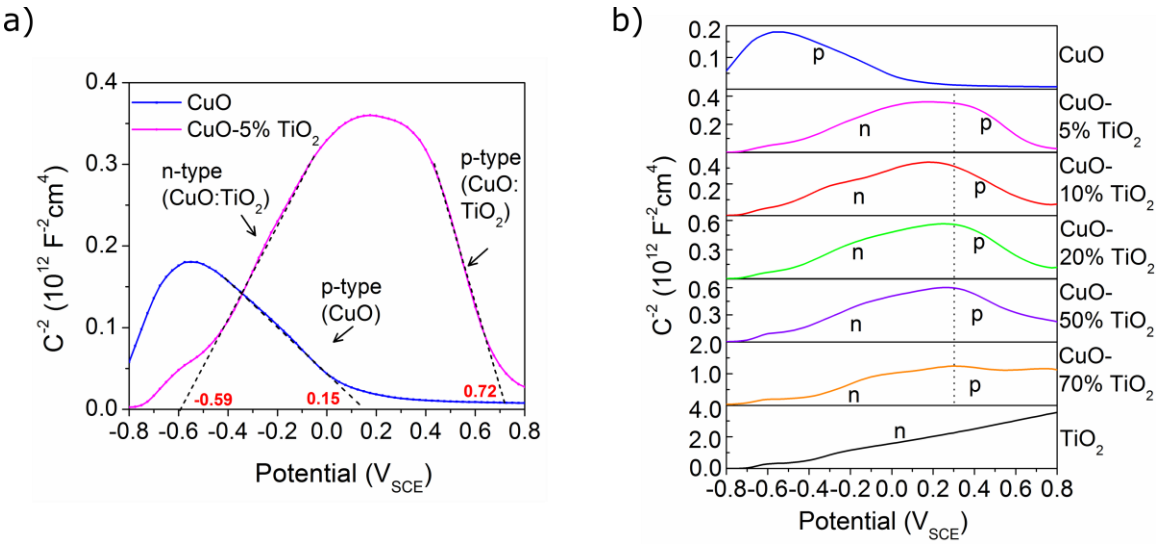

Figure 4.6 **Mott-Schottky plots of FTO/npCuO:npTiO$_2$ BHJ photocathode with varying wt% of npTiO$_2$. The measurements were carried out at 1 kHz AC applied frequency with an amplitude of 10 mV. The applied potential of the electrode was varied between 0.8 V and −0.8 V$_{SCE}$ in 0.5M Na$_2$SO$_4$ (pH 5.5) in 25 mV steps.**

4.3.5. Electrochemical Polarization Studies

Photoelectrodes are expected to generate high photocurrents and photopotential upon illumination. Open circuit potential (OCP) measurement under dark and illuminated conditions is a simple technique to assess the photopotential generated by a photoelectrode. The difference in OCP under dark and illuminated conditions provides an estimate of the photopotential (E_{ph}) that the electrode can generate.[306] OCP values of FTO/npCuO:npTiO$_2$ electrodes containing increasing content of npTiO$_2$ are shown in Figure 4.7. The increase in the OCP value of pure FTO/npCuO upon illumination is indicative of the p-type nature of the semiconductor. The photopotential was measured to be ~180 mV (Figure 4.7a). OCP values for FTO/npCuO:npTiO$_2$ BHJ photoelectrodes are shown in Figure 4.7 (b–e). For the BHJ electrodes containing 10 wt% and 20 wt% of TiO$_2$, the photopotential values decrease to 110 mV and 80 mV respectively. The decreased photopotential indicates a smaller number of excited electron generation in the depletion layer which can be ascribed to increased electrode resistance and decreased charge carrier density upon TiO$_2$ addition, as observed in the previous sections.

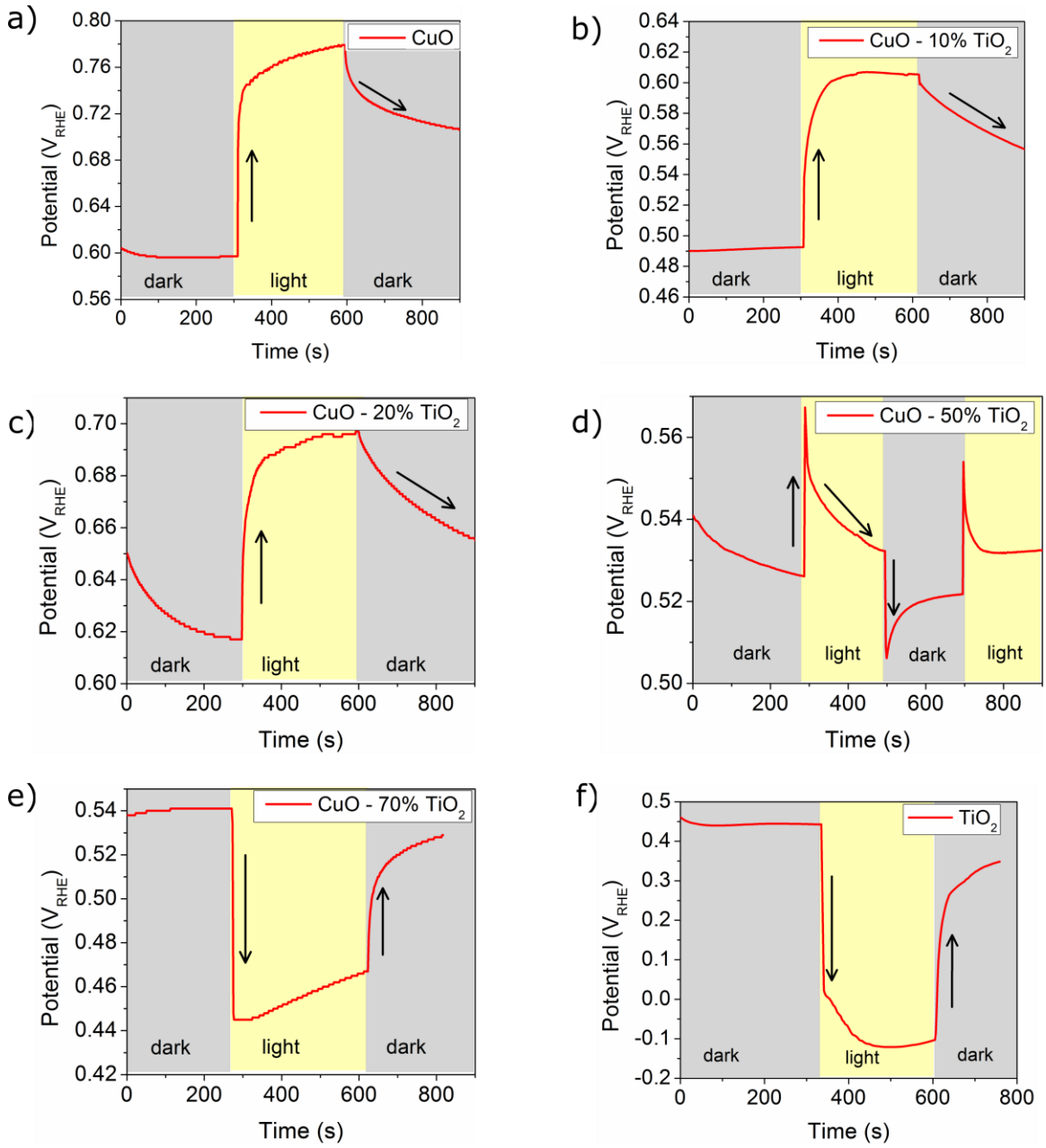

Figure 4.7 **Open circuit potential of FTO/npCuO:npTiO$_2$ BHJ photoelectrodes with different npCuO:npTiO$_2$ ratios after thermal annealing at 600 °C measured under light and dark conditions in 0.5M Na$_2$SO$_4$. (I=100 mW cm^{-2}, AM 1.5G). A positive shift in OCP upon illumination indicates the p-type nature of the photoelectrode; a negative shift indicates the n-type nature.**

For electrodes containing 50 wt% npTiO$_2$ (CuO-50%TiO$_2$), the increase in OCP values upon illumination was followed by a rapid decay in OCP, even though the electrode was kept under illumination. This indicates fast electron-hole recombination[63] and signifies that the addition of TiO$_2$ introduces recombination centers. It should be noted that a small

energy difference between the valence band of CuO and the conduction band of TiO_2 can render CuO/TiO_2 junctions potential recombination centers.[294] Although it might seem that recombination behaviour in OCP measurements does not appear in electrodes containing low quantities of TiO_2, this could also be attributed to a higher percentage of CuO in the film, which can overshadow the recombination characteristics. When the npTiO_2 content increased to above 50 wt%, the photoelectrode exhibited n-type behaviour and OCP shifted in a negative direction upon illumination. With a further increase in TiO_2 percentage, the n-type photopotential increased to higher values.

To further understand the photoelectrochemical behaviour of the photoelectrodes upon illumination, linear sweep voltammetry (LSV) was undertaken. The electrodes were illuminated with chopped AM 1.5G light at a 5 s interval. As the potential was scanned in a negative direction, the cathodic currents increased, as characteristic of a photocathode (Figure 4.8a), and the photocurrent onset potential was identified to be at 0.55 V_{RHE}. With a further increase in potential, the photocurrents gradually increased to a current density of -1.5 mA cm^{-2} at -0.56 V_{SCE} (0 V_{RHE}). Both photocurrent density and 'dark' current density are observed to increase with reduction potential. Although photoelectrodes are usually expected to be inert or display negligible photocurrents under 'dark' conditions, the observed -0.3 mA cm^{-2} current signifies electrochemical activity. The source of this current is speculative and may either be due to hydrogen evolution or photocorrosion.

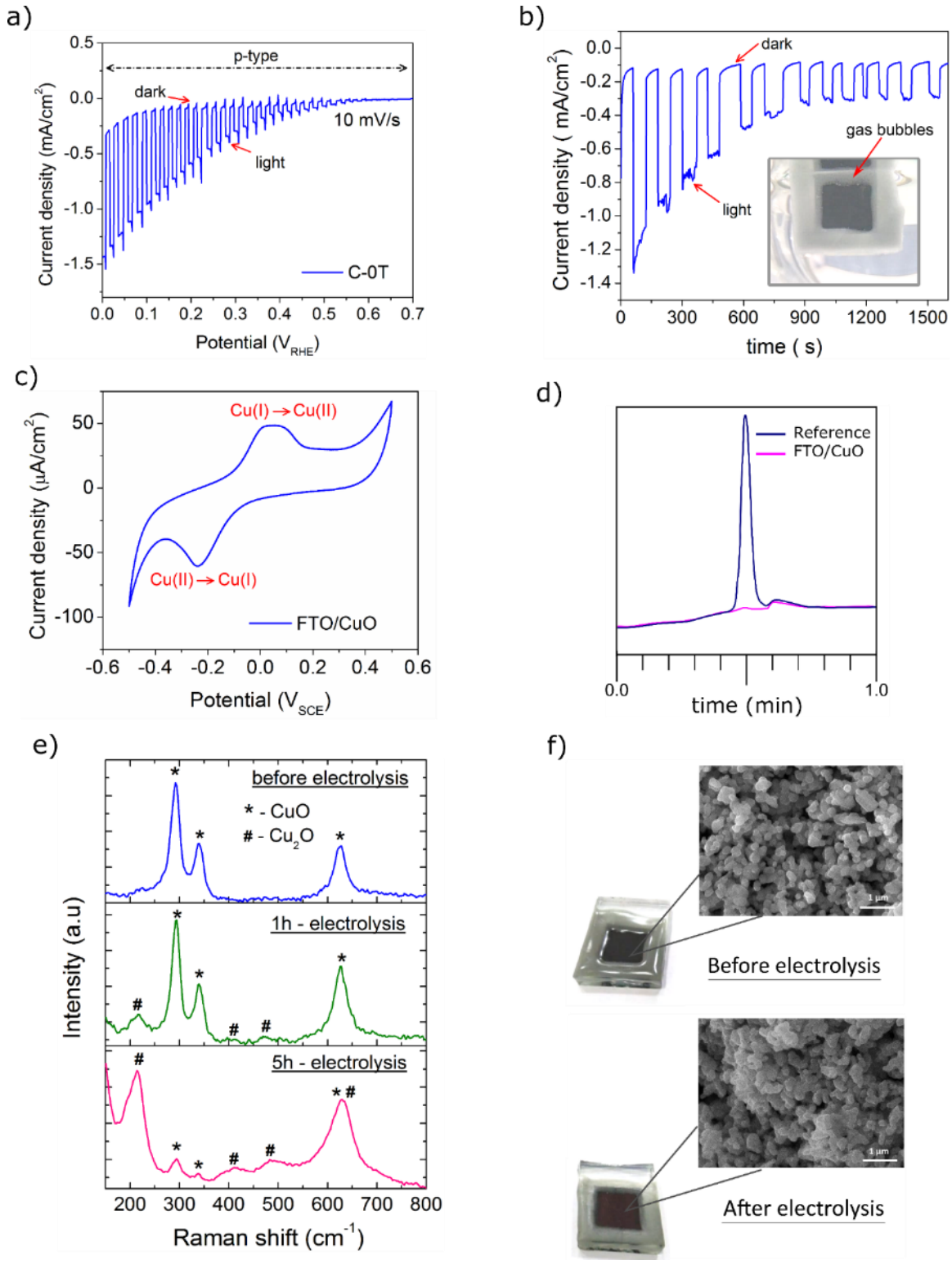
a)
p-type
dark
light
10 mV/s
C-0T
Current density (mA/cm²)
Potential (V_RHE)
b)
dark
light
gas bubbles
Current density (mA/cm²)
time (s)
c)
Cu(I) → Cu(II)
Cu(II) → Cu(I)
FTO/CuO
Current density (μA/cm²)
Potential (V_SCE)
d)
Reference
FTO/CuO
time (min)
e)
before electrolysis
* - CuO
# - Cu2O
1h - electrolysis
5h - electrolysis
Intensity (a.u)
Raman shift (cm⁻¹)
f)
Before electrolysis
After electrolysis

Figure 4.8 **(a) Linear sweep voltammetry, (b) photoelectrolysis at 0 V_{RHE}, (c) cyclic voltammetry of FTO/npCuO electrode with alternating dark and light cycles measured in 0.5M Na_2SO_4. (pH 5.5, intensity=100 mW cm^{-2}, AM 1.5G). inset: A photograph of the electrode during electrolysis shows gas bubbles at the edges. (d) H_2 gas chromatograph of the sample gas collected during photoelectrolysis, along with reference H_2 obtained by electrolysis in 0.5M Na_2SO_4 (pH 5.5) at Pt working and counter electrodes by applying −0.1 V_{RHE} for 15 minutes. (e) Raman spectroscopic analysis, and (f) Photograph and SEM micrograph of the electrode before and after an hour of electrolysis indicating the presence of Cu_2O.**

For CuO, the increase in 'dark' current is associated with the photodegradation of CuO, signalling the unstable nature of the electrode.[275] Chronoamperometry measurements were carried out at a constant potential (0 V_{RHE}) with alternating dark and light cycles for a prolonged duration to learn about the stability of the electrode, as CuO is known to undergo photo corrosion information. Photocurrents corresponding to the pure npCuO photoelectrode decreased from 1.2 mA cm^{-2} to 0.3 mA cm^{-2} within 15 minutes of illumination (Figure 4.8b), retaining only 25% of the initial photocurrents. The decrease is speculated as being due to an increase in physical shielding of active electrochemical sites by corrosion products or a decrease in the light absorbed by the electrode as the concentration of the photoactive material in the film decreases. For instance, one of the degradation pathways for CuO is conversion to Cu_2O (Equation 4.4), which leaves the CuO electrode surface covered with Cu_2O. Although Cu_2O is photoactive (bandgap is ~2.1 eV), electron transfer from CuO to electrolyte via Cu_2O is impeded by the high position of its conduction band, as illustrated in Figure 4.9, thereby resulting in decreased electrode performance. Photoconversion of CuO to Cu (Equation 4.3), on the other hand, renders the electrode inactive as Cu is not a semiconductor.

Cyclic voltammetry of the pure FTO/npCuO electrode measured in the potential range revealed a reduction peak at −0.23 V_{SCE} (Figure 4.8c), which is attributed to the conversion of Cu^{2+} to Cu^{+}. This reaction will compete with the HER (−0.56 V (0 V_{RHE})). Thus, although minor gas evolution was observed at the edges of the electrode (possibly H_2 but not confirmed) (Figure 4.8d), the quantity of which was below the minimum detectable limit of the GC instrument. After an hour of electrolysis, the colour of the electrode changed from black to dark red indicating Cu_2O formation (Figure 4.8f). However, SEM analysis of the electrode revealed no change in shape or morphology of the NPs (Figure 4.8f). Raman spectroscopic analyses of the photoelectrode before and

after electrolysis are shown in Figure 4.8e. Three Raman active vibrational modes are observed for CuO electrodes before electrolysis. The peak corresponding to 298 cm^{-1} is attributed to the A_{1g} mode. B_{1g} and B_{2g} modes were observed at 344 cm^{-1} and 632 cm^{-1} respectively. Raman analysis after electrolysis indicated the presence of Cu_2O (210, 405, 483, and 638 cm^{-1}) along with characteristic peaks of CuO. The Cu_2O peak intensity was observed to increase with electrolysis time.

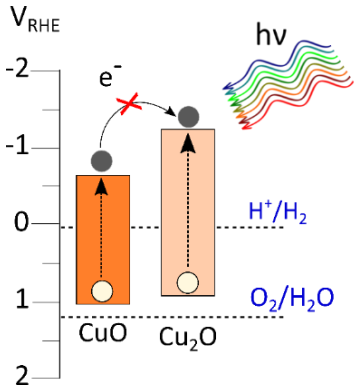

Figure 4.9 **Schematic depicting charge transfer between CuO photoelectrode and Cu_2O formed as a result of photodegradation on the surface of the former. The misaligned conduction band energy levels prevent efficient charge transfer from CuO to the electrolyte.**

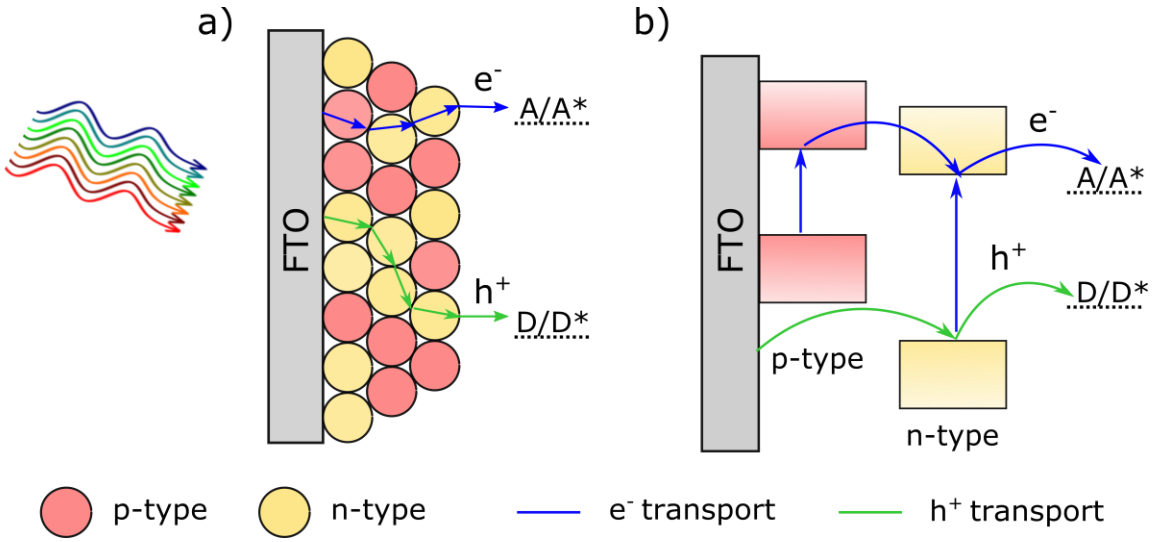

Figure 4.10 **(a and b) Schematic depicting electron transfer (blue) and hole transfer (green) pathways that give rise to photocathodic and photoanodic currents, respectively, upon illumination in type-II p-n BHJ electrodes. As hole transfer from p-type to n-type cannot occur due to improper band alignment, in BHJ electrodes exhibiting dual photocurrents, photoanodic currents arise solely from the n-type semiconductor, while photocathodic currents comprise of electrons from both p-type and n-type semiconductors.**

A linear sweep photoelectrolysis of the BHJ electrode with 5 wt% npTiO$_2$ (CuO - 5% TiO$_2$) yielded a photocurrent of −0.15 mA cm^{-2} at −0.56 V_{SCE} (0 V_{RHE}), which is significantly smaller than that obtained using pure npCuO (−1.2 mA cm^{-2}) electrode (Figure 4.11). This is attributed to a significant reduction in exposed CuO in BHJ electrodes as a large fraction of photocurrent is due to photocorrosion of CuO, as observed previously (Figure 4.8). Further increase in the npTiO$_2$ content from 5 wt% to 70 wt% reduced the photocurrent from the milliampere to the microampere range. Although a decrease in photocathodic current with increasing TiO$_2$ percentage in the film was observed, a simultaneous increase in photoanodic currents signifies that the electrode displays dual-semiconducting behaviour, as confirmed by the Mott-Schottky analysis. The alternating p-type and n-type behaviour upon perturbance by an external stimulus (light or electric potential) is known as a photoelectrochemical photocurrent switching (PEPS) effect, which can be utilized to design molecule-based logic devices.[307-310] Charge transport pathways for the case of p-type and n-type semiconductors in BHJ architecture having type-II bandgap alignment are shown in Figure 4.10. As it is not the intent of this thesis to explore this topic, subsequent experiments will only focus on the photocathodic behaviour of the electrodes.

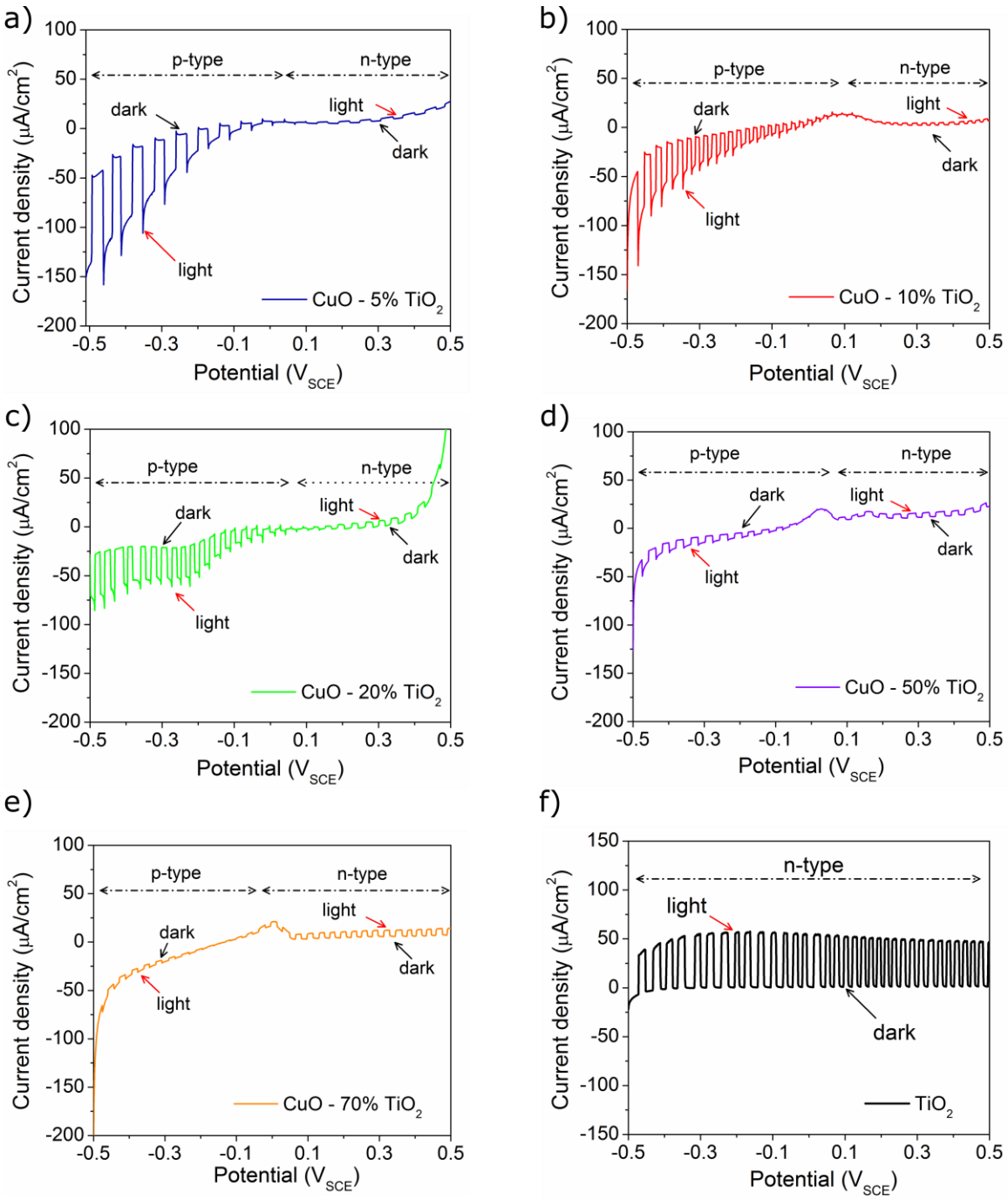

Figure 4.11 **Linear sweep voltammetry (LSV) measurements of FTO/npCuO:npTiO$_2$ BHJ photoelectrodes with different npCuO:npTiO$_2$ ratios measured in 0.5M Na$_2$SO$_4$. (pH 5.5, intensity=100 mW cm^{-2}, AM 1.5G). LSV measurements were carried out under chopped light with illumination intervals of 5 s at the scan rate of 10 mV s^{-1}.**

4.3.6. Impedance Spectroscopy Analysis

Although the band edges of CuO and TiO_2 semiconductors form type-II heterojunction, the BHJ electrodes displayed poor photocurrent response as seen in the previous section. To probe further, electrochemical impedance spectroscopy measurements of the photoelectrode were undertaken to examine the resistance offered by the BHJ electrode for charge transfer within the electrode and across the electrode/electrolyte interface. Impedance spectra were obtained at an applied potential of −0.24 V_{SCE} so that the electrode exhibits cathodic behaviour. The Nyquist plots reveal a partial section of a large-diameter semi-circle, representing high charge-transfer resistance (R_{ct}) at the electrode/electrolyte interface (Figure 4.13 & Figure 4.14). As the TiO_2 mass fraction increased from 5% to 70%, the diameter of the semi-circle increased, indicating higher resistance. Impedance spectra were further deconvoluted by fitting with an appropriate equivalent electrical circuit to assess the underlying physical parameters. An equivalent circuit for a bulk-heterojunction electrode immersed in an electrolyte under the dark can ideally be represented using the electrical circuit given in Figure 4.12 (adapted from the transmission line model used to describe organic BHJ solar cells).[311]

To represent the impedance spectrum with an appropriate equivalent circuit, it is necessary to understand the nature of the electrode that gives rise to each electrical element. The equivalent circuit of a p-n junction can be represented by a circuit containing a resistor and capacitor in parallel. As BHJs is a three-dimensional network of p-n junctions formed at the donor-acceptor NP interface, it gives rise to a series of resistor-capacitor circuits, as shown in Figure 4.12. The resistance encountered by the electron to move across the film is represented by charge transport resistance ($R_{transport}$) and the global capacitance arising from the dielectric nature of the film as C_{film}. As the BHJ electrodes have two dissimilar NPs (CuO and TiO_2) exposed to the electrolyte, each gives rise to one R–C circuit at the electrode/electrolyte interface due to double-layer formation. The resistance offered by the electrolyte and FTO substrate is represented by R_s and R_{FTO}, respectively.

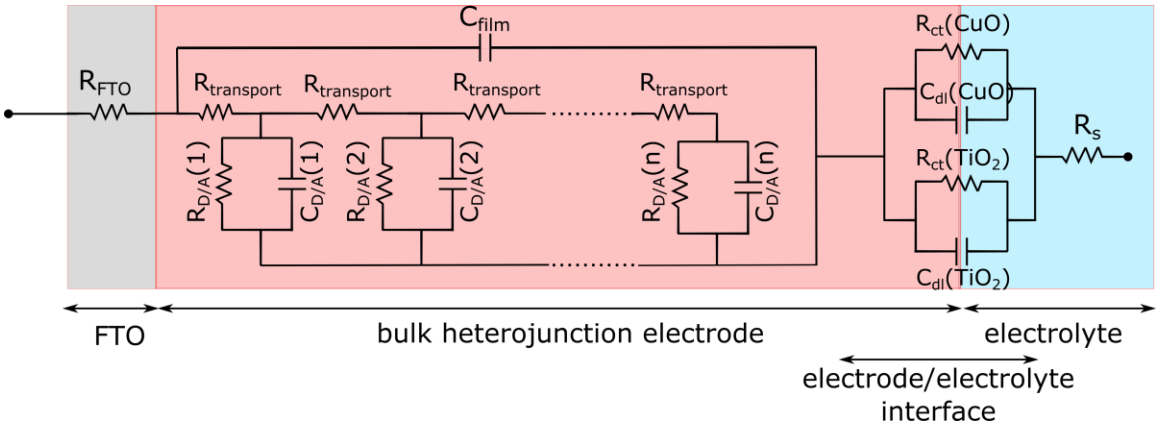

Figure 4.12 Equivalent electrical circuit of a bulk-heterojunction photoelectrode in contact with an electrolyte under dark.

Owing to the inherent complexity in fitting the impedance spectra with this circuit, a simplified model consisting of two parallelly connected resistor and capacitor elements, each representing electrode (R_{film}–CPE(2)) and electrode/electrolyte ($R_{interface}$–CPE(1)) interface, in series with solution resistance (R_s) and an inductor (L_{film}, arising from porous nature of the film) is used (as shown in Figure 4.13)[312]. Note that capacitors are replaced with the constant phase element to account for the non-ideal behaviour of capacitors as the center of the semicircle does not lie on the axis, that is, the phase angle of the capacitor is less than 90°. The equivalent circuit fits impedance spectra well (Figure 4.13 and Figure 4.14), and the fitting parameters are listed in Table 4.1. Both charge transfer resistance ($R_{interface}$) and film resistance (R_{film}) doubled with just 5 wt% addition of TiO_2. Further addition of TiO_2 increased the resistance to even higher values, affecting both charge transport within the electrode and charge transfer at the film/electrolyte interface. The resistance values will decrease if there exists an efficient charge transfer between CuO and TiO_2.[143]

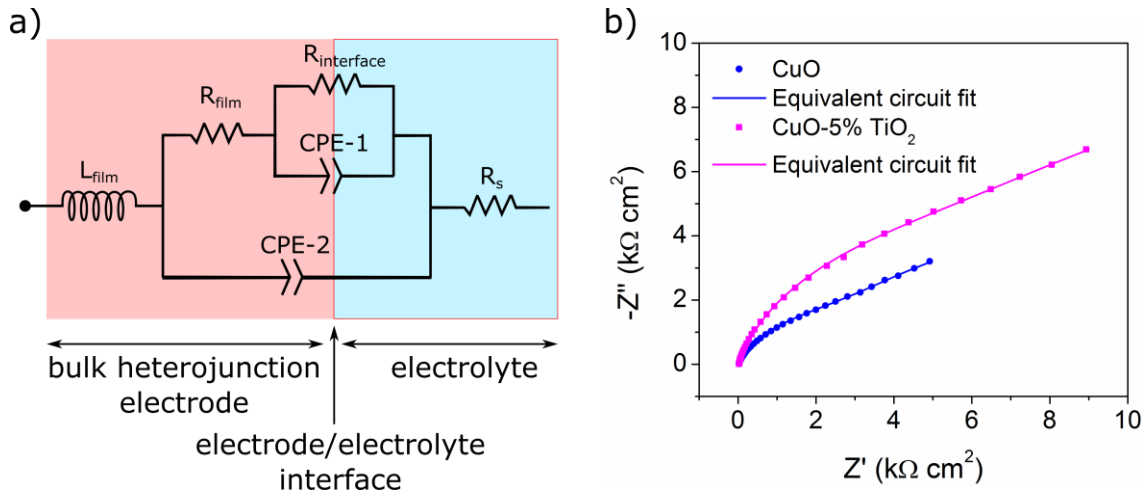

Figure 4.13 **(a) Equivalent electrical circuit model used to fit (b) EIS Nyquist plot of FTO/npCuO:npTiO$_2$ BHJ photocathodes with 0% and 5% npTiO$_2$ content. The measurements were carried out at the applied potential of −0.24 V$_{SCE}$ in 0.5M Na$_2$SO$_4$ (pH 5.5) in a three-electrode configuration.**

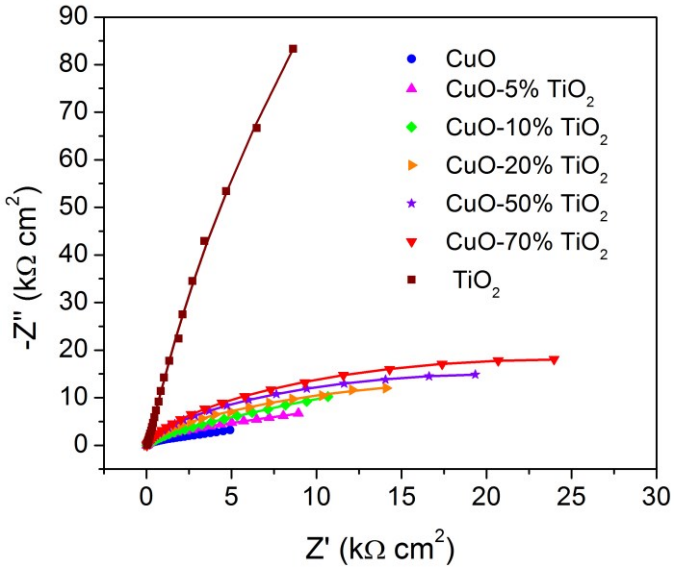

Figure 4.14 **EIS Nyquist plot of FTO/npCuO:npTiO$_2$ BHJ photocathodes with varying npTiO$_2$ content (0, 5, 10, 20, 50, 70, and 100 wt% TiO$_2$). The measurements were carried out at the applied potential of −0.24 V$_{SCE}$ in 0.5M Na$_2$SO$_4$ (pH 5.5) in a three-electrode configuration. (symbols represent experimental data, and lines represent equivalent circuit fit).**

Table 4.1. **Electrical parameters extracted from the impedance spectra by fitting with an equivalent circuit.**

	R_s (Ω)	$R_{interface}$ (Ω)	R_{film} (Ω)	CPE-1 ($\Omega^{-1}s^{\alpha}cm^{-2}$)	α_1	CPE-2 ($\Omega^{-1}s^{\alpha}cm^{-2}$)	α_2	L (x10^5 H)
CuO	11.18	1.01 x10^4	4.42 x10^3	5.44 x10^{-5}	0.711	1.32 x10^{-5}	0.732	-1.02
CuO-5% TiO_2	14.38	2.16 x10^4	9.18 x10^3	3.19 x10^{-5}	0.721	6.81 x10^{-6}	0.828	-1.50
CuO-10% TiO_2	14.53	2.19 x10^4	1.35 x10^4	1.16 x10^{-5}	0.879	7.38 x10^{-6}	0.796	-1.78
CuO-20% TiO_2	21.37	2.44 x10^4	1.39 x10^4	1.28 x10^{-5}	0.741	4.45 x10^{-6}	0.899	-2.31
CuO-50% TiO_2	29.64	2.26 x10^4	1.78 x10^4	8.56 x10^{-6}	0.700	3.47 x10^{-6}	0.916	-1.67
CuO-70% TiO_2	35.30	2.59 x10^4	2.18 x10^4	6.22 x10^{-6}	0.721	2.84 x10^{-6}	0.916	-2.17
TiO_2	44.04	1.73 x10^6	1.14 x10^5	1.16 x10^{-7}	0.902	1.92 x10^{-6}	0.968	-2.48

4.3.7. Homogeneously Distributed BHJ Nanoparticles

The reduced photocurrent density and high resistance of the CuO-TiO_2 NP BHJ devices can be ascribed to the non-homogeneous (agglomerated) distribution of donor and acceptor NPs as particle distributions play an essential role in randomly distributed BHJ electrodes. For example, a schematic of the ideal and non-ideal distribution of donor and acceptor NPs is depicted in Figure 4.15. Agglomerated (isolated) regions of either donor or acceptor particles will function as charge traps causing fast recombination of excitons as no continuous charge transport pathways are available.

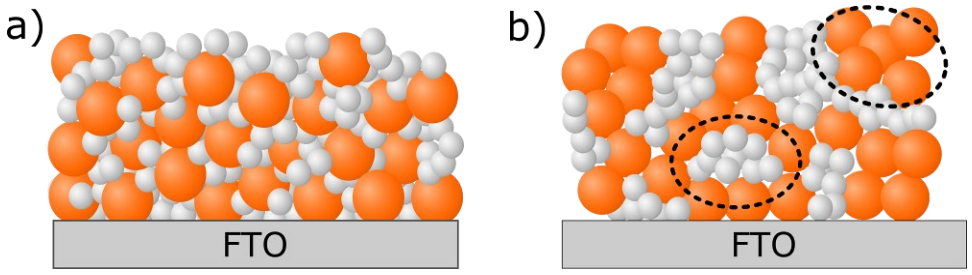

Figure 4.15 **Schematics of randomly distributed np-donor (CuO, orange):np-acceptor (TiO_2, white) configuration, (a) ideal arrangements for efficient charge extraction and transportation; (b) sample distribution of agglomerated NPs in which circled areas act as charge traps.**

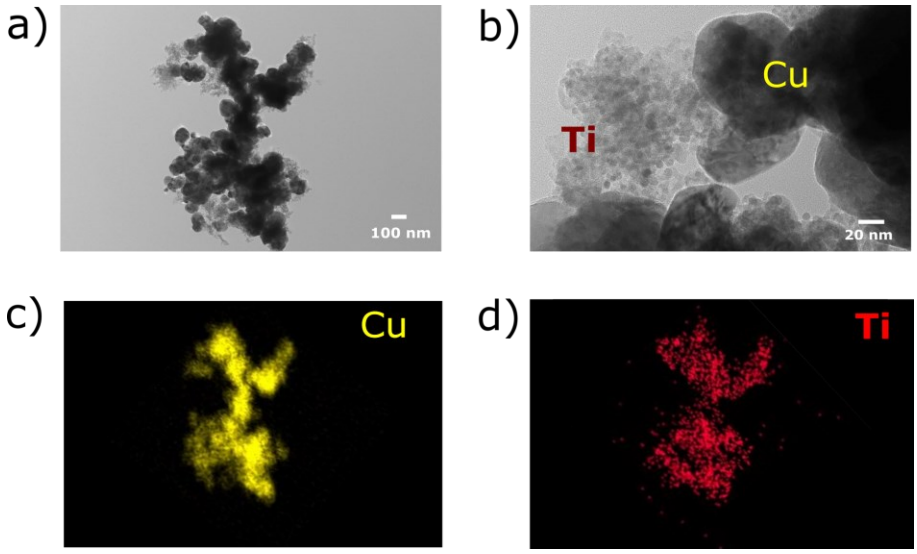

Figure 4.16 Transmission electron image of homogeneously distributed npCuO:npTiO$_2$ (a and b) synthesized via co-precipitation method along with Cu and Ti elemental distribution (c and d).

Attempts to obtain a homogeneous distribution of CuO and TiO_2 NPs – as depicted in Figure 4.15a – by mechanical mixing of commercial NPs were not fruitful. Even long-term magnetic stirring and ultrasonication of the NP mix did not yield a homogeneous blend. Hence, uniformly distributed BHJ electrodes were synthesized using the co-precipitation method (cp-(npCuO:npTiO$_2$)) from a 1:1 molar ratio of copper nitrate and titanium chloride solutions. The precipitants ($Cu(OH)_2$ and $Ti(OH)_4$) were filtered and annealed at 400 °C to obtain CuO and TiO_2 NPs (as confirmed by Raman spectroscopy (Figure 4.17)). Transmission electron microscopy analysis revealed uniformly distributed CuO and TiO_2 NPs with particle sizes of ~50 nm and ~10 nm respectively (Figure 4.16).

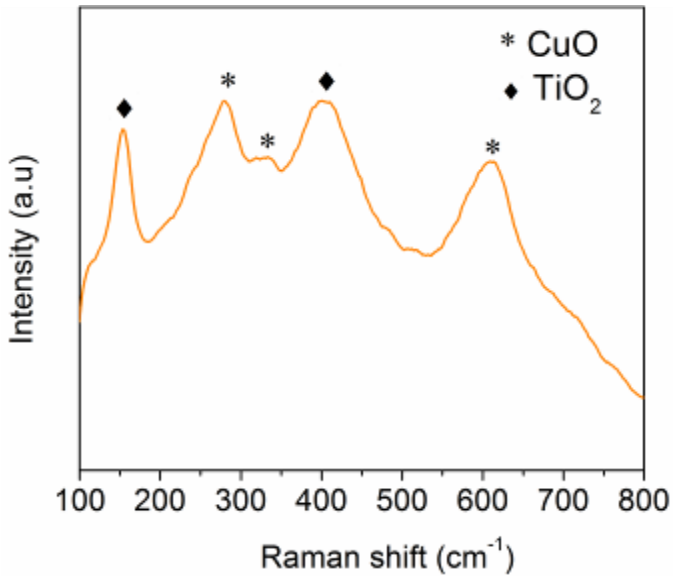

Figure 4.17 Raman active vibrational modes of npCuO:npTiO$_2$ bulk-heterojunction NPs. CuO vibrational modes (298 cm^{-1}, 344 cm^{-1} and 632 cm^{-1}) and TiO$_2$ vibrational modes (145 cm^{-1} and 396 cm^{-1}) are depicted.

The NPs were deposited on the FTO substrate and then annealed at 600 °C for electrode preparation. SEM analysis of the electrode revealed a particle size of ~130 nm for CuO. During particle growth, as CuO NPs fuse to become larger NPs, it is reasonable to assume that the final electrode may contain nanostructures depicted by a mixture represented in Figure 2.11b and Figure 2.11c. The electrode also exhibits dual-semiconducting behaviour similar to non-homogeneous electrodes. Cyclic voltammetry analysis revealed Cu(II)/Cu(I) reduction peaks, signifying exposed CuO to the electrolyte (Figure 4.18a). However, the peak current density is much less than that of a pure CuO electrode (Figure 4.8c). This implies a lower rate of the redox reaction for CuO and hence improved stability of the prepared electrode. The photoelectrochemical performance of FTO/cp-(npCuO:npTiO$_2$) photoelectrodes is indicated in Figure 4.18b–d. OCP measurement of FTO/cp-(npCuO:npTiO$_2$) under dark and illuminated conditions displayed a photopotential of 100 mV compared to 150 mV observed for FTO/npCuO electrode. This is similar to the observation before that the addition of TiO$_2$ reduces photopotential. LSV measured photocurrent (~0.17 mA cm^{-2} at 0 V_{RHE}) of cp-(npCuO:npTiO$_2$) (Figure 4.18c) is much lower than that of the npCuO (~1.5 mA cm^{-2} at 0 $V_{RHE,}$). This can be ascribed to the increase in film resistance and decrease in carrier concentration upon introducing TiO$_2$, as discussed in the preceding sections. On the other hand, the electrode stability considerably improved during photoelectrolysis because of the presence of TiO$_2$ on the

surface of BHJ electrodes (Figure 4.18d). The electrode retained 77% of the initial photocurrent compared to 25% of the FTO/npCuO electrode. However, no hydrogen gas evolution was observed, highlighting the need for a hydrogen evolution reaction catalyst.

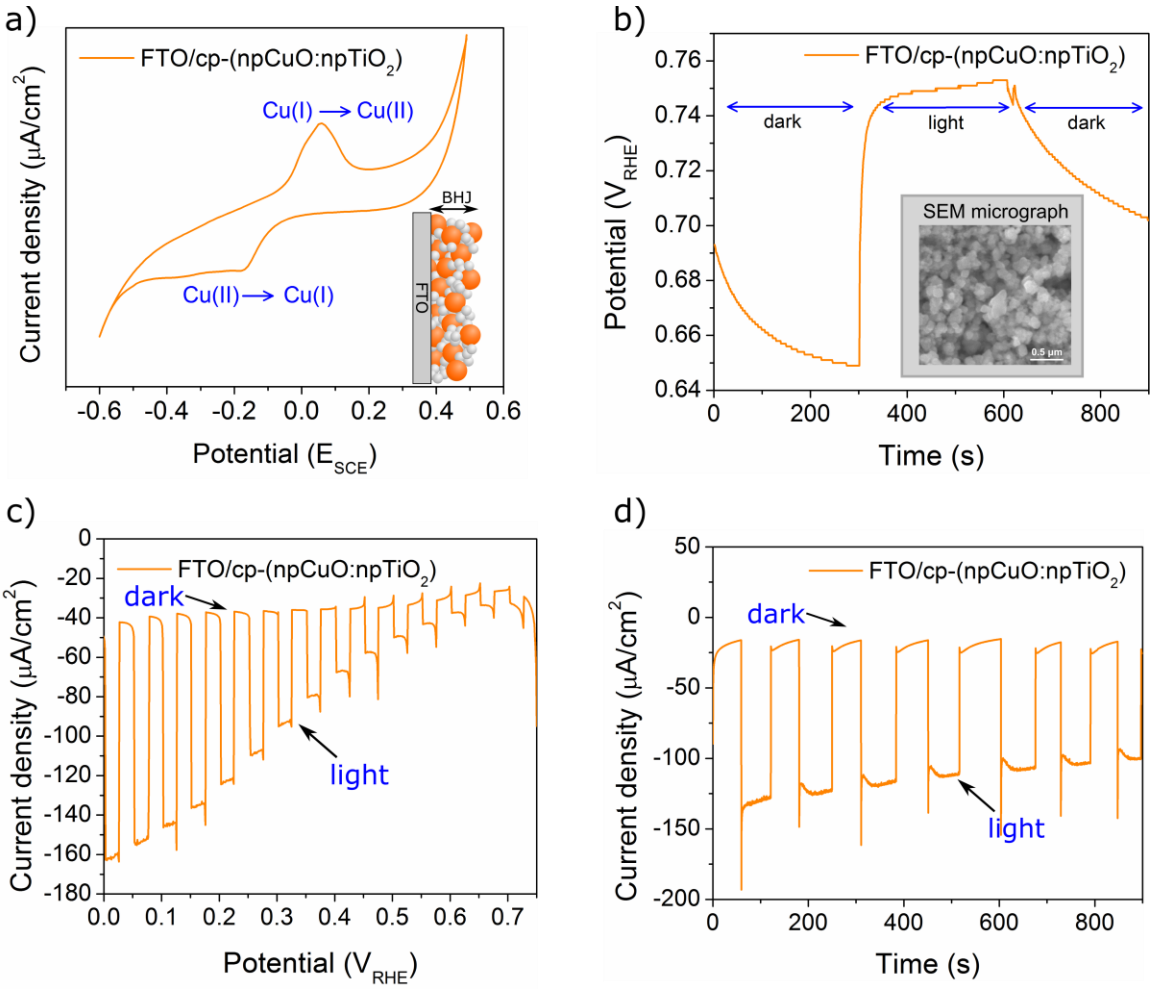

Figure 4.18 (a) Open circuit potential, (b) cyclic voltammogram of cp-(npCuO:npTiO$_2$) BHJ electrode, (c) linear sweep voltammetry, and (d) photoelectrolysis (at 0 V_{RHE}) of cp-(npCuO:npTiO$_2$) BHJ photoelectrodes measured under light and dark conditions in 0.5M Na_2SO_4. (I=100 mW cm^{-2}, AM 1.5G).

4.3.8. Catalyst Modified Photoelectrodes

In the previous sections, it is ascertained that CuO undergoes photodegradation instead of hydrogen evolution. Photodegradation (photocorrosion) of CuO occurs via the electrochemical reactions shown in Equations 4.2–4.4. In the research literature, two methods are widely discussed to address the photocorrosion of the electrodes. One method employs a protective layer conformally on top of the electrodes, eliminating direct

contact between reactant species (CuO, $H^{+,}$ and e^{-}), thereby preventing photocorrosion (Figure 4.19a). The other route is to employ highly conducting, stable catalysts that serve as an electron shuttle to the solution species. However, this purely kinetic approach often does not prevent photocorrosion entirely, and in the present system, CuO reduction still occurs at the exposed surface, albeit at a decreased rate.

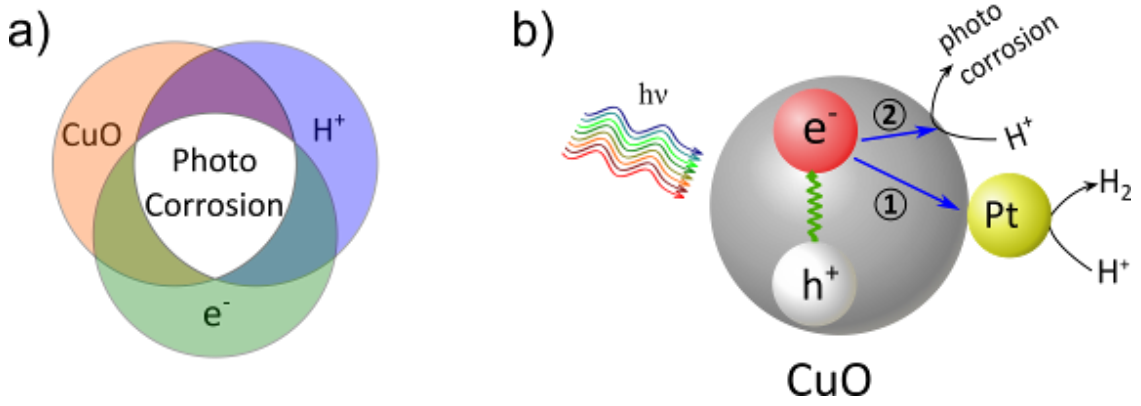

Figure 4.19 Schematic depicting (a) reactants involved in CuO photodegradation, and (b) photodegradation of CuO in the presence of Pt catalyst which enhances the stability of the electrodes.

In previous reports, to increase both stability and electrode kinetics towards water splitting, catalyst particles were employed (Figure 4.19b). [296, 313, 314] Here, Pt is chosen for its good catalytic activity towards the HER and is electrodeposited on top of BHJ photoelectrodes (FTO/cp-(npCuO:npTiO$_2$) following the procedure described in the experimental methods.[299] A typical SEM micrograph of photoelectrode after Pt deposition is shown in Figure 4.20b, depicting Pt covered cp-(npCuO:npTiO$_2$) BHJ NPs. The particle size of Pt is measured to be ~60 nm. Unfortunately, the presence of redox peaks in cyclic voltammetry measurements indicates exposed CuO to the electrolyte arising from the non-platinum-deposited region of CuO. After Pt deposition, the cyclic voltammogram revealed two reduction peaks: the Cu(II)/Cu(I) peak at −0.08 V_{SCE} followed by the Cu(I)/Cu(0) peak at −0.31 V_{SCE}.[315] The two reduction peaks were observed only after Pt electrodeposition, and hence it is presumed that during Pt deposition in an acidic electrolyte (1 mM H_2PtCl_6), CuO also undergoes reduction to either Cu_2O or Cu. Furthermore, the photopotential value calculated from the difference between OCP values in the dark and under illumination is very low (~5 mV). The lesser photopotential further ascertains that CuO undergoes surface degradation during Pt electrodeposition and the electrode becomes less photoactive. LSV and electrolysis measurements revealed significant dark currents

indicating the unstable nature of Pt-deposited FTO/cp-(npCuO:npTiO$_2$)/Pt BHJ electrodes (Figure 4.20 e&f) and the electrode lost 50% of the initial photocurrents in 15 minutes.

Thus, a solution-based approach was chosen to protect the electrode both at the surface and subsurface regions from the electrolyte during Pt electrodeposition and photoelectrolysis. A thin TiO_2 (50 nm) was deposited on top of BHJ electrodes by thermal conversion (at 400 °C) of the spin-coated titanium tetraisopropoxide (TTIP) layer, which resulted in a ~50 nm thick TiO_2 film. After applying the protective TiO_2 coating, the Cu redox peaks could not be observed by cyclic voltammetry (Figure 4.20c), confirming the protective nature of TiO_2 film in mitigating the exposure of the underlying CuO. Photoelectrochemical analysis of FTO/cp-(npCuO:npTiO$_2$)/TiO$_2$/Pt is shown in Figure 4.20 e&f. The TiO_2 and Pt protected cp-(npCuO:npTiO$_2$) BHJ photoelectrode exhibited photocurrents of 0.2 mA cm^{-2}. Although the photocurrent onset potential (0.5 V_{RHE}) is less than the FTO/cp-(npCuO:npTiO$_2$) electrode after TiO_2 and Pt deposition, the BHJ electrode displayed good stability and retained 90% of the initial photocurrents. GC analysis of the gas collected from the headspace of the photoelectrochemical cell was carried out to identify the liberated gas. From the elution trace of the chromatographs, it was identified to be hydrogen (Figure 4.21), and from the Coulombic charges passed, the quantity of hydrogen liberated was calculated to be ~0.05 μmol hr^{-1} cm^{-2}, with Faradaic efficiency less than 30%.

Despite the initial improved stability of the FTO/cp-(npCuO:npTiO$_2$)/TiO$_2$/Pt electrode, long-term photoelectrolysis revealed that the photocurrent decreases with time, as shown in Figure 4.22. The diminishing stability combined with low Faradaic efficiency suggests the occurrence of alternate redox reactions other than hydrogen evolution despite the presence of protective and catalyst layers. Paracchino et al., in their seminal work on Cu_2O photoelectrodes involving atomic layer deposited Al:ZnO and TiO_2 overlayers observed a similar decrease in electrode stability which they have shown to be the reduction of TiO_2 to $Ti(OH)_3$.[193, 299] Although TiO_2 is a widely reported protective layer for inorganic photocathodes, there remains significant unanswered questions regarding the electron transfer from photoelectrodes, particularly CuO or Cu_2O to TiO_2. However, this warrants a separate study as it shifts the current work from its intended scope to understand the feasibility of BHJ architectures in inorganic electrodes.

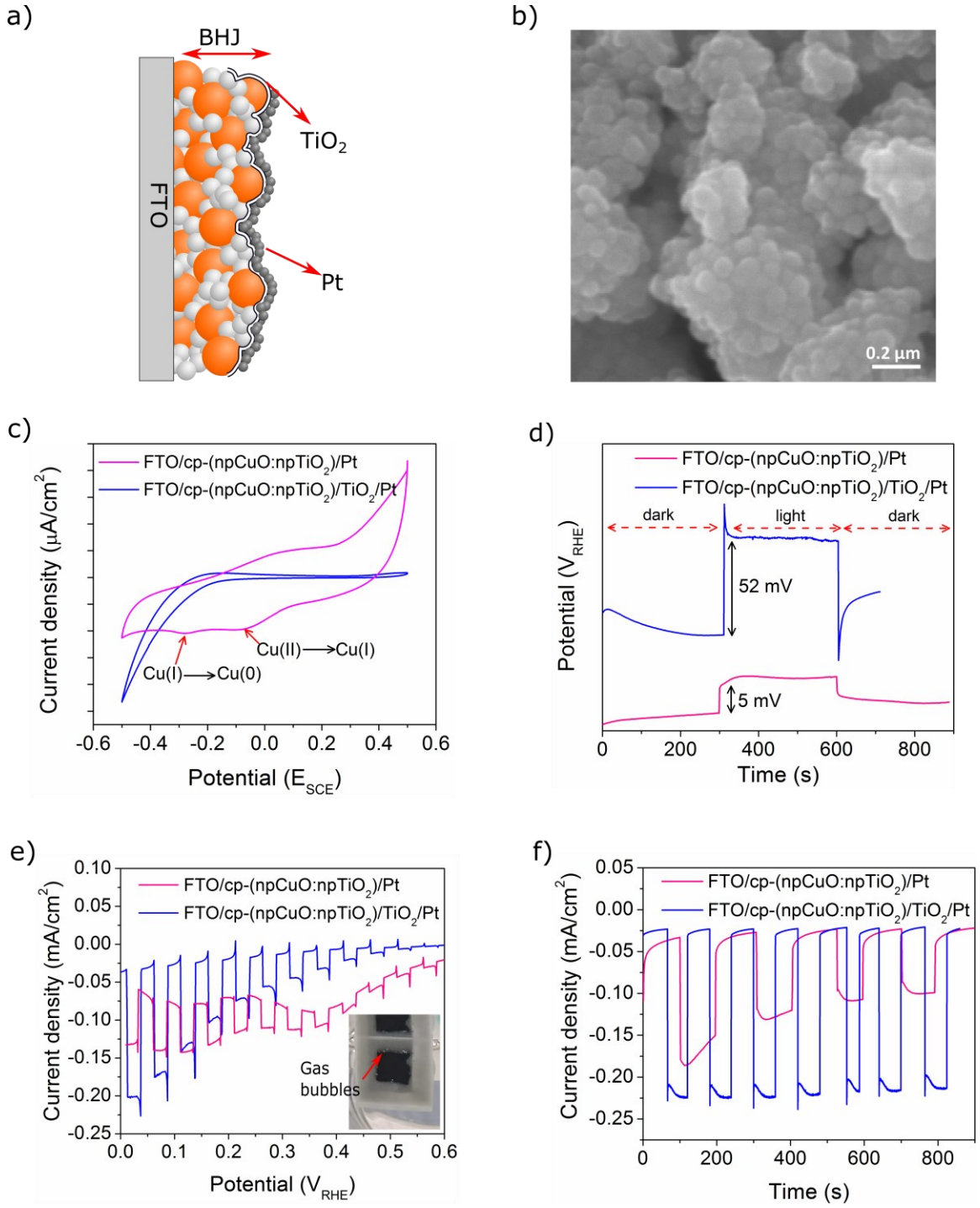

Figure 4.20 **(a) Schematic and (b) SEM micrograph (only Pt NPs are visible) of cp-(npCuO:npTiO$_2$)/TiO$_2$/Pt photoelectrode; (c) cyclic voltammogram, (d) open circuit potential, (e) linear sweep voltammetry and (f) photoelectrolysis (at 0 V$_{RHE}$) of cp-(npCuO:npTiO$_2$)/Pt BHJ photoelectrodes without and with TiO$_2$ protective layer measured under light and dark conditions in 0.5M Na$_2$SO$_4$. (I=100 mW cm^{-2}, AM 1.5G). inset: Photograph of electrode during photoelectrolysis depicting H$_2$ evolution.**

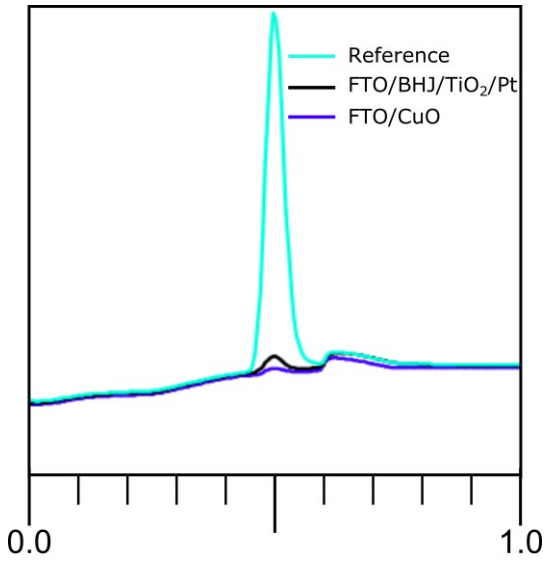

Figure 4.21 **Gas Chromatograph of liberated gases during photoelectrolysis of FTO/cp-(npCuO:npTiO$_2$)/TiO$_2$/Pt electrode for an hour at 0 V$_{RHE}$ in 0.5M Na$_2$SO$_4$. (pH-5.5, I=100 mW cm^{-2}, AM 1.5G) (black). Reference H$_2$ was obtained by electrolysis (−0.1 V$_{RHE}$, 15 minutes) of Pt working and counter electrodes immersed in 0.5M Na$_2$SO$_4$ (cyan). GC spectrum of FTO/CuO electrode is depicted for comparison (blue).**

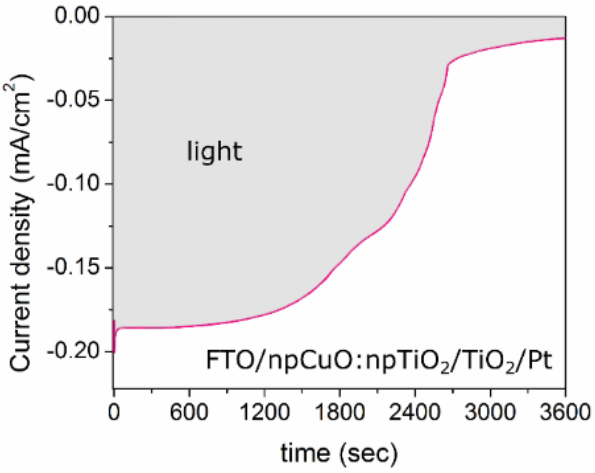

Figure 4.22 **Photoelectrolysis (at 0 V$_{RHE}$) of cp-(npCuO:npTiO$_2$)/TiO$_2$/Pt BHJ carried out for one hour under AM1.5G (I=100 mW cm^{-2}) illumination in 0.5M Na$_2$SO$_4$. (pH 5.5). Reference electrode: SCE. Counter electrode: Pt.**

4.4. Conclusion

Photoelectrochemical behaviour of randomly distributed CuO (donor) and TiO_2 (acceptor) nanoparticle-based p-n BHJ architecture was extensively explored towards highly efficient photoelectrodes for potential hydrogen generation. The hypothesis that BHJ architecture will aid CuO-based photocathodes to attain higher photocurrents than the typically reported ~2 mA cm^{-2} by efficient charge extraction and transportation is tested, and the results revealed that:

- Unprotected CuO photoelectrodes undergo photocorrosion instead of promoting H_2 evolution.
- BHJ electrodes display dual-semiconducting behaviour (p-type and n-type).
- In the presence of acceptor NPs (TiO_2), stability of the BHJ electrode increases, but photocurrents decrease because of increased electrode resistance and electron-hole recombination.
- A TiO_2 (protective layer) and Pt (protective and catalyst layer) covered npCuO:npTiO$_2$ BHJ electrodes exhibited H_2 evolution, albeit with a very low faradaic efficiency (<30%).

The observed low Faradaic efficiency indicates that not all photocurrent arises from the hydrogen evolution reaction despite the presence of a protective layer and catalyst. There exists an inconclusiveness in the literature over the active component for H_2 evolution in CuO/TiO_2 photocatalysts. Few studies reported CuO as the active component,[216, 275, 283, 284] while others have reported that CuO undergoes internal restructuring to Cu_2O during photoelectrolysis, and the latter becomes the active component.[291] Alternatively, another suggestion has been that TiO_2 alone acts as an active component, as the light source contains a percentage of UV light. Ambiguity arises from different synthetic routes employed, which results in varying energy levels of the valence and conduction bands.

The attempt to prepare CuO/TiO_2 BHJ architectures was successful, but their photocurrent and photoefficiency were low. Low photocurrents may be attributed to one or more of the following: (a) photocorrosion of CuO (b) the CuO/TiO_2 interface acting as a

recombination center due to a small energy difference between the valence band of the former and the conduction band of the latter,[294] (c) the presence of surface states at the donor/acceptor interface which acts as recombination centers, and (d) poor interface formation between donor and acceptor materials resulting in reduced charge transfer efficiency. Although the hypothesis could not be validated for the aforementioned reasons, further studies of inorganic BHJ electrodes with different donor:acceptor material combinations merit more attention. Towards this end, the results obtained in this study provide initial information with regard to the research methodologies and interfacial phenomena for inorganic BHJ electrodes.

Chapter 5.

Conclusions and Future Directions

5.1. Introduction

In a traditional photoelectrochemical (PEC) device where planar electrode architecture (TC/photoelectrode) is typically employed, the electric field established at the electrode/electrolyte interface (i.e., depletion region) plays a significant role in exciton separation (as discussed in section 1.2.1). Hence, nanostructures have been widely used by researchers to increase the efficiency of the photoelectrodes by increasing the electrode/electrolyte interface. However, as the PEC field matured, researchers arrived at a consensus that photoelectrodes having a device architecture TC/HTL/SC/ETL/HER-EC (for photocathodes) or TC/ETL/SC/HTL/OER-EC (for photoanodes) is necessary to obtain high energy conversion efficiency and good stability.[a]

After incorporating charge transport, protective, and catalytic layers, the PEC device is not driven by the electric field at the photoelectrode/electrolyte interface but from the photoactive materials and charge transport layers similar to PVs. Thus, instead of the surface-dependent photoelectrochemical behaviour of the simple photoelectrodes, the bulk properties of the photoactive material such as domain size, crystallinity and interconnectivity are expected to play a significant role in determining the devices' performances.

5.2. Organic BHJ Electrodes

In the emerging field of organic semiconductors, where a combination of donor and acceptor materials is necessary to dissociate an exciton into component charges, the

[a] TC-Transparent conductor
ETL-Electron transport layer
HTL-Hole transport layer
SC-Semiconductor
HER-EC–Hydrogen evolution reaction - electrocatalyst
OER-EC –Oxygen evolution reaction - electrocatalyst

bulk electrode's structure determines the device's performance.[316] Hence, it was attempted to form a nanoparticle-based BHJ electrode which will allow control over BHJ domain size during the preparation of nanoparticles. Towards this, in chapter three, npP3HT and npPCBM nanoparticles were individually prepared by miniemulsion technique which are dispersed in an aqueous solution and subsequently used to make a bulk-heterojunction electrode.

By separating the npP3HT and npPCBM nanoparticles, the long-range order within P3HT nanoparticles and hence electronic properties is preserved. The synthesized electrode performed much better than the planar BHJ electrode and the nanoparticle BHJ electrode prepared via the precipitation method. Though the increased photocurrent and higher onset potential indicate better performance of miniemulsion synthesized electrodes, the photoelectrochemical properties of these electrodes are unoptimized. The presented work represents a preliminary investigation that provides the basis for exploring new nanoparticle systems with different photoactive polymers and greater control and variation of the dispersion formed. For example, the following research directions are recommended for disordered, phase-separated electrode research.

5.2.1. Control of Nanoparticle Size

The miniemulsion nanoparticle size depends on several processing parameters such as ultrasonication power, time, temperature, type of solvent, and nature and concentration of surfactants.[252, 317] For example, an increase in surfactant concentration will lead to smaller miniemulsion droplet size which will consequently result in smaller particle size.[318] A BHJ photoelectrode prepared from the smaller nanoparticles is expected to perform better as it will exhibit a higher donor:acceptor interface area than that consisting of larger particles. However, as smaller nanoparticles lead to a higher concentration of non-photoactive and non-conductive surfactants in the photoelectrode, it is also expected to negatively affect the photoelectrodes' performance. Hence, identifying optimal surfactant concentration is essential to achieve maximum performance for the given polymer-surfactant combination.

5.2.2. Removal of Surfactants

Surfactants are compounds that contain both hydrophilic and hydrophobic groups in one structure. The most widely used surfactant, sodium dodecyl sulfate (SDS) contains a hydrophobic tail, a negatively charged hydrophilic head group, and a counter-ion for charge balance (Figure 5.1). Since the head group carries a negative charge, SDS is an anionic surfactant. Similarly, cationic surfactant cetyltrimethyl ammonium bromide (CTAB) contains a positive head group and negative (Br^-) counter-ion. Surfactants with no charge groups also exist like Tween-20, Triton-100 etc., known as non-ionic surfactants. Since surfactants are invariably present in miniemulsion synthesized NPs (depicted in Figure 3.3), it is essential to understand their effect/interference on the functions of the photoactive layer.

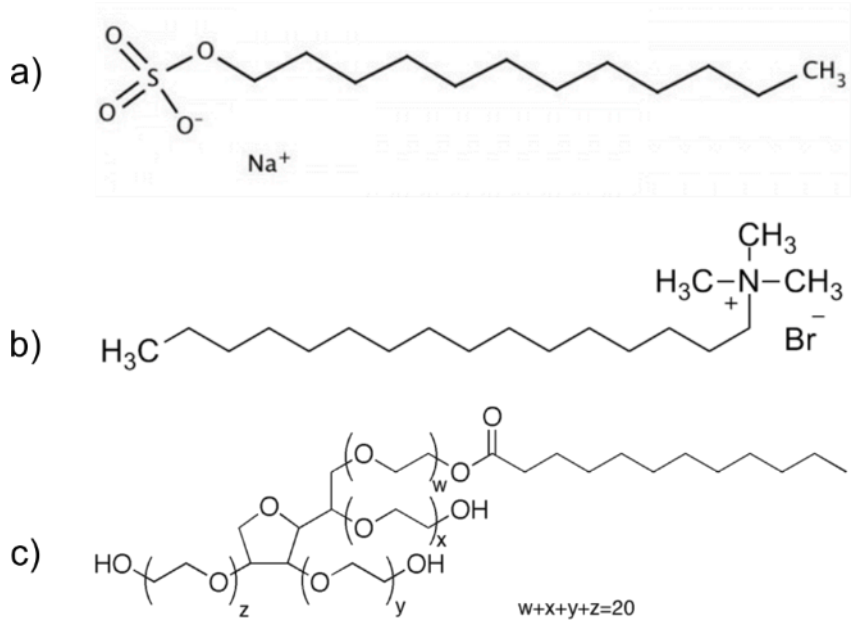

Figure 5.1 Molecular structure of (a) sodium dodecyl sulfate (SDS, anionic), (b) cetyltrimethyl ammonium bromide (CTAB, cationic), and (c) polyoxyethylene sorbitan monolaurate (Tween-20, non-ionic) surfactants.

The BHJ electrodes absorb light and generate electrons and holes. The photogenerated charges (electrons for photocathodes and holes for photoanodes) are then transferred to the electrode/electrolyte interface either due to diffusion or under the influence of a built-in electrical field. Since surfactants are either charged (anionic or cationic) or non-conductive (non-ionic), it is expected to minimize or impede the charge transport across the film or charge transfer at the electrode/electrolyte interface.[319] Hence,

after NP formation, it is recommended to remove the excess surfactants present in the NP dispersion by processes such as dialysis centrifugal filtration. However, as it is impossible to remove the surfactants completely, their impact on the photophysical processes of miniemulsion nanoparticles must be understood to prepare highly efficient photoelectrodes.

5.2.3. Effect of Crystallinity

In BHJ-based OPV devices, thermal annealing is typically performed to control the domain size of phases and to increase the crystallinity of photoactive materials. Ideally, it is desirable to increase the crystallinity i.e., interchain packing without increasing the nanoparticle size. It has been shown in the literature that annealing in the temperature range of 120–150 °C for 10–30 min improves the crystallinity via increased molecular ordering, reduces the voids in the electrode, and results in better film homogeneity without a significant increase in domain size.[320, 321] These changes result in enhanced intra- and inter-particle charge transport that translates to increased efficiency.[122, 320] However, as the traditional BHJ electrodes contain an intermix of polymer and electron acceptor, the extent of the effect of annealing on polymers' crystallinity is limited by the presence of an electron acceptor. In miniemulsion prepared nanoparticle BHJ electrodes, as the domains are phase separated, the effect of annealing on crystallinity is expected to be more pronounced than in planar BHJ electrodes. This warrants an investigation to understand the annealing effect on interconnectivity, crystallinity, and nanoparticle growth of semiconducting polymers in the presence of surfactants.

After optimizing the above-mentioned parameters, the phase-separated nanoparticle-based BHJ approach can potentially be applied to a variety of organic semiconductors such as low bandgap polymers,[96, 322, 323] small-molecule organic semiconductors,[324] n-type polymers (photoanodes),[128, 145, 325-327] non-fullerene acceptors,[141, 145, 328-332] donor-acceptor polymers,[333, 334] and high-dielectric polymers.[335, 336]

5.3. Inorganic BHJ Electrodes

Several earth-abundant inorganic semiconductors, such as Fe_2O_3, Cu_2O, and CuO, have poor photoelectronic properties, i.e., fast recombination time, long optical absorption length, and less exciton diffusion length. These issues are typically addressed

in the literature by employing nanostructures. Inspired by the performance of the phase-separated randomly-distributed organic BHJ electrodes, it was attempted to replicate BHJ nanoparticle electrode architecture in inorganics. Indeed, in chapter four, a randomly distributed inorganic BHJ electrode comprising CuO (donor) and TiO_2 (acceptor) nanoparticle-based BHJ electrode is studied.

Although npCuO:npTiO$_2$ BHJ electrode was successfully prepared, the effect of BHJ nanostructures on the performance of inorganic photoelectrode could not be verified. The chosen photoactive material, CuO, underwent photocorrosion, which was addressed by employing protective and catalyst layers. Furthermore, TiO_2 was determined not to act as an electron acceptor or electron transport layer but rather acted to promote exciton recombination, contradicting the literature reports. This was attributed to the increased CuO/TiO_2 interface area in the BHJ electrode studied versus the planar heterojunction electrodes typically examined in the literature. For these reasons, the hypothesis proposed in this thesis could not be verified for the chosen inorganic photoactive materials.

It is necessary to distinguish the donor and acceptor interface in organic and inorganic materials to understand the contrasting npBHJ electrode performance. In inorganics, as the periodic structure of a crystal lattice is terminated, there exists a plane of dangling bonds at the surface. The energy levels of these bonds, termed surface states, are different from the bulk material's energy level.[337] This fundamentally alters the electronic structure of the surface and introduces new electronic states within the bandgap that dominate the interfacial charge transfer. The effect of the surface state is magnified in BHJ electrodes due to an exponential increase in interfacial surface area compared to planar heterojunction. On the other hand, the surface of a polymer semiconductor is fundamentally different as no bonds are broken to form the surface. Furthermore, there is no requirement for the adjacent material to share the same chemical or structural properties. This allows polymer heterojunctions to be formed easily via simple solution-based approaches.

Hence, a photoactive material can undergo three types of recombination processes: [338] i.e., (i) recombination in bulk, (ii) recombination at the surface, and (iii) recombination at the layer/layer interface. The method proposed in this thesis, i.e., phase-separated donor:acceptor bulk-heterojunction, is suitable for electrodes whose efficiency

is limited by bulk recombination. If other recombination sources exist, that must be addressed before employing the BHJ approach.

For the above-mentioned reasons, further studies of inorganic BHJ electrodes with suitable donor:acceptor combinations merit more attention and will likely provide additional information on the interfacial phenomena leading to increased photoefficiency. The results from chapter four indicate that the selection of donor and acceptor plays an important role in forming inorganic BHJ electrodes. The semiconductors must display the following characteristics to be able to explore the BHJ effect in inorganics: (i) It must undergo significant bulk recombination, (ii) it should form a type-II heterojunction with acceptor material, (iii) the donor:acceptor interface must be defect-free, (iv) the acceptor material must have similar or higher melting temperature than photoactive material, and (v) any existing defects on the nanoparticles' surface must be addressed/passivated before BHJ formation.

5.4. Long-term View

PEC research aims to achieve the targets set by DOE for H_2 production to be a potential alternative to using fossil fuel-based resources for H_2 generation. Currently, the cycle of validating a photocatalyst material for solar H_2 generation is as follows (Figure 5.2):

(i) First, the performance of the material is verified for H_2 generation via the ‘photocatalytic (PC)’ method, a low-cost, easy to implement in a large-scale technique.

(ii) If the performance is found unsatisfactory, the material is assessed as a ‘photocatalytic sheet’ where the semiconductor is immobilized as an electrode where the particle aggregation provides efficient charge transport pathways.

(iii) Failing which, the material is validated in a PEC reactor, where it is possible to address the shortcoming of the photocatalyst by connecting with a counter electrode. Here the material is evaluated under different surface modifications, surface treatments, heterojunction with different photocatalysts, etc.

(iv) The efficiency and cost of H_2 generation via PC and PEC method using a particular photocatalyst are compared with that of hydrogen generated using commercially available electrolyzer powered by photovoltaics.

(v) The photocatalyst that fails the previous condition is labelled as 'unsuitable' for PEC, and the cycle continues with a different or modified photocatalyst.

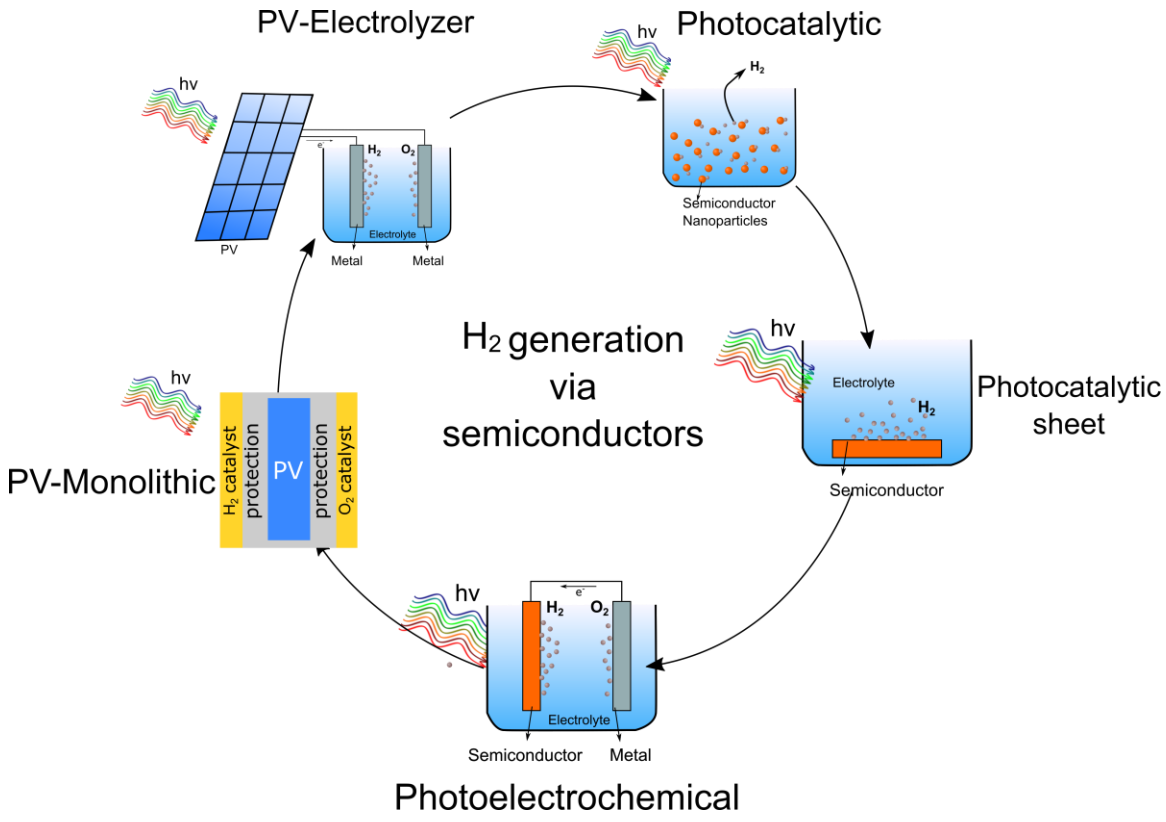

Figure 5.2 Schematic depicting different solar hydrogen generation pathways using semiconductors.

In the last few years, the brute force approach of coupling an electrolyzer with a photovoltaic cell (PV-Electrolyzer) was touted as a readily available and commercially implementable pathway to green H_2, with the cost of the produced H_2 being the only concern. However, as both photovoltaics and electrolyzer technologies matured significantly in recent years in both cost and efficiency, the PV-electrolyzer approach looks more attractive. Owing to this, research articles questioning the future of PEC research, such as 'PEC water splitting: An idea heading to obsolescence?' began to appear in the literature.[339]

When PV and electrolyzer technologies are coupled to make H_2, the intersection of the I-V curves of the electrolyzer and photovoltaic cell represents the coupling point that determines the maximum operating voltage (V_{OP}) and current (I_{OP}) of the combined system. Hence, the coupled device's efficiency is the product of individual photovoltaic and electrolyzer efficiencies and the coupling factor. Thus, both technologies cannot operate at individual peak efficiency but at reduced efficiency, as depicted in Figure 5.3a. On the contrary, the PEC approach of combining electrolysis and photon absorption in a single device is more efficient than the PV-driven electrolyzer approach, and hence the cost of the produced H_2 in the former will eventually be lesser as the PEC field matures.[46, 340] Furthermore, even in the worst-case scenario of PEC cells not being competitive with the PV-electrolyzer approach for H_2 generation, PEC electrodes can generate partial photopotential via the PV-PEC approach, which will give solar hydrogen an increased advantage over using electricity-grid powered electrolyzers.[17, 70, 341-344]

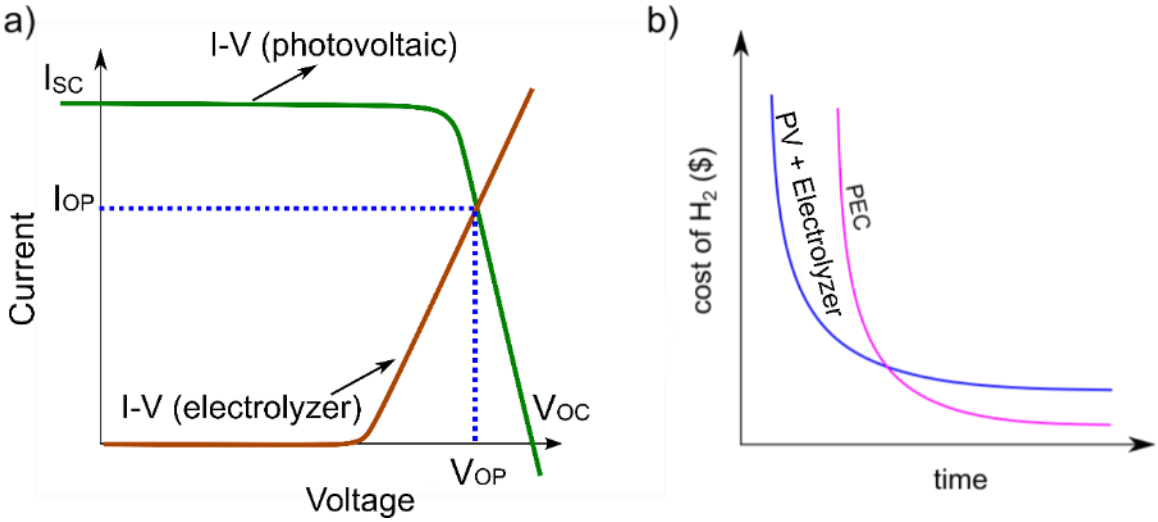

Figure 5.3 **(a) Schematic current-voltage characteristics of a photovoltaic cell and an electrolyzer. I_{SC} and V_{OC} represent photovoltaic short–circuit current and open-circuit voltage, respectively; I_{OP} and V_{OP} are operating current and voltage when an electrolyzer is coupled with photovoltaics. (b) Expected progress in cost of H_2 generation via PV-electrolyzer and PEC approaches.**

To compete with the PV-electrolyzer approach, PEC cells must see a significant improvement in terms of cost of H_2 and hours of stable operation. Towards this end, new photocatalysts (such as perovskites,[345] organic semiconductors,[346] metal-organic frameworks,[347] quantum dots[348]), new technologies (such as light concentrators, back reflectors, anti-reflectors, light trapping),[349, 350] new physical phenomena (such as photon

upconversion,[351] surface plasmons,[352, 353] multiple exciton generation[354]) are constantly explored, pushing the boundaries of efficiency limitation. However, the process of validating a newly developed electrode is exhaustive, as the material must be studied under different types of modifications, such as nanostructuring, doping, surface modifications, thermal treatments, catalysts, and heterojunction with different semiconductors before arriving at a consensus decision. The phase-separated BHJ nanoparticle approach described in this thesis is explored as one of the pathways to validate the suitability of photocatalysts for future electrode developments.

References

1. Rhodes, C. J. *Sci. Prog.* **2016,** *99*, 97.

2. Michaelowa, A. *Intereconomics* **2021,** *56*, 302.

3. Kannan, N.; Vakeesan, D. *Renew. Sust. Energ. Rev.* **2016,** *62*, 1092.

4. Green, M. A.; Dunlop, E. D.; Hohl-Ebinger, J.; Yoshita, M.; Kopidakis, N.; Hao, X. *Prog. Photovolt.: Res. Appl.* **2021,** *30*, 3.

5. Swanson, R. M. *Prog. Photovolt.: Res. Appl.* **2006,** *14*, 443.

6. Yin, J.; Molini, A.; Porporato, A. *Nat. Commun.* **2020,** *11*, 4781.

7. Asiaban, S.; Kayedpour, N.; Samani, A. E.; Bozalakov, D.; De Kooning, J. D. M.; Crevecoeur, G.; Vandevelde, L. *Energies* **2021,** *14*, 2630.

8. Hou, Y.; Vidu, R.; Stroeve, P. *Ind. Eng. Chem. Res.* **2011,** *50*, 8954.

9. Aneke, M.; Wang, M. *Appl. Energy* **2016,** *179*, 350.

10. Walter, M. G.; Warren, E. L.; McKone, J. R.; Boettcher, S. W.; Mi, Q.; Santori, E. A.; Lewis, N. S. *Chem. Rev.* **2010,** *110*, 6446.

11. Yang, W.; Prabhakar, R. R.; Tan, J.; Tilley, S. D.; Moon, J. *Chem. Soc. Rev.* **2019,** *48*, 4979.

12. Yukesh Kannah, R.; Kavitha, S.; Preethi; Parthiba Karthikeyan, O.; Kumar, G.; Dai-Viet, N. V.; Rajesh Banu, J. *Bioresour. Technol.* **2021,** *319*, 124175.

13. Nikolaidis, P.; Poullikkas, A. *Renew. Sust. Energ. Rev.* **2017,** *67*, 597.

14. Ghiat, I.; Al-Ansari, T. *J. CO_2 Util.* **2021,** *45*, 101432.

15. Nguyen, T.; Abdin, Z.; Holm, T.; Mérida, W. *Energy Convers. Manag.* **2019,** *200*, 112108.

16. Shiva Kumar, S.; Himabindu, V. *Mater. Sci. Energy Technol.* **2019,** *2*, 442.

17. Jia, J.; Seitz, L. C.; Benck, J. D.; Huo, Y.; Chen, Y.; Ng, J. W.; Bilir, T.; Harris, J. S.; Jaramillo, T. F. *Nat. Commun.* **2016,** *7*, 13237.

18. Abanades, S.; Flamant, G. *Sol. Energy* **2006,** *80*, 1611.

19. Dehghanimadvar, M.; Shirmohammadi, R.; Sadeghzadeh, M.; Aslani, A.; Ghasempour, R. *Int. J. Energy Res.* **2020,** *44*, 8233.

20. Acar, C.; Dincer, I. *J. Clean. Prod.* **2019,** *218*, 835.

21. Holladay, J. D.; Hu, J.; King, D. L.; Wang, Y. *Catal. Today* **2009,** *139*, 244.

22. Dutta, S. *Energy Fuels* **2021,** *35*, 11613.

23. Li, R.; Li, C., Photocatalytic Water Splitting on Semiconductor-Based Photocatalysts. In *Advances in Catalysis*, Song, C., Ed. Academic Press: **2017,** 60, 1.

24. Benck, J. D.; Hellstern, T. R.; Kibsgaard, J.; Chakthranont, P.; Jaramillo, T. F. *ACS Catal.* **2014,** *4*, 3957.

25. Gorlin, M.; Chernev, P.; Ferreira de Araujo, J.; Reier, T.; Dresp, S.; Paul, B.; Krahnert, R.; Dau, H.; Strasser, P. *J. Am. Chem. Soc.* **2016,** *138*, 5603.

26. Wu, H.; Tan, H. L.; Toe, C. Y.; Scott, J.; Wang, L.; Amal, R.; Ng, Y. H. *Adv. Mater.* **2020,** *32*, 1904717.

27. Abe, R. *J. Photochem. Photobiol. C: Photochem. Rev.* **2010,** *11*, 179.

28. Kumaravel, V.; Imam, M.; Badreldin, A.; Chava, R.; Do, J.; Kang, M.; Abdel-Wahab, A. *Catalysts* **2019,** *9*, 276.

29. Wang, M.; Shen, S.; Li, L.; Tang, Z.; Yang, J. *J. Mater. Sci.* **2017,** *52*, 5155.

30. Chiarello, G. L.; Selli, E., Photocatalytic Production of Hydrogen. In *Advances in Hydrogen Production, Storage and Distribution*, Angelo Basile; Adolfo Iulianelli, Eds. Woodhead Publishing: **2014,** 216.

31. Hisatomi, T.; Kubota, J.; Domen, K. *Chem. Soc. Rev.* **2014,** *43*, 7520.

32. Low, J.; Yu, J.; Jaroniec, M.; Wageh, S.; Al-Ghamdi, A. A. *Adv. Mater.* **2017,** *29*, 1601694.

33. Fajrina, N.; Tahir, M. *Int. J. Hydrog. Energy* **2019,** *44*, 540.

34. Wang, Y.; Shang, X.; Shen, J.; Zhang, Z.; Wang, D.; Lin, J.; Wu, J. C. S.; Fu, X.; Wang, X.; Li, C. *Nat. Commun.* **2020,** *11*, 3043.

35. Ng, B. J.; Putri, L. K.; Kong, X. Y.; Teh, Y. W.; Pasbakhsh, P.; Chai, S. P. *Adv. Sci.* **2020,** *7*, 1903171.

36. Chen, S.; Takata, T.; Domen, K. *Nat. Rev. Mater.* **2017,** *2*, 17050.

37. Lin, L.; Hisatomi, T.; Chen, S.; Takata, T.; Domen, K. *Trends Chem.* **2020,** *2*, 813.

38. Nadeem, M. A.; Khan, M. A.; Ziani, A. A.; Idriss, H. *Catalysts* **2021,** *11*, 60.

39. Grätzel, M. *Nature* **2001,** *414*, 338.

40. Liu, Y.; Bai, S.; Wang, F.; Chen, Y. *Environ. Chem. Lett.* **2022,** *20*, 1169.

41. Bak, T.; Nowotny, J.; Rekas, M.; Sorrell, C. C. *Int. J. Hydrog. Energy* **2002,** *27*, 991.

42. Singleton, J., *Band Theory and Electronic Properties of Solids*. Oxford University Press: New York, **2001**.

43. Rajeshwar, K., Fundamentals of Semiconductor Electrochemistry and Photoelectrochemistry. In *Encyclopedia of Electrochemistry*, Bard, A. J., Ed. **2007**.

44. Sugiyama, M.; Fujii, K.; Nakamura, S., *Solar to Chemical Energy Conversion Theory and Application*. Springer International Publishing: Swizerland, **2016**.

45. Y.Yu, P.; Cardona, M., *Fundamentals of Semiconductors : Physics and Materials Properties*. Springer: New York, **2010**.

46. Jiang, C.; Moniz, S. J. A.; Wang, A.; Zhang, T.; Tang, J. *Chem. Soc. Rev.* **2017,** *46*, 4645.

47. Bard, A. J.; Faulkner, L. R., *Electrochemical Methods Fundamentals and Applications*. John Wiley & Sons, Inc: New York, **2001**.

48. Vidal-Iglesias, F. J.; Solla-Gullón, J.; Rodes, A.; Herrero, E.; Aldaz, A. *J. Chem. Educ.* **2012,** *89*, 936.

49. Landolt, D., *Corrosion and Surface Chemistry of Metals*. CRC Press: **2007**.

50. Helmholtz, H. *Ann. Phys. Chem.* **1879,** *243*, 337.

51. Nakamura, M.; Sato, N.; Hoshi, N.; Sakata, O. *Chemphyschem* **2011,** *12*, 1430.

52. Bott, A. W. *Curr. Sep.* **1998,** *17*, 87.

53. Chen, Z.; Dinh, H. N.; Miller, E., *Photoelectrochemical Water Splitting Standards, Experimental Methods, and Protocols*. Springer Inc: New York, **2013**.

54. Ros, C.; Andreu, T.; Morante, J. R. *J. Mater. Chem. A* **2020,** *8*, 10625.

55. Aruchamy, A.; Aravamudan, G.; Subba Rao, G., V. *Bull. Mater. Sci.* **1982,** *4*, 483.

56. Tauc, J. *Mat. Res. Bull.* **1968,** *3*, 37.

57. Makula, P.; Pacia, M.; Macyk, W. *J. Phys. Chem. Lett.* **2018,** *9*, 6814.

58. Zanatta, A. R. *Sci. Rep.* **2019,** *9*, 11225.

59. Murphy, A. *Sol. Energy Mater. Sol. Cells* **2007,** *91*, 1326.

60. Bott, A. W. *Curr. Sep.* **1998,** *17*, 87.

61. Berger, T.; Monllor-Satoca, D.; Jankulovska, M.; Lana-Villarreal, T.; Gomez, R. *Chemphyschem* **2012,** *13*, 2824.

62. Yang, M.; Zhang, L.; Jin, B.; Huang, L.; Gan, Y. *Appl. Surf. Sci.* **2016,** *364*, 410.

63. Zaban, A.; Greenshtein, M.; Bisquert, J. *Chemphyschem* **2003,** *4*, 859.

64. Orazem, M. E.; Tribollet, B., *Electrochemical Impedance Spectroscopy*. Jon Wiley & Sons, Inc : New Jersey, **2008**.

65. Lasia, A., *Electrochemical Impedance Spectroscopy and its Applications*. Springer: New York, **2014**.

66. Chang, B. Y.; Park, S. M. *Annu. Rev. Anal. Chem.* **2010,** *3*, 207.

67. Chakhari, W.; Ben Naceur, J.; Ben Taieb, S.; Ben Assaker, I.; Chtourou, R. *J. Alloys Compd.* **2017,** *708*, 862.

68. Harris, D. C., *Quantitative Chemical Analysis*. W. H. Freeman and Company: New York, **2010**.

69. Sivula, K.; Le Formal, F.; Grätzel, M. *ChemSusChem* **2011,** *4*, 432.

70. Shaner, M. R.; Atwater, H. A.; Lewis, N. S.; McFarland, E. W. *Energy Environ. Sci.* **2016,** *9*, 2354.

71. Fujishima, A.; Honda, K. *Nature* **1972,** *238*, 37.

72. Moss, B.; Babacan, O.; Kafizas, A.; Hankin, A. *Adv. Energy Mater.* **2021,** *11*, 2003286.

73. Goga, N.; Mayrhofer, L.; Tranca, I.; Nedea, S.; Heijmans, K.; Ponnuchamy, V.; Vasilateanu, A. *Catalysts* **2021,** *11*, 807.

74. Li, Z.; Luo, W.; Zhang, M.; Feng, J.; Zou, Z. *Energy Environ. Sci.* **2013,** *6*, 347.

75. Eftekhari, A.; Babu, V. J.; Ramakrishna, S. *Int. J. Hydrog. Energy* **2017,** *42*, 11078.

76. Benanti, T. L.; Venkataraman, D. *Photosynth. Res.* **2006,** *87*, 73.

77. Brabec, C. J.; Gowrisanker, S.; Halls, J. J.; Laird, D.; Jia, S.; Williams, S. P. *Adv. Mater.* **2010,** *22*, 3839.

78. Zheng, Y. Nanostructured Thin Films for Organic Photovoltaic Cells and Organic Light Emitting Diodes. University of Florida, **2009**.

79. Hoppe, H.; Sariciftci, N. S. *J. Mater. Res.* **2011,** *19*, 1924.

80. Søndergaard, R.; Helgesen, M.; Jørgensen, M.; Krebs, F. C. *Adv. Energy Mater.* **2011,** *1*, 68.

81. Krebs, F. *Sol. Energy Mater. Sol. Cells* **2009,** *93*, 394.

82. Andersen, T. R.; Larsen-Olsen, T. T.; Andreasen, B.; Bottiger, P. L. A.; Carl, J. E.; M., H.; Bundgaard, E.; Norrman, K.; Andreasen, W. J.; Jørgensen, M.; C., K. F. *ACS Nano* **2011,** *5*, 4188.

83. Schwoerer, M.; Wolf, H. C., *Organic Molecular Solids*. WILEY-VCH Verlag GmbH & Co. KGaA: Weinheim, **2007**.

84. Wang, C.; Dong, H.; Jiang, L.; Hu, W. *Chem. Soc. Rev.* **2018,** *47*, 422.

85. Jiang, L.; Dong, H.; Hu, W. *J. Mater. Chem.* **2010,** *20*.

86. Shirakawa, H.; Louis, E. J.; Macdiarmid, A. G.; Chiang, C. K.; Heeger, A. J. *J. Chem. Soc., Chem. Commun.,* **1977,** 578.

87. Rasmussen, S. C. *Bull. Hist. Chem.* **2014,** *39*, 64.

88. Laquai, F.; Park, Y. S.; Kim, J. J.; Basche, T. *Macromol. Rapid Commun.* **2009,** *30*, 1203.

89. Köhler, A.; Bässle, H., *Electronic Processes in Organic Semiconductors*. Wiley-VCH Verlag GmbH & Co. KGaA: Weinheim, **2015**.

90. Giebink, N. C.; Wiederrecht, G. P.; Wasielewski, M. R.; Forrest, S. R. *Phys. Rev. B* **2011,** *83*, 195326.

91. Shaw, P. E.; Ruseckas, A.; Samuel, I. D. W. *Adv. Mater.* **2008,** *20*, 3516.

92. Kang, D.; Kim, T. W.; Kubota, S. R.; Cardiel, A. C.; Cha, H. G.; Choi, K. S. *Chem. Rev.* **2015,** *115*, 12839.

93. Li, Y. *Acc. Chem. Res.* **2012,** *45*, 723.

94. Koeppe, R.; Sariciftci, N. S. *Photochem. Photobiol. Sci.* **2006,** *5*, 1122.

95. Thompson, B. C.; Frechet, J. M. *Angew. Chem.* **2008,** *47*, 58.

96. Dang, M. T.; Hirsch, L.; Wantz, G. *Adv. Mater.* **2011,** *23*, 3597.

97. Clafton, S. N. Photophysics and Photochemistry of Conjugated Polymer Nanoparticles. University of Adelaide, **2014**.

98. Mikhnenko, O. V.; Blom, P. W. M.; Nguyen, T. P. *Energy Environ. Sci.* **2015,** *8*, 1867.

99. Chen, L. X. *ACS Energy Lett.* **2019,** *4*, 2537.

100. Günes, S.; Neugebauer, H.; Sariciftci, N. S. *Chem. Rev.* **2007,** *107*, 1324.

101. Guo, X.; Facchetti, A. *Nat. Mater.* **2020,** *19*, 922.

102. Otep, S.; Wang, Y.; Kohara, A.; Matsumoto, H.; Mori, T.; Michinobu, T. *ACS Appl. Polym. Mater.* **2019,** *1*, 2302.

103. Wang, Y.; Masunaga, H.; Hikima, T.; Matsumoto, H.; Mori, T.; Michinobu, T. *Macromolecules* **2015,** *48*, 4012.

104. Meyers, F.; Heeger, A. J.; Brédas, J. L. *J. Chem. Phys.* **1992,** *97*, 2750.

105. Groenendaal, L.; Jonas, F.; Freitag, D.; Pielartzik, H.; Reynolds, J. R. *Adv. Mater.* **2000,** *12*, 481.

106. Tang, C. W. *Appl. Phys. Lett.* **1986,** *48*, 183.

107. Sariciftci, N. S.; Smilowitz, L.; Heeger, A. J.; Wudl, F. *Science* **1992,** *258*, 1474.

108. Yu, G.; Gao, J.; Hummelen, J. C.; Wudl, F.; Heeger, A. J. *Science* **1995,** *270*, 1789.

109. Saito, S.; Oshiyama, A. *Phys. Rev. Lett.* **1991,** *66*, 2637.

110. Morita, S.; AZakhidov, A.; Yoshino, K. *Solid State Commun.* **1992,** *82*, 249.

111. Li, G.; Shrotriya, V.; Huang, J.; Yao, Y.; Moriarty, T.; Emery, K.; Yang, Y. *Nat. Mater.* **2005,** *4*, 864.

112. Singh, T. B.; Sariciftci, N. S. *Annu. Rev. Mater. Res.* **2006,** *36*, 199.

113. El-Rashiedy, O. A.; Holdcroft, S. *J. Phys. Chem.* **1996,** *100*, 5481.

114. Abe, T.; Tobinai, S.; Taira, N.; Chiba, J.; Itoh, T.; Nagai, K. *J. Phys. Chem. C* **2011,** *115*, 7701.

115. Lanzarini, E.; Antognazza, M. R.; Biso, M.; Ansaldo, A.; Laudato, L.; Bruno, P.; Metrangolo, P.; Resnati, G.; Ricci, D.; Lanzani, G. *J. Phys. Chem. C* **2012,** *116*, 10944.

116. Bellani, S.; Antognazza, M. R.; Bonaccorso, F. *Adv. Mater.* **2019,** *31*, e1801446.

117. Otep, S.; Michinobu, T.; Zhang, Q. *Sol. RRL* **2019,** *4*.

118. Queyriaux, N.; Kaeffer, N.; Morozan, A.; Chavarot-Kerlidou, M.; Artero, V. *J. Photochem. Photobiol. C: Photochem. Rev.* **2015,** *25*, 90.

119. Hoppe, H.; Niggemann, M.; Winder, C.; Kraut, J.; Hiesgen, R.; Hinsch, A.; Meissner, D.; Sariciftci, N. S. *Adv. Funct. Mater.* **2004,** *14*, 1005.

120. Snaith, H. J.; Arias, A. C.; Morteani, A. C.; Silva, C.; Friend, R. H. *Nano Lett.* **2002,** *2*, 1353.

121. Laquai, F.; Andrienko, D.; Mauer, R.; Blom, P. W. *Macromol. Rapid Commun.* **2015,** *36*, 1001.

122. Gartner, S.; Christmann, M.; Sankaran, S.; Rohm, H.; Prinz, E. M.; Penth, F.; Putz, A.; Tureli, A. E.; Penth, B.; Baumstummler, B.; Colsmann, A. *Adv. Mater.* **2014,** *26*, 6653.

123. Ma, W.; Yang, C.; Gong, X.; Lee, K.; Heeger, A. J. *Adv. Funct. Mater.* **2005,** *15*, 1617.

124. Xue, B.; Vaughan, B.; Poh, C.-H.; Burke, K. B.; Thomsen, L.; Stapleton, A.; Zhou, X.; Bryant, G. W.; Belcher, W.; Dastoor, P. C. *J. Phys. Chem. C* **2010,** *114*, 15797.

125. Peet, J.; Senatore, M. L.; Heeger, A. J.; Bazan, G. C. *Adv. Mater.* **2009,** *21*, 1521.

126. Xu, H.; Yuan, F.; Zhou, D.; Liao, X.; Chen, L.; Chen, Y. *J. Mater. Chem. A* **2020,** *8*, 11478.

127. Lattante, S. *Electronics* **2014,** *3*, 132.

128. Yao, L.; Rahmanudin, A.; Guijarro, N.; Sivula, K. *Adv. Energy Mater.* **2018,** *8*, 1802585.

129. Bourgeteau, T.; Tondelier, D.; Geffroy, B.; Brisse, R.; Cornut, R.; Artero, V.; Jousselme, B. *ACS Appl. Mater. Interfaces* **2015,** *7*, 16395.

130. Bourgeteau, T.; Tondelier, D.; Geffroy, B.; Brisse, R.; Campidelli, S.; Cornut, R.; Jousselme, B. *J. Mater. Chem. A* **2016,** *4*, 4831.

131. Betancur, R.; Maymó, M.; Elias, X.; Vuong, L. T.; Martorell, J. *Sol. Energy Mater. Sol. Cells* **2011,** *95*, 735.

132. Fumagalli, F.; Bellani, S.; Schreier, M.; Leonardi, S.; Rojas, H. C.; Ghadirzadeh, A.; Tullii, G.; Savoini, A.; Marra, G.; Meda, L.; Grätzel, M.; Mayer, M. T.; Antognazza, M. R.; Fonzo, F. D. *J. Mater. Chem. A.* **2016,** *4*, 2178.

133. Ghadirzadeh, A.; Fumagalli, F.; Mezzetti, A.; Bellani, S.; Meda, L.; Antognazza, M. R.; Di Fonzo, F. *ChemPhotoChem* **2018,** *2*, 283.

134. Mezzetti, A.; Fumagalli, F.; Alfano, A.; Iadicicco, D.; Antognazza, M. R.; di Fonzo, F. *Faraday Discuss. Chem. Soc.* **2017,** *198*, 433.

135. Bellani, S.; Najafi, L.; Martín-García, B.; Ansaldo, A.; Del Rio Castillo, A. E.; Prato, M.; Moreels, I.; Bonaccorso, F. *J. Phys. Chem. C* **2017,** *121*, 21887.

136. Rojas, H. C.; Bellani, S.; Fumagalli, F.; Tullii, G.; Leonardi, S.; Mayer, M. T.; Schreier, M.; Grätzel, M.; Lanzani, G.; Di Fonzo, F.; Antognazza, M. R. *Energy Environ. Sci.* **2016,** *9*, 3710.

137. Steier, L.; Bellani, S.; Rojas, H. C.; Pan, L.; Laitinen, M.; Sajavaara, T.; Di Fonzo, F.; Grätzel, M.; Antognazza, M. R.; Mayer, M. T. *Sustain. Energy Fuels* **2017,** *1*, 1915.

138. Rojas, H. C.; Bellani, S.; Sarduy, E. A.; Fumagalli, F.; Mayer, M. T.; Schreier, M.; Grätzel, M.; Di Fonzo, F.; Antognazza, M. R. *ACS Omega* **2017,** *2*, 3424.

139. Haro, M.; Solis, C.; Molina, G.; Otero, L.; Bisquert, J.; Gimenez, S.; Guerrero, A. *J. Phys. Chem. C* **2015,** *119*, 6488.

140. Najafi, L.; Romano, V.; Oropesa-Nuñez, R.; Prato, M.; Lauciello, S.; D'Angelo, G.; Bellani, S.; Bonaccorso, F. *Small Struct.* **2020,** *2*, 2000098.

141. Shi, W.; Li, D.; Fan, W.; Ma, J.; Li, C.; Yu, W.; Shi, J.; Li, C. *Adv. Funct. Mater.* **2020,** *30*.

142. Bourgeteau, T.; Tondelier, D.; Geffroy, B.; Brisse, R.; Laberty-Robert, C.; Campidelli, S.; de Bettignies, R.; Artero, V.; Palacin, S.; Jousselme, B. *Energy Sustain. Soc.* **2013,** *6*, 2706.

143. Shi, W.; Yu, W.; Li, D.; Zhang, D.; Fan, W.; Shi, J.; Li, C. *Chem. Mater.* **2019,** *31*, 1928.

144. Yao, L.; Guijarro, N.; Boudoire, F.; Liu, Y.; Rahmanudin, A.; Wells, R. A.; Sekar, A.; Cho, H. H.; Yum, J. H.; Le Formal, F.; Sivula, K. *J. Am. Chem. Soc.* **2020,** *142*, 7795.

145. Yu, J. M.; Lee, J.; Kim, Y. S.; Song, J.; Oh, J.; Lee, S. M.; Jeong, M.; Kim, Y.; Kwak, J. H.; Cho, S.; Yang, C.; Jang, J. W. *Nat. Commun.* **2020,** *11*, 5509.

146. Ye, S.; Shi, W.; Liu, Y.; Li, D.; Yin, H.; Chi, H.; Luo, Y.; Ta, N.; Fan, F.; Wang, X.; Li, C. *J. Am. Chem. Soc.* **2021,** *143*, 12499.

147. Liu, C.; Dasgupta, N. P.; Yang, P. *Chem. Mater.* **2013,** *26*, 415.

148. Zhang, X.; Li, H.; Wang, S.; Fan, F.-R. F.; Bard, A. J. *J. Phys. Chem. C* **2014,** *118*, 16842.

149. Kibria, M. G.; Mi, Z. *J. Mater. Chem. A* **2016,** *4*, 2801.

150. Neville, E. M.; Mattle, M. J.; Loughrey, D.; Rajesh, B.; Rahman, M.; MacElroy, J. M. D.; Sullivan, J. A.; Thampi, K. R. *J. Phys. Chem. C* **2012,** *116*, 16511.

151. Asahi, R.; Morikawa, T.; Irie, H.; Ohwaki, T. *Chem. Rev.* **2014,** *114*, 9824.

152. Yu, J. C.; Ho, W.; Yu, J.; Yip, H.; Wong, P. K.; Zhao, J. *Environ. Sci. Technol.* **2005,** *39*, 1175.

153. Yang, C.; Wang, Z.; Lin, T.; Yin, H.; Lu, X.; Wan, D.; Xu, T.; Zheng, C.; Lin, J.; Huang, F.; Xie, X.; Jiang, M. *J. Am. Chem. Soc.* **2013,** *135*, 17831.

154. Wang, G.; Wang, H.; Ling, Y.; Tang, Y.; Yang, X.; Fitzmorris, R. C.; Wang, C.; Zhang, J. Z.; Li, Y. *Nano Lett.* **2011,** *11*, 3026.

155. Yang, Y.; Niu, S.; Han, D.; Liu, T.; Wang, G.; Li, Y. *Adv. Energy Mater.* **2017,** *7*.

156. Su, J.; Guo, L.; Bao, N.; Grimes, C. A. *Nano Lett.* **2011,** *11*, 1928.

157. Hu, S.; Lewis, N. S.; Ager, J. W.; Yang, J.; McKone, J. R.; Strandwitz, N. C. *J. Phys. Chem. C* **2015,** *119*, 24201.

158. Seger, B.; Pedersen, T.; Laursen, A. B.; Vesborg, P. C.; Hansen, O.; Chorkendorff, I. *J. Am. Chem. Soc.* **2013,** *135*, 1057.

159. Choudhary, S.; Upadhyay, S.; Kumar, P.; Singh, N.; Satsangi, V. R.; Shrivastav, R.; Dass, S. *Int. J. Hydrog. Energy* **2012,** *37*, 18713.

160. Choi, J.; Song, J. T.; Jang, H. S.; Choi, M.-J.; Sim, D. M.; Yim, S.; Lim, H.; Jung, Y. S.; Oh, J. *Electron. Mater. Lett.* **2016,** *13*, 57.

161. Wu, H.; Zhang, Z. *Int. J. Hydrog. Energy* **2011,** *36*, 13481.

162. Mali, M. G.; Yoon, H.; Kim, M.-w.; Swihart, M. T.; Al-Deyab, S. S.; Yoon, S. S. *Appl. Phys. Lett.* **2015,** *106*, 151603.

163. Wang, T.; Luo, Z.; Li, C.; Gong, J. *Chem. Soc. Rev.* **2014,** *43*, 7469.

164. Smith, W. A.; Sharp, I. D.; Strandwitz, N. C.; Bisquert, J. *Energy Environ. Sci.* **2015,** *8*, 2851.

165. Lewis, N. S. *Nat. Nanotechnol.* **2016,** *11*, 1010.

166. Li, Y.; Zhang, J. Z. *Laser Photonics Rev.* **2009,** *4*, 517.

167. Tian, J.; Zhao, Z.; Kumar, A.; Boughton, R. I.; Liu, H. *Chem. Soc. Rev.* **2014,** *43*, 6920.

168. McCrory, C. C.; Jung, S.; Ferrer, I. M.; Chatman, S. M.; Peters, J. C.; Jaramillo, T. F. *J. Am. Chem. Soc.* **2015,** *137*, 4347.

169. Li, D.; Shi, J.; Li, C. *Small* **2018,** *14*, 1704179.

170. He, Y.; Hamann, T.; Wang, D. *Chem. Soc. Rev.* **2019,** *48*, 2182.

171. Tilley, S. D.; Schreier, M.; Azevedo, J.; Stefik, M.; Grätzel, M. *Adv. Funct. Mater.* **2014,** *24*, 303.

172. Yan, Y.; Xia, B.; Xu, Z.; Wang, X. *ACS Catal.* **2014,** *4*, 1693.

173. Haydous, F.; Si, W.; Guzenko, V. A.; Waag, F.; Pomjakushina, E.; El Kazzi, M.; Sévery, L.; Wokaun, A.; Pergolesi, D.; Lippert, T. *J. Phys. Chem. C* **2018,** *123*, 1059.

174. Ma, Q.-B.; Hofmann, J. P.; Litke, A.; Hensen, E. J. M. *Sol. Energy Mater. Sol. Cells* **2015,** *141*, 178.

175. Zheng, J. Y.; Song, G.; Hong, J.; Van, T. K.; Pawar, A. U.; Kim, D. Y.; Kim, C. W.; Haider, Z.; Kang, Y. S. *Cryst. Growth Des.* **2014,** *14*, 6057.

176. Huang, X.; Gao, X.; Xue, Q.; Wang, C.; Zhang, R.; Gao, Y.; Han, Z. *Dalton Trans.* **2020,** *49*, 2184.

177. Vittal, R.; Ho, K.-C. *Renew. Sust. Energy Rev.* **2017,** *70*, 920.

178. Dong, Y.; Chen, Y.; Jiang, P.; Wang, G.; Wu, X.; Wu, R.; Zhang, C. *Chem. Asian J.* **2015,** *10*, 1660.

179. Lopes, T.; Andrade, L.; Le Formal, F.; Grätzel, M.; Sivula, K.; Mendes, A. *Phys. Chem. Chem. Phys.* **2014,** *16*, 16515.

180. Seabold, J. A.; Choi, K.-S. *Chem. Mater.* **2011,** *23*, 1105.

181. Santato, C.; Ulmann, M.; Augustynski, J. *J. Phys. Chem. B* **2001,** *105*, 936.

182. Kudo, A.; Omori, K.; Kato, H. *J. Am. Chem. Soc.* **1999,** *121*, 11459.

183. Kuang, Y.; Jia, Q.; Ma, G.; Hisatomi, T.; Minegishi, T.; Nishiyama, H.; Nakabayashi, M.; Shibata, N.; Yamada, T.; Kudo, A.; Domen, K. *Nat. Energy* **2016,** *2*, 16191.

184. Masudy-Panah, S.; Siavash Moakhar, R.; Chua, C. S.; Tan, H. R.; Wong, T. I.; Chi, D.; Dalapati, G. K. *ACS Appl. Mater. Interfaces* **2016,** *8*, 1206.

185. Lee, J. G.; Kim, D. Y.; Lee, J. H.; Kim, M. W.; An, S.; Jo, H. S.; Nervi, C.; Al-Deyab, S. S.; Swihart, M. T.; Yoon, S. S. *ACS Appl. Mater. Interfaces* **2016,** *8*, 15406.

186. Chiang, C.-Y.; Aroh, K.; Franson, N.; Satsangi, V. R.; Dass, S.; Ehrman, S. *Int. J. Hydrog. Energy* **2011,** *36*, 15519.

187. Nian, J.-N.; Hu, C.-C.; Teng, H. *Int. J. Hydrog. Energy* **2008,** *33*, 2897.

188. Salehmin, M. N. I.; Jeffery Minggu, L.; Arifin, K.; Mohamad Yunus, R.; Mohamed, M. A.; Kassim, M. B. *Appl. Catal. A: Gen* **2019,** *582*, 117104.

189. Cesar, I.; Sivula, K.; Kay, A.; Zboril, R.; Grätzel, M. *J. Phys. Chem. C* **2009,** *113*, 772.

190. Septina, W.; Prabhakar, R. R.; Wick, R.; Moehl, T.; Tilley, S. D. *Chem. Mater.* **2017,** *29*, 1735.

191. Yang, Y.; Xu, D.; Wu, Q.; Diao, P. *Sci. Rep.* **2016,** *6*, 35158.

192. Paracchino, A.; Brauer, J. C.; Moser, J.-E.; Thimsen, E.; Grätzel, M. *J. Phys. Chem. C* **2012,** *116*, 7341.

193. Paracchino, A.; Mathews, N.; Hisatomi, T.; Stefik, M.; Tilley, S. D.; Grätzel, M. *Energy Environ. Sci.* **2012,** *5*, 8673.

194. Luo, J.; Steier, L.; Son, M. K.; Schreier, M.; Mayer, M. T.; Grätzel, M. *Nano Lett.* **2016,** *16*, 1848.

195. Morales-Guio, C. G.; Tilley, S. D.; Vrubel, H.; Grätzel, M.; Hu, X. *Nat. Commun.* **2014,** *5*, 3059.

196. Paracchino, A.; Laporte, V.; Sivula, K.; Grätzel, M.; Thimsen, E. *Nat. Mater.* **2011,** *10*, 456.

197. Pan, L.; Kim, J. H.; Mayer, M. T.; Son, M.-K.; Ummadisingu, A.; Lee, J. S.; Hagfeldt, A.; Luo, J.; Grätzel, M. *Nat. Catal.* **2018,** *1*, 412.

198. Boettcher, S. W.; Warren, E. L.; Putnam, M. C.; Santori, E. A.; Turner-Evans, D.; Kelzenberg, M. D.; Walter, M. G.; McKone, J. R.; Brunschwig, B. S.; Atwater, H. A.; Lewis, N. S. *J. Am. Chem. Soc.* **2011,** *133*, 1216.

199. Lee, M. H.; Takei, K.; Zhang, J.; Kapadia, R.; Zheng, M.; Chen, Y. Z.; Nah, J.; Matthews, T. S.; Chueh, Y. L.; Ager, J. W.; Javey, A. *Angew. Chem.* **2012,** *51*, 10760.

200. Khaselev, O.; Turner, J. A. *Science* **1998,** *280*, 425.

201. Kumagai, H.; Minegishi, T.; Sato, N.; Yamada, T.; Kubota, J.; Domen, K. *J. Mater. Chem. A* **2015,** *3*, 8300.

202. Jiang, F.; Gunawan; Harada, T.; Kuang, Y.; Minegishi, T.; Domen, K.; Ikeda, S. *J. Am. Chem. Soc.* **2015,** *137*, 13691.

203. Polman, A.; Knight, M.; Garnett, E. C.; Ehrler, B.; Sinke, W. C. *Science* **2016,** *352*, aad4424.

204. Bae, D.; Seger, B.; Vesborg, P. C.; Hansen, O.; Chorkendorff, I. *Chem. Soc. Rev.* **2017,** *46*, 1933.

205. Cheng, W.-H.; Richter, M. H.; May, M. M.; Ohlmann, J.; Lackner, D.; Dimroth, F.; Hannappel, T.; Atwater, H. A.; Lewerenz, H.-J. *ACS Energy Lett.* **2018,** *3*, 1795.

206. Wang, Y.; Sharma, A.; Duong, T.; Arandiyan, H.; Zhao, T.; Zhang, D.; Su, Z.; Garbrecht, M.; Beck, F. J.; Karuturi, S.; Zhao, C.; Catchpole, K. *Adv. Energy Mater.* **2021,** *11,* 2101053.

207. Gao, J.; Sahli, F.; Liu, C.; Ren, D.; Guo, X.; Werner, J.; Jeangros, Q.; Zakeeruddin, S. M.; Ballif, C.; Grätzel, M.; Luo, J. *Joule* **2019,** *3*, 2930.

208. Karuturi, S. K.; Shen, H.; Sharma, A.; Beck, F. J.; Varadhan, P.; Duong, T.; Narangari, P. R.; Zhang, D.; Wan, Y.; He, J. H.; Tan, H. H.; Jagadish, C.; Catchpole, K. *Adv. Energy Mater.* **2020,** *10,* 2000772.

209. Hamdani, I. R.; Bhaskarwar, A. N. *Renew. Sustain. Energy Rev.* **2021,** *138,* 110503.

210. Khaselev, O.; Turner, J. A. *Science* **1998,** *280*, 425.

211. Lichterman, M. F.; Carim, A. I.; McDowell, M. T.; Hu, S.; Gray, H. B.; Brunschwig, B. S.; Lewis, N. S. *Energy Environ. Sci.* **2014,** *7*, 3334.

212. Sun, K.; Shen, S.; Liang, Y.; Burrows, P. E.; Mao, S. S.; Wang, D. *Chem. Rev*. **2014,** *114*, 8662.

213. Kim, J. S.; Cho, S. W.; Deshpande, N. G.; Kim, Y. B.; Yun, Y. D.; Jung, S. H.; Kim, D. S.; Cho, H. K. *ACS Appl. Mater. Interfaces* **2019,** *11*, 14840.

214. George, S. M. *Chem. Rev.* **2010,** *110*, 111.

215. Septina, W.; Gunawan; Ikeda, S.; Harada, T.; Higashi, M.; Abe, R.; Matsumura, M. *J. Phys. Chem. C* **2015,** *119*, 8576.

216. Masudy-Panah, S.; Siavash Moakhar, R.; Chua, C. S.; Kushwaha, A.; Dalapati, G. K. *ACS Appl. Mater. Interfaces* **2017,** *9*, 27596.

217. Bard, A. J.; Fan, F. F.; Gioda, A. S.; Nagasubramanian, G.; White, H. S. *Faraday Discuss. Chem. Soc.* **1980,** *70*, 19.

218. Masudy-Panah, S.; Khiavi, N. D.; Katal, R.; Ten It, W.; Saeedikhani, M.; Rimaz, S.; Ying, W.; Xiao, G. *Adv. Mater. Interfaces* **2019,** *6*, 1901099.

219. Miller, E.; DeAngelis, A.; Mallory, S., Multijunction Approaches to Photoelectrochemical Water Splitting. In *Photoelectrochemical Hydrogen Production*, Krol, R. v. d.; Gratzel, M., Eds. Springer: New York, **2012**.

220. Ge, H.; Tian, H.; Zhou, Y.; Wu, S.; Liu, D.; Fu, X.; Song, X. M.; Shi, X.; Wang, X.; Li, N. *ACS Appl. Mater. Interfaces* **2014,** *6*, 2401.

221. Huang, Q.; Ye, Z.; Xiao, X. *J. Mater. Chem. A* **2015,** *3*, 15824.

222. Lianos, P. *Appl. Catal. B Environ.* **2017,** *210*, 235.

223. Yao, T.; An, X.; Han, H.; Chen, J. Q.; Li, C. *Adv. Energy Mater.* **2018,** *8*, 1800210.

224. Young, J. L.; Steiner, M. A.; Döscher, H.; France, R. M.; Turner, J. A.; Deutsch, Todd G. *Nat. Energy* **2017,** *2*, 17028.

225. Cheng, W.-H.; Richter, M. H.; May, M. M.; Ohlmann, J.; Lackner, D.; Dimroth, F.; Hannappel, T.; Atwater, H. A.; Lewerenz, H.-J. *ACS Energy Lett.* **2018,** *3*, 1795.

226. Fountaine, K. T.; Lewerenz, H. J.; Atwater, H. A. *Nat. Commun.* **2016,** *7*, 13706.

227. Shockley, W.; Queisser, H. J. *J. Appl. Phys* **1961,** *32*, 510.

228. Peerakiatkhajohn, P.; Yun, J.-H.; Wang, S.; Wang, L. *J. Photonics Energy* **2016,** *7*, 012006.

229. Jafari, T.; Moharreri, E.; Amin, A. S.; Miao, R.; Song, W.; Suib, S. L. *Molecules* **2016,** *21*, 900.

230. Hoppe, H.; Sariciftci, N. S. *J. Mater. Chem.* **2006,** *16*, 45.

231. Ghazy, O. A. *Adv. Polym. Technol.* **2015,** *34*, 21500.

232. Kietzke, T.; Neher, D.; Landfester, K.; Montenegro, R.; Guntner, R.; Scherf, U. *Nat. Mater.* **2003,** *2*, 408.

233. Moulé, A. J.; Meerholz, K. *Adv. Mater.* **2008,** *20*, 240.

234. Kim, Y.; Cook, S.; Tuladhar, S. M.; Choulis, S. A.; Nelson, J.; Durrant, J. R.; Bradley, D. D. C.; Giles, M.; McCulloch, I.; Ha, C.-S.; Ree, M. *Nat. Mater.* **2006,** *5*, 197.

235. Jin, S.-H.; Vijaya Kumar Naidu, B.; Jeon, H.-S.; Park, S.-M.; Park, J.-S.; Chul Kim, S.; Wook Lee, J.; Gal, Y.-S. *Sol. Energy Mater. Sol. Cells* **2007,** *91*, 1187.

236. Landfester, K. *Top. Curr. Chem.* **2003,** *227*, 75.

237. Holmes, N. P.; Burke, K. B.; Sista, P.; Barr, M.; Magurudeniya, H. D.; Stefan, M. C.; Kilcoyne, A. L. D.; Zhou, X.; Dastoor, P. C.; Belcher, W. J. *Sol. Energy Mater. Sol. Cells* **2013,** *117*, 437.

238. Chen, J.-T.; Hsu, C.-S. *Polym. Chem.* **2011,** *2*, 2707.

239. Dam, H. F.; Holmes, N. P.; Andersen, T. R.; Larsen-Olsen, T. T.; Barr, M.; Kilcoyne, A. L. D.; Zhou, X.; Dastoor, P. C.; Krebs, F. C.; Belcher, W. J. *Sol. Energy Mater. Sol. Cells* **2015,** *138*, 102.

240. Burke, K. B.; Stapleton, A. J.; Vaughan, B.; Zhou, X.; Kilcoyne, A. L.; Belcher, W. J.; Dastoor, P. C. *Nanotechnology* **2011,** *22*, 265710.

241. Mosconi, E.; Salvatori, P.; Saba, M. I.; Mattoni, A.; Bellani, S.; Bruni, F.; Santiago Gonzalez, B.; Antognazza, M. R.; Brovelli, S.; Lanzani, G.; Li, H.; Brédas, J.-L.; De Angelis, F. *ACS Energy Lett.* **2016,** *1*, 454.

242. Darwis, D.; Elkington, D.; Sesa, E.; Cooling, N.; Bryant, G.; Zhou, X.; Belcher, W. J.; Dastoor, P.; Iskandar, F.; Abdullah, M. *AIP Conf. Proc.* **2011,** *1415*, 120.

243. Darwis, D.; Holmes, N.; Elkington, D.; David Kilcoyne, A. L.; Bryant, G.; Zhou, X.; Dastoor, P.; Belcher, W. *Sol. Energy Mater. Sol. Cells* **2014,** *121*, 99.

244. Fortin, P.; Rajasekar, S.; Chowdhury, P.; Holdcroft, S. *Can. J. Chem.* **2018,** *96*, 148.

245. Millstone, J. E.; Kavulak, D. F.; Woo, C. H.; Holcombe, T. W.; Westling, E. J.; Briseno, A. L.; Toney, M. F.; Frechet, J. M. *Langmuir* **2010,** *26*, 13056.

246. Ruder, A. M. *Ann. N. Y. Acad. Sci* **2006,** *1076*, 207.

247. Landfester, K. *Angew. Chem.* **2009,** *48*, 4488.

248. Landfester, K. *Annu. Rev. Mater. Res.* **2006,** *36*, 231.

249. Pecher, J.; Mecking, S. *Chem. Rev.* **2010,** *110*, 6260.

250. Lanfester, K.; Montenegro, R.; Scherf, U.; Guntner, R.; Asawapirom, U.; Patil, S.; Neher, D.; Kietzke, T. *Adv. Mater.* **2002,** *14*, 651.

251. Landfester, K. *Adv. Mater.* **2001,** *13*, 765.

252. Landfester, K.; Schork, F. J.; Kusuma, V. A. *C. R. Chim.* **2003,** *6*, 1337.

253. Schwarz, K. N.; Farley, S. B.; Smith, T. A.; Ghiggino, K. P. *Nanoscale* **2015,** *7*, 19899.

254. Stapleton, A.; Vaughan, B.; Xue, B.; Sesa, E.; Burke, K.; Zhou, X.; Bryant, G.; Werzer, O.; Nelson, A.; David Kilcoyne, A. L.; Thomsen, L.; Wanless, E.; Belcher, W.; Dastoor, P. *Sol. Energy Mater. Sol. Cells* **2012,** *102*, 114.

255. Ulum, S.; Holmes, N.; Darwis, D.; Burke, K.; David Kilcoyne, A. L.; Zhou, X.; Belcher, W.; Dastoor, P. *Sol. Energy Mater. Sol. Cells* **2013,** *110*, 43.

256. Khan, A.; Rahman, F.; Nongjai, R.; Asokan, K. *Solid State Sci.* **2020,** *109,* 106436.

257. Gao, F. G.; Bard, A. J.; Kispert, L. D. *J. Photochem. Photobiol. A: Chem* **2000,** *130*, 49.

258. Suppes, G. M.; Fortin, P. J.; Holdcroft, S. *J. Electrochem. Soc.* **2015,** *162*, H551.

259. Stapleton, A. J. Nanoparticle Based Organic Photovoltaic Devices. University of Newcastle, **2011**.

260. Chantrapornchai, W.; Clydesdale, F. M.; McClements, D. J., Understanding Colors in Emulsions. In *Color Quality of Fresh and Processed Foods*, **2008,** 364.

261. Darwis, D. Fabricating Nanoparticulate Organic Thin Film Transistor (OTFT) and Organic Photovoltaic (OPV) Devices Using Inkjet Printing. University of Newcastle, **2013**.

262. Spano, F. C.; Silva, C. *Annu. Rev. Phys. Chem.* **2014,** *65*, 477.

263. Spano, F. C.; Clark, J.; Silva, C.; Friend, R. H. *J. Chem. Phys.* **2009,** *130*, 074904.

264. Clark, J.; Silva, C.; Friend, R. H.; Spano, F. C. *Phys. Rev. Lett.* **2007,** *98*, 206406.

265. Spano, F. C. *J. Chem. Phys.* **2005,** *122*, 234701.

266. Barnes, M. D.; Baghar, M. *J. Polym. Sci. B Polym. Phys.* **2012,** *50*, 1121.

267. Más-Montoya, M.; Janssen, R. A. J. *Adv. Funct. Mater.* **2017,** *27,* 1605779.

268. Erb, T.; Zhokhavets, U.; Gobsch, G.; Raleva, S.; Stuhn, B.; Schilinsky, P.; Waldauf, C.; Brabec, C. J. *Adv. Funct. Mater.* **2005,** *15*, 1193.

269. Baumann, A.; Lorrmann, J.; Deibel, C.; Dyakonov, V. *Appl. Phys. Lett.* **2008,** 1.

270. Yang, X.; Loos, J.; Veenstra, S. C.; Verhees, W. J.; Wienk, M. M.; Kroon, J. M.; Michels, M. A.; Janssen, R. A. *Nano Lett.* **2005,** *5*, 579.

271. Clark, J.; Chang, J.-F.; Spano, F. C.; Friend, R. H.; Silva, C. *Appl. Phys. Lett.* **2009,** *94*, 163306.

272. Gerischer, H. *Pure Appl. Chem.* **1980,** *52*, 2649.

273. Chiaravalli, G.; Manfredi, G.; Sacco, R.; Lanzani, G. *ACS Appl Mater Interfaces* **2021,** *13*, 36595.

274. Bellani, S.; Fazzi, D.; Bruno, P.; Giussani, E.; Canesi, E. V.; Lanzani, G.; Antognazza, M. R. *J. Phys. Chem. C* **2014,** *118*, 6291.

275. Septina, W.; Prabhakar, R. R.; Wick, R.; Moehl, T.; Tilley, S. D. *Chem. Mater.* **2017,** *29*, 1735.

276. Yip, S. K.; Sauls, J. A. *Phys. Rev. Lett.* **1992,** *69*, 2264.

277. Grigore, M. E.; Biscu, E. R.; Holban, A. M.; Gestal, M. C.; Grumezescu, A. M. *Pharmaceuticals* **2016,** *9*, 75.

278. Samarasekara, P.; Kumara, N. T. R. N.; Yapa, N. U. S. *J. Phys. Condens. Matter* **2006,** *18*, 2417.

279. Tian, X.; Liu, L.; Li, Y.; Yang, C.; Zhou, Z.; Nie, Y.; Wang, Y. *Sens. Actuators B Chem.* **2018,** *256*, 135.

280. Nolan, M.; Elliott, S. D. *Phys. Chem. Chem. Phys.* **2006,** *8*, 5350.

281. Koffyberg, F. P.; Benko, F. A. *J. Appl. Phys.* **1982,** *53*, 1173.

282. Siavash Moakhar, R.; Hosseini-Hosseinabad, S. M.; Masudy-Panah, S.; Seza, A.; Jalali, M.; Fallah-Arani, H.; Dabir, F.; Gholipour, S.; Abdi, Y.; Bagheri-Hariri, M.; Riahi-Noori, N.; Lim, Y. F.; Hagfeldt, A.; Saliba, M. *Adv. Mater.* **2021,** *33*, 2007285.

283. Masudy-Panah, S.; Eugene, Y. J. K.; Khiavi, N. D.; Katal, R.; Gong, X. *J. Mater. Chem. A* **2018,** *6*, 11951.

284. Jang, Y. J.; Jang, J. W.; Choi, S. H.; Kim, J. Y.; Kim, J. H.; Youn, D. H.; Kim, W. Y.; Han, S.; Sung Lee, J. *Nanoscale* **2015,** *7*, 7624.

285. Kunturu, P. P.; Huskens, J. *ACS Appl. Energy Mater.* **2019,** *2*, 7850.

286. Born, B.; Krupa, J. D. A.; Geoffroy-Gagnon, S.; Hristovski, I. R.; Collier, C. M.; Holzman, J. F. *ACS Photonics* **2016,** *3*, 2475.

287. Othonos, A.; Zervos, M. *Nanoscale Res. Lett.* **2011,** *6*, 622.

288. Yildirim, N.; Serin, T.; Serin, N. *J. Optoelectron. Adv. Mater.* **2010,** *12*, 1153.

289. Dimopoulos, T.; Peić, A.; Müllner, P.; Neuschitzer, M.; Resel, R.; Abermann, S.; Postl, M.; List, E. J. W.; Yakunin, S.; Heiss, W.; Brückl, H. *J. Renew. Sustain. Energy* **2013,** *5*, 011205.

290. Chen, W.-T.; Jovic, V.; Sun-Waterhouse, D.; Idriss, H.; Waterhouse, G. I. N. *Int. J. Hydrog. Energy* **2013,** *38*, 15036.

291. Wang, Z.; Liu, Y.; Martin, D. J.; Wang, W.; Tang, J.; Huang, W. *Phys. Chem. Chem. Phys.* **2013,** *15*, 14956.

292. Park, S. M.; Razzaq, A.; Park, Y. H.; Sorcar, S.; Park, Y.; Grimes, C. A.; In, S. I. *ACS Omega* **2016,** *1*, 868.

293. Huang, Q.; Kang, F.; Liu, H.; Li, Q.; Xiao, X. *J. Mater. Chem. A* **2013,** *1*, 2418.

294. Morasch, J.; Wardenga, H. F.; Jaegermann, W.; Klein, A. *phys. status solidi (a)* **2016,** *213*, 1615.

295. Dai, P.; Li, W.; Xie, J.; He, Y.; Thorne, J.; McMahon, G.; Zhan, J.; Wang, D. *Angew. Chem., Int. Ed. Engl.* **2014,** *53*, 13493.

296. Guo, X.; Diao, P.; Xu, D.; Huang, S.; Yang, Y.; Jin, T.; Wu, Q.; Xiang, M.; Zhang, M. *Int. J. Hydrog. Energy* **2014,** *39*, 7686.

297. Chiang, C.-Y.; Shin, Y.; Aroh, K.; Ehrman, S. *Int. J. Hydrog. Energy* **2012,** *37*, 8232.

298. Dasi, G.; Asokan, K.; Thangaraju, K. *Appl. Phys. A* **2017,** *123*.

299. Paracchino, A.; Laporte, V.; Sivula, K.; Gratzel, M.; Thimsen, E. *Nat. Mater.* **2011,** *10*, 456.

300. Jayatissa, A. H.; Guo, K.; Jayasuriya, A. C. *Appl. Surf. Sci.* **2009,** *255*, 9474.

301. Othman, M. A.; Amat, N. F.; Ahmad, B. H.; Rajan, J. *J. Phys. Conf. Ser* **2014,** *495*, 012027.

302. Sowers, K. L.; Fillinger, A. *J. Electrochem. Soc.* **2009,** *156*, F80.

303. Akashi, R.; Naya, S.; Negishi, R.; Tada, H. *J. Phys. Chem. C* **2016,** *120*, 27989.

304. Ganesh, I.; Kumar, P. P.; Annapoorna, I.; Sumliner, J. M.; Ramakrishna, M.; Hebalkar, N. Y.; Padmanabham, G.; Sundararajan, G. *Appl. Surf. Sci.* **2014,** *293*, 229.

305. Samokhvalov, A. A.; Viglin, N. A.; Gizhevskii, B. A.; Loshkareva, N. N.; Osipov, V. V.; Solin, N. I.; Sukhoruko, Y. P. *J. Exp. Theor. Phys.* **1992,** *76*, 463.

306. Rajasekar, S.; Fortin, P.; Tiwari, V.; Srivastva, U.; Sharma, A.; Holdcroft, S. *Synth. Met.* **2019,** *247*, 10.

307. Beranek, R.; Kisch, H. *Angew. Chem. Int. Ed.* **2008,** *47*, 1320.

308. Guijarro, N.; Lana-Villarreal, T.; Gomez, R. *Chem. Commun.* **2012,** *48*, 7681.

309. Szaciłowski, K.; Macyk, W. *Chimia* **2007,** *61*, 831.

310. Gaweda, S.; Podborska, A.; Macyk, W.; Szacilowski, K. *Nanoscale* **2009,** *1*, 299.

311. Garcia-Belmonte, G.; Guerrero, A.; Bisquert, J. *J Phys. Chem. Lett.* **2013,** *4*, 877.

312. Pehlivan, İ. B.; Arvizu, M. A.; Qiu, Z.; Niklasson, G. A.; Edvinsson, T. *J. Phys. Chem. C* **2019,** *123*, 23890.

313. Wick, R.; Tilley, S. D. *J. Phys. Chem. C* **2015,** *119*, 26243.

314. Dubale, A. A.; Pan, C.-J.; Tamirat, A. G.; Chen, H.-M.; Su, W.-N.; Chen, C.-H.; Rick, J.; Ayele, D. W.; Aragaw, B. A.; Lee, J.-F.; Yang, Y.-W.; Hwang, B.-J. *J. Mater. Chem. A* **2015,** *3*, 12482.

315. Zhang, Z.; Wang, P. *J. Mater. Chem.* **2012,** *22*, 2456.

316. Li, G.; Zhu, R.; Yang, Y. *Nat. Photonics* **2012,** *6*, 153.

317. Wooster, T. J.; Golding, M.; Sanguansri, P. *Langmuir* **2008,** *24*, 12758.

318. Ghazy, O. *Macromol. Symp.* **2015,** *352*, 25.

319. Holmes, A.; Deniau, E.; Lartigau-Dagron, C.; Bousquet, A.; Chambon, S.; Holmes, N. P. *ACS Nano* **2021,** *15*, 3927.

320. Fu, C.-M.; Jeng, K.-S.; Li, Y.-H.; Hsu, Y.-C.; Chi, M.-H.; Jian, W.-B.; Chen, J.-T. *Macromol. Chem. Phys.* **2015,** *216*, 59.

321. Verploegen, E.; Mondal, R.; Bettinger, C. J.; Sok, S.; Toney, M. F.; Bao, Z. *Adv. Funct. Mater.* **2010,** *20*, 3519.

322. Monnaie, F.; Brullot, W.; Verbiest, T.; De Winter, J.; Gerbaux, P.; Smeets, A.; Koeckelberghs, G. *Macromolecules* **2013,** *46*, 8500.

323. Sprick, R. S.; Jiang, J. X.; Bonillo, B.; Ren, S.; Ratvijitvech, T.; Guiglion, P.; Zwijnenburg, M. A.; Adams, D. J.; Cooper, A. I. *J. Am. Chem. Soc.* **2015,** *137*, 3265.

324. Kirner, J. T.; Finke, R. G. *J. Mater. Chem. A* **2017,** *5*, 19560.

325. Bornoz, P.; Prevot, M. S.; Yu, X.; Guijarro, N.; Sivula, K. *J. Am. Chem. Soc.* **2015,** *137*, 15338.

326. Saito, K.; Kuwabara, J.; Kanbara, T. *Synth. Met.* **2011,** *161*, 1150.

327. Cho, H.-H.; Yao, L.; Yum, J.-H.; Liu, Y.; Boudoire, F.; Wells, R. A.; Guijarro, N.; Sekar, A.; Sivula, K. *Nat. Catal.* **2021,** *4*, 431.

328. Holliday, S.; Ashraf, R. S.; Wadsworth, A.; Baran, D.; Yousaf, S. A.; Nielsen, C. B.; Tan, C. H.; Dimitrov, S. D.; Shang, Z.; Gasparini, N.; Alamoudi, M.; Laquai, F.; Brabec, C. J.; Salleo, A.; Durrant, J. R.; McCulloch, I. *Nat. Commun.* **2016,** *7*, 11585.

329. Yan, C.; Barlow, S.; Wang, Z.; Yan, H.; Jen, A. K. Y.; Marder, S. R.; Zhan, X. *Nat. Rev. Mater.* **2018,** *3*, 18003.

330. Armin, A.; Li, W.; Sandberg, O. J.; Xiao, Z.; Ding, L.; Nelson, J.; Neher, D.; Vandewal, K.; Shoaee, S.; Wang, T.; Ade, H.; Heumüller, T.; Brabec, C.; Meredith, P. *Adv. Energy Mater.* **2021,** *11*, 2003570.

331. Zhang, G.; Zhao, J.; Chow, P. C. Y.; Jiang, K.; Zhang, J.; Zhu, Z.; Zhang, J.; Huang, F.; Yan, H. *Chem. Rev.* **2018,** *118*, 3447.

332. Li, S.; Zhang, Z.; Shi, M.; Li, C. Z.; Chen, H. *Phys. Chem. Chem. Phys.* **2017,** *19*, 3440.

333. Dou, L.; You, J.; Hong, Z.; Xu, Z.; Li, G.; Street, R. A.; Yang, Y. *Adv. Mater.* **2013,** *25*, 6642.

334. Park, S. H.; Roy, A.; Beaupré, S.; Cho, S.; Coates, N.; Moon, J. S.; Moses, D.; Leclerc, M.; Lee, K.; Heeger, A. J. *Nat. Photonics* **2009,** *3*, 297.

335. Wang, C.; Zhang, Z.; Pejić, S.; Li, R.; Fukuto, M.; Zhu, L.; Sauvé, G. *Macromolecules* **2018,** *51*, 9368.

336. Brebels, J.; Manca, J. V.; Lutsen, L.; Vanderzande, D.; Maes, W. *J. Mater. Chem. A* **2017,** *5*, 24037.

337. Nozik, A. J.; Memming, R. *J. Phys. Chem.* **1996,** *100*, 13061.

338. Zheng, J.; Zhou, H.; Zou, Y.; Wang, R.; Lyu, Y.; Jiang, S. P.; Wang, S. *Energy Environ. Sci.* **2019,** *12*, 2345.

339. Jacobsson, T. J. *Energy Environ. Sci.* **2018,** *11*, 1977.

340. Ardo, S.; Fernandez Rivas, D.; Modestino, M. A.; Schulze Greiving, V.; Abdi, F. F.; Alarcon Llado, E.; Artero, V.; Ayers, K.; Battaglia, C.; Becker, J.-P.; Bederak, D.; Berger, A.; Buda, F.; Chinello, E.; Dam, B.; Di Palma, V.; Edvinsson, T.; Fujii, K.; Gardeniers, H.; Geerlings, H.; H. Hashemi, S. M.; Haussener, S.; Houle, F.; Huskens, J.; James, B. D.; Konrad, K.; Kudo, A.; Kunturu, P. P.; Lohse, D.; Mei, B.; Miller, E. L.; Moore, G. F.; Muller, J.; Orchard, K. L.; Rosser, T. E.; Saadi, F. H.; Schüttauf, J.-W.; Seger, B.; Sheehan, S. W.; Smith, W. A.; Spurgeon, J.; Tang, M. H.; van de Krol, R.; Vesborg, P. C. K.; Westerik, P. *Energy Environ. Sci.* **2018,** *11*, 2768.

341. Rothschild, A.; Dotan, H. *ACS Energy Lett.* **2016,** *2*, 45.

342. Pan, S.; Li, R.; Zhang, Q.; Cui, C.; Wang, M.; Shi, B.; Wang, P.; Zhang, C.; Zhang, B.; Zhao, Y.; Zhang, X. *J. Mater. Chem. A* **2021,** *9*, 14085.

343. Young, J. L.; Steiner, M. A.; Döscher, H.; France, R. M.; Turner, J. A.; Deutsch, T. G. *Nat. Energy* **2017,** *2*, 17028.

344. May, M. M.; Lewerenz, H. J.; Lackner, D.; Dimroth, F.; Hannappel, T. *Nat. Commun.* **2015,** *6*, 8286.

345. Kim, J. H.; Seo, S.; Lee, J. H.; Choi, H.; Kim, S.; Piao, G.; Kim, Y. R.; Park, B.; Lee, J.; Jung, Y.; Park, H.; Lee, S.; Lee, K. *Adv. Funct. Mater.* **2021,** *31*, 2008277.

346. Zhang, Z.; Long, J.; Yang, L.; Chen, W.; Dai, W.; Fu, X.; Wang, X. *Chem. Sci.* **2011,** *2*, 1826.

347. Wang, H.; Zhu, Q.-L.; Zou, R.; Xu, Q. *Chem* **2017,** *2*, 52.

348. Kalisman, P.; Nakibli, Y.; Amirav, L. *Nano Lett.* **2016,** *16*, 1776.

349. Chiang, C. Y.; Epstein, J.; Brown, A.; Munday, J. N.; Culver, J. N.; Ehrman, S. *Nano Lett.* **2012,** *12*, 6005.

350. Peumans, P.; Yakimov, A.; Forrest, S. R. *J. Appl. Phys.* **2003,** *93*, 3693.

351. Barawi, M.; Fresno, F.; Pérez-Ruiz, R.; de la Peña O'Shea, V. A. *ACS Appl. Energy Mater.* **2018,** *2*, 207.

352. Chen, X.; Zhang, Z.; Chi, L.; Nair, A. K.; Shangguan, W.; Jiang, Z. *Nanomicro Lett.* **2016,** *8*, 1.

353. Jana, B.; Bhattacharyya, S.; Patra, A. *Phys. Chem. Chem. Phys.* **2015,** *17*, 15392.

354. Yan, Y.; Crisp, R. W.; Gu, J.; Chernomordik, B. D.; Pach, G. F.; Marshall, Ashley R.; Turner, J. A.; Beard, M. C. *Nat. Energy* **2017,** *2*, 17052.